Fundamental Study on Structural and Surface Control on Single Crystalline Metal Oxide Nanowires

趙，茜茜

https://hdl.handle.net/2324/4496082

出版情報：Kyushu University, 2021, 博士（工学）, 課程博士
バージョン：
権利関係：

Fundamental Study on Structural and Surface Control on Single Crystalline Metal Oxide Nanowires

(単結晶金属酸化物ナノワイヤの微細構造・表面構造制御に関する基礎的研究)

XIXI ZHAO

Ph.D. Thesis September 2021

Fundamental Study on Structural and Surface Control on Single Crystalline Metal Oxide Nanowires

A DISSERTATION SUBMITTED TO
INTERDISCIPLINARY GRADUATE SCHOOL
OF ENGINEERING SCIENCE,
KYUSHU UNIVERSITY
IN PARTIAL FULFILLMENT OF REQUIREMENTS FOR THE DEGREE OF
DOCTOR OF PHILOSOPHY IN ENGINEERING

XIXI ZHAO

September 2021

Abstract

Metal oxide nanowires are promising building blocks for various applications due to their unique physical and chemical properties. Among various nanowire growth methods, a hydrothermal method is particularly promising because the process can be performed at relatively low temperatures (<100 °C). Although efforts have been made to investigate a synthesis and control of hydrothermal single crystalline metal oxide nanowires, there are still challenging and interesting issues as to the controllability of nanowire size distributions and the surface modification and functionalization.

In chapter I, the general introduction for this thesis is described. In chapter II, the related literature review is given to explain the research background of this thesis and the comparison with existing knowledge. In chapter III, I demonstrate the effect strategy of excessive ammonia addition to significantly increase on the growth rate of ZnO nanowires. We found that the ammonia addition substantially narrows the width of "concentration window". The narrowed "concentration window" and the resultant increased growth rate by the ammonia addition can be understood in terms of synchronized effects of both (1) a reduction of zinc hydroxide complex (precursor) concentration and (2) a fast rate limiting process of ligand exchange between different zinc complexes. The present knowledge of "concentration window" will accelerate further tailoring an anisotropic crystal growth of hydrothermal ZnO nanowires. In chapter IV, I demonstrated a facile, rational method to synthesize monodispersed sized zinc oxide (ZnO) nanowires from randomly sized seeds. Uniformly shaped nanowire tips constructed in ammonia-dominated alkaline conditions serve as a foundation for the subsequent formation of the monodisperse nanowires. By precisely controlling the sharp tip formation and the nucleation, our method substantially narrows the distribution of ZnO nanowire diameters. The proposed concept of sharp tip based monodisperse nanowires growth can be applied to the growth of diverse metal oxide nanowires and thus paves the way for bottom-up grown metal oxide nanowires-integrated nanodevices with a reliable performance. In chapter V, I demonstrated an emergence of a thermally robust molecular selectivity with one carbon resolution for aliphatic chains of aldehydes on molecularly templated single crystalline ZnO nanowire surfaces with amorphous TiOx shell layers grown by atomic layer deposition. Spectroscopic, spectrometric and microstructural measurements revealed that such molecular selectivity only emerged when controlling the number of atomic layer deposition cycles with anchoring spatially isolated target-aliphatic aldehyde molecules on the ZnO surface during shell layer formations. This present method to create thermally robust molecular selectivity on abundant oxide surfaces is shown to be simple and highly reproducible and holds promise for scalability and applicability to various molecules. In chapter VI, I summarize overall conclusions in this PhD thesis.

Acknowledgement

First and foremost, I wish to express my sincere gratitude to Prof. Takeshi Yanagida of the Institute for Materials Chemistry and Engineering, Kyushu University; Department of Applied Chemistry, School of Engineering, The University of Tokyo, for his continuous encouragement, supports and stimulating discussions. His sophisticated and exquisite viewpoints always led me to be one step ahead.

I sincerely express my gratitude to Prof. Hata and Prof. Hojo for their invaluable comments and constructive suggestions.

Then, I deeply express my gratitude to Assoc. Prof. Kazuki Nagashima for his lots of encouragement, supports, invaluable discussions, and constructive suggestions. I learned the scientific knowledge, the experimental procedures, the perspectives, and the interests of research from him, especially his ability to be logically rigorous in making presentations.

I would like to express my appreciation to Assis. Prof. Takuro Hosomi for his ideas and explanation during the discussion. His extensive knowledge covering the physical and chemistry field always gives me a new understanding to research.

I would like to express my sincere gratitude to Assoc. Prof. Tsunaki Takahashi. Without his helpful guidance and support, it would be difficult for me to comprehensively understand our experiment and equipment.

I would like to express my appreciation to Dr. Masaki Kanai for lots of theory discussion and guidance in the experiment. I learned systematic knowledge in the semiconductor field, but I also learned the importance of a rigorous scientific attitude.

I would like to express my appreciation for all staff in Yanagida Lab. Especially, I would like to thank Prof. Wataru Tanaka, Dr. Guozhu Zhang, Dr. Benjarong Samransuksame, Dr. Hao Zeng, and Dr. Jiangyang Liu for their support and encouragement.

I would like to thank Ms. Hiroki Imaizumi, she helped me a lot in both life and work, especially with the application for the nursery school. And thanks to Ms. Maki Inoue as well.

I acknowledge all the alumni in Yanagida Lab, including Prof. He Yong, Prof. Gang Meng, Prof. Fuwei Zhuge, Mr. Atsuo Nakao. Dr. Hiroshi Anzai, Dr. Zetao Zhu, Dr. Chen Wang, Dr. Ruolin Yan, Mr. Hiroki Yamashita, Mr. Yuki Nagamatsu, Mr. Kentaro Nakabayashi, Mr. Yuya Akihiro, Mr. Junxiong Zhang, Ms. Mengke Pei, Mr. Sameh Okasha, Mr. Daiki Sakai, Mr. Akihide Inoue, Ms. Chie Nakamura, Dr. Yosuke Hanai, Mr. Rimon Yanaguchi, Mr. Masahiro Shimizu, Mr. Satoru Shiraishi and Dr. Mizuki Matsui.

I would like to thank the Japan Society for the Promotion of Science (JSPS) for financial support. I would like to thank my family for their support and understanding of my career. Especially, my husband, I am thanking him for his support and help in my work and life. I would thank my son (Bohao Zhu). I am thanking him for understanding and supporting me all the time. Finally, I appreciate all the kind people during my Ph.D. course.

XIXI ZHAO

Contents

Chapter I

General Introduction

1.1 General Introduction

1.1.1 Metal Oxide Nanowires

Due to the advantages of larger surface area,[1] grain boundary-free,[2] structural design flexibility,[3] good thermal and chemical stability[4] and diversity of functional properties,[5] single-crystalline metal oxide nanowires are promising candidate materials for electronics,[6] energy harvest,[7] molecular recognition,[8] and human interaction.[9] Various bottom-up methods based on natural crystallization processes have been well developed to grow single-crystal metal oxide nanowires, such as gas-phase and solution-phase methods.[10] Although the gas-phase methods can produce high-quality single-crystal nanowires, the high temperature with more than 600 ºC is often required, which is a limitation to grow nanowires on the thermal-unstable substrates.[11] In contrast, the solution-phase method can grow high-quality single-crystalline nanowires even at low temperature below 100 ºC.[10] Especially, the hydrothermal method is widely used to synthesize various metal oxide nanowires, including ZnO, SnO_2, WO_3, and so on.[12,13] Furthermore, this easy-to-operate method with a low cost enables nanowire growth on a large-scale substrate through an environmentally friendly process. In addition, the structural and morphological control of nanowires can be conducted by adjusting the growth parameters, such as growth time, growth temperature, and solution concentration. Since the structure of nanowires can undoubtedly affect their physical and chemical properties, the designed growth of nanowires by hydrothermal method provides a novel approach to enhancing the performances in various electronic, magnetic, optical and, thermal applications.[14,15,16]

1.1.2 Molecular Recognition

The molecular recognition is often likened to a “lock “and “key”, which involves interactions between host and guest molecules, such as noncovalent interactions, including Van der Waals forces, hydrogen bonds, π-π interactions, coordinate bonds, and electrostatic force.[17,18,19,20] Because of their high selectivity for target molecules, molecular recognition-based separation and sensing systems have gained much attention in the field of disease diagnosis,[21] health monitoring,[22] environmental monitoring,[23] security checking,[24] drug delivery,[25] and so on. Currently, there are three main types of detection instruments based on molecular recognition: 1) Mass Spectrometry (high resolution but needs more extended analysis time);[26] 2) Optical methods (high resolution but only apply to small target molecules);[27] 3) Sensors (small size and portable but limited detection targets and low selectivity).[28] Considering the advantages of miniaturized sensors, including portability, high sensitivity, and fast response, they are one of the most promising next generation instruments based on molecular recognition technology in our further life.[29]

1.1.3 Nanowire Based Molecular Recognition Surface

The diverse demand in the molecular recognition and separation process has accelerated related science and technology development. Current advances in nanotechnology have greatly facilitated the further improvement of the performance of a device due to its dimension in the nanoscale range, which exhibits unique properties compared to bulk materials.[30] Among the various nanomaterials proposed to develop sensor devices, and metal oxide nanowires have attracted great interest due to their excellent single crystallinity, well-defined crystal orientations, high surface-to-volume ratio, and specific physicochemical properties.[31] Significant efforts have been made to enhance the performance of metal oxide nanowires-based molecular recognition devices in the past years.[32] People found that identifying specific molecules can be achieved by two approaches of 1) design the growth of the nanowires, including expanding nanowire material species, growing specific crystal face of nanowires, controlling the morphology of size, uniformity, orientation, and density of nanowires; 2) surface functionalization on nanowires, including doping of metal/oxides on surface, molecular assemble on the surface, MOF coated on surface, and molecular imprinting on the surface.

1.1.4 Significance of This Study

As mentioned above, metal oxide nanowires fabricated by the hydrothermal method provide ideal platforms for constructing molecular recognition surfaces, which can be utilized in sensor and other device applications. However, there are still many problems in creating a novel nanowire-based structure for molecule recognition so far. Firstly, the nanowire growth mechanism is not well developed. For example, the limitation of zinc concentration in nanowire growth and selective anisotropic growth emerges with a certain concentration range. These result in the slow nanowire growth rate at optimal Zn concentration, how to dramatically increase the growth rate of nanowires? Although we found many factors can precisely control the morphology of nanowires, once the seed layer is not uniformly distributed, it is very hard to reduce the size distribution of fabricated nanowires. How to control the uniformity of the nanowire diameter without using the expensive lithography process? Secondly, the selectivity to target molecules of molecular recognition elements is dependent on their intrinsic properties of materials. In this case, the targets that can selectively interact with materials are limited, and the selectivity is not enough. Therefore, how to design a conceptual approach to create a novel type of recognition surface adapted to a large number of targets. From the above description, this thesis is focused on the fundamental study of nanowire growth, control of the nanowire growth, and conceptual creation of a novel nanowire-based recognition surface.

1.2 Framework of This Thesis

This thesis consists of six chapters, which are presented as follows: Chapter 1 presents a general introduction and the framework of this thesis; In chapter 2, a literature review is proposed to give a general introduction of the metal oxide nanowires and their application for molecular recognition, the control of nanowire structure and surface functionalization of nanowires are highlighted; Chapter 3 proposes a model based on modulation of Rate-limiting process in the solution, and successfully enhanced the nanowire growth rate; Chapter 4 presents a rational method to synthesis of monodispersed sized ZnO nanowires from randomly sized seeds; Chapter 5 shows an artificial molecular recognition surface obtained by ALD process and reveals the mechanism of molecule selectivity; Chapter 6 finally gives an overall conclusion of this thesis and the perspective for possible future work.

1.3 References

(1) Hwang, Y. J.; Boukai, A.; Yang, P. High Density N-Si/n-TiO_2 Core/Shell Nanowire Arrays with Enhanced Photoactivity. *Nano Lett.* **2009**, *9* (1), 410–415.

(2) Klamchuen, A.; Suzuki, M.; Nagashima, K.; Yoshida, H.; Kanai, M.; Zhuge, F.; He, Y.; Meng, G.; Kai, S.; Takeda, S.; Kawai, T.; Yanagida, T. Rational Concept for Designing Vapor-Liquid-Solid Growth of Single Crystalline Metal Oxide Nanowires. *Nano Lett.* **2015**, *15* (10), 6406–6412.

(3) Xia, X.; Tu, J.; Zhang, Y.; Wang, X.; Gu, C.; Zhao, X. B.; Fan, H. J. High-Quality Metal Oxide Core/Shell Nanowire Arrays on Conductive Substrates for Electrochemical Energy Storage. *ACS Nano* **2012**, *6* (6), 5531–5538.

(4) Nakamura, K.; Takahashi, T.; Hosomi, T.; Seki, T.; Kanai, M.; Zhang, G.; Nagashima, K.; Shibata, N.; Yanagida, T. Redox-Inactive CO_2 Determines Atmospheric Stability of Electrical Properties of ZnO Nanowire Devices through a Room-Temperature Surface Reaction. *ACS Appl. Mater. Interfaces* **2019**, *11* (43), 40260–40266.

(5) Wang, C.; Hosomi, T.; Nagashima, K.; Takahashi, T.; Zhang, G.; Kanai, M.; Yoshida, H.; Yanagida, T. Phosphonic Acid Modified ZnO Nanowire Sensors: Directing Reaction Pathway of Volatile Carbonyl Compounds. *ACS Appl. Mater. Interfaces* **2020**, *12* (39), 44265–44272.

(6) Lee, S. W.; Kim, J. M.; Park, W.; Lee, H.; Lee, G. R.; Jung, Y.; Jung, Y. S.; Park, J. Y. Controlling Hot Electron Flux and Catalytic Selectivity with Nanoscale Metal-Oxide Interfaces. *Nat. Commun.* **2021**, *12* (1), 40.

(7) Wang, X.; Song, J.; Liu, J.; Wang, Z. L. Direct-Current Nanogenerator Driven by Ultrasonic Waves. *Science* **2007**, *316* (5821), 102–105.

(8) Sysoev, V. V.; Strelcov, E.; Sommer, M.; Bruns, M.; Kiselev, I.; Habicht, W.; Kar, S.; Gregoratti, L.; Kiskinova, M.; Kolmakov, A. Single-Nanobelt Electronic Nose: Engineering and Tests of the Simplest Analytical Element. *ACS Nano* **2010**, *4* (8), 4487–4494.

(9) Baik, J. M.; Zielke, M.; Kim, M. H.; Turner, K. L.; Wodtke, A. M.; Moskovits, M. Tin-Oxide-Nanowire-Based Electronic Nose Using Heterogeneous Catalysis as a Functionalization Strategy. *ACS Nano* **2010**, *4* (6), 3117–3122.

(10) Zhao, X.; Nagashima, K.; Zhang, G.; Hosomi, T.; Yoshida, H.; Akihiro, Y.; Kanai, M.; Mizukami, W.; Zhu, Z.; Takahashi, T.; Suzuki, M.; Samransuksamer, B.; Meng, G.; Yasui, T.; Aoki, Y.; Baba, Y.; Yanagida, T. Synthesis of Monodispersedly Sized ZnO Nanowires

from Randomly Sized Seeds. *Nano Lett.* **2020**, *20* (1), 599–605.

(11) Zhu, Z.; Suzuki, M.; Nagashima, K.; Yoshida, H.; Kanai, M.; Meng, G.; Anzai, H.; Zhuge, F.; He, Y.; Boudot, M.; Takeda, S.; Yanagida, T. Rational Concept for Reducing Growth Temperature in Vapor–Liquid–Solid Process of Metal Oxide Nanowires. *Nano Lett.* **2016**, *16* (12), 7495–7502.

(12) Cheng, C.; Liu, B.; Yang, H.; Zhou, W.; Sun, L.; Chen, R.; Yu, S. F.; Zhang, J.; Gong, H.; Sun, H.; Fan, H. J. Hierarchical Assembly of ZnO Nanostructures on SnO_2 Backbone Nanowires: Low-Temperature Hydrothermal Preparation and Optical Properties. *ACS Nano* **2009**, *3* (10), 3069–3076.

(13) Nekita, S.; Nagashima, K.; Zhang, G.; Wang, Q.; Kanai, M.; Takahashi, T.; Hosomi, T.; Nakamura, K.; Okuyama, T.; Yanagida, T. Face-Selective Crystal Growth of Hydrothermal Tungsten Oxide Nanowires for Sensing Volatile Molecules. *ACS Appl. Nano Mater.* **2020**, *3* (10), 10252–10260.

(14) Zhang, J.; Yu, D.; Du, K.; Wang, F.; Zhao, D.; Wang, Y.; Chen, L.; Kong, M.; Zou, J. Hydrothermally Controlled Growth and Magnetic Properties of Multi-Morphology Manganese Oxide ($RMnO_3$, R=Ca, Sr, Ba) Nano- and Microcrystals. *J. Cryst. Growth* **2013**, *380*, 163–168.

(15) Robak, E.; Coy, E.; Kotkowiak, M.; Jurga, S.; Załęski, K.; Drozdowski, H. The Effect of Cu Doping on the Mechanical and Optical Properties of Zinc Oxide Nanowires Synthesized by Hydrothermal Route. *Nanotechnology* **2016**, *27* (17), 175706.

(16) Liu, C.; Wu, W.; Drummer, D.; Shen, W.; Wang, Y.; Schneider, K.; Tomiak, F. ZnO Nanowire-Decorated Al_2O_3 Hybrids for Improving the Thermal Conductivity of Polymer Composites. *J. Mater. Chem. C* **2020**, *8* (16), 5380–5388.

(17) Mazik, M. Molecular Recognition of Carbohydrates by Acyclic Receptors Employing Noncovalent Interactions. *Chem. Soc. Rev.* **2009**, *38* (4), 935.

(18) Chen, T.; Li, M.; Liu, J. π–π Stacking Interaction: A Nondestructive and Facile Means in Material Engineering for Bioapplications. *Cryst. Growth Des.* **2018**, *18* (5), 2765–2783.

(19) Fersht, A. R. The Hydrogen Bond in Molecular Recognition. *Trends Biochem. Sci.* **1987**, *12*, 301–304.

(20) Shashikala, H. B. M.; Chakravorty, A.; Alexov, E. Modeling Electrostatic Force in Protein-Protein Recognition. *Front. Mol. Biosci.* **2019**, *6*, 94.

(21) Zaidi, S. A. An Overview of Bio-Inspired Intelligent Imprinted Polymers for Virus

Determination. *Biosensors* **2021**, *11* (3), 89.

(22) Dragonieri, S.; van der Schee, M. P.; Massaro, T.; Schiavulli, N.; Brinkman, P.; Pinca, A.; Carratú, P.; Spanevello, A.; Resta, O.; Musti, M.; Sterk, P. J. An Electronic Nose Distinguishes Exhaled Breath of Patients with Malignant Pleural Mesothelioma from Controls. *Lung Cancer* **2012**, *75* (3), 326–331.

(23) Dincer, C.; Bruch, R.; Costa-Rama, E.; Fernández-Abedul, M. T.; Merkoçi, A.; Manz, A.; Urban, G. A.; Güder, F. Disposable Sensors in Diagnostics, Food, and Environmental Monitoring. *Adv. Mater.* **2019**, 1806739.

(24) Cao, A.; Zhu, W.; Shang, J.; Klootwijk, J. H.; Sudhölter, E. J. R.; Huskens, J.; de Smet, L. C. P. M. Metal–Organic Polyhedra-Coated Si Nanowires for the Sensitive Detection of Trace Explosives. *Nano Lett.* **2017**, *17* (1), 1–7.

(25) Liu, R.; Zuo, R.; Hudalla, G. A. Harnessing Molecular Recognition for Localized Drug Delivery. *Adv. Drug Deliv. Rev.* **2021**, *170*, 238–260.

(26) Di Tullio, A.; Reale, S.; De Angelis, F. Molecular Recognition by Mass Spectrometry. *J. Mass Spectrom.* **2005**, *40* (7), 845–865.

(27) Kruss, S.; Landry, M. P.; Vander Ende, E.; Lima, B. M. A.; Reuel, N. F.; Zhang, J.; Nelson, J.; Mu, B.; Hilmer, A.; Strano, M. Neurotransmitter Detection Using Corona Phase Molecular Recognition on Fluorescent Single-Walled Carbon Nanotube Sensors. *J. Am. Chem. Soc.* **2014**, *136* (2), 713–724.

(28) Masuda, Y.; Kato, K.; Kida, M.; Otsuka, J. Selective Nonanal Molecular Recognition with SnO_2 Nanosheets for Lung Cancer Sensor. *Int. J. Appl. Ceram. Technol.* **2019**, *16* (5), 1807–1811.

(29) Righettoni, M.; Amann, A.; Pratsinis, S. E. Breath Analysis by Nanostructured Metal Oxides as Chemo-Resistive Gas Sensors. *Mater. Today* **2015**, *18* (3), 163–171.

(30) Yang, C. C.; Mai, Y.-W. Thermodynamics at the Nanoscale: A New Approach to the Investigation of Unique Physicochemical Properties of Nanomaterials. *Mater. Sci. Eng. R Reports* **2014**, *79*, 1–40.

(31) Zeng, H.; Zhang, G.; Nagashima, K.; Takahashi, T.; Hosomi, T.; Yanagida, T. Metal–Oxide Nanowire Molecular Sensors and Their Promises. *Chemosensors* **2021**, *9* (2), 41.

(32) Ramirez-Vick, J. E. Nanostructured ZnO For Electrochemical Biosensors. *J. Biosens. Bioelectron.* **2012**, *03* (02), 1000e109.

Chapter II

Literature Reviews

2.1 Introduction

As shown in chapter I, this thesis focused on investing the current problems about the growth mechanism of nanowires, the control of nanowires structure, and a further application on molecular recognition. To gain a deeper understanding of the purpose and significance of this work, a thorough review of the current studies is necessary. Therefore, in this chapter, we begin by summarizing research progress based on a bottom-up nanowire growth approach, including vapor-phase growth and liquid-phase growth methods. Then, we further control the structure of the nanowires, including nanowire size, nanowire morphology, nanowire position, nanowire orientation, and nanowire density. We subsequently discuss metal oxide nanowire for molecular recognition application. This is followed by a detailed discussion of various surface modifications of nanowires. Including doping/loading of noble metals, molecular assemble, MOF coated, and molecular imprinting on nanowires.

2.2 Synthesis of Metal Oxide Nanowires

To date, several methods have been developed to fabricate the metal oxide nanowires, which can be mainly described as two different types: "top-town"[1] and "bottom-up"[2] approaches. The top-down approaches usually utilize planar and lithographic techniques to write patterns to obtain well-defined nanowire arrays on substrates. The advantage of this approach is the uniformity of the nanowires. However, this method soon reaches its limits regarding the need for miniaturized devices because of the difficulty in obtaining smaller-sized patterns.[3,4] The bottom-up method is a natural crystallization process-based approach. Nanowires are fabricated from basic nanoscale units by chemical or physical forces. As component size decreases in the nanofabrication process, the bottom-up methods have been intensively investigated on the industrial and scientific demand side.[5,6] In the following subsections, the nanowires we discussed are all grown by bottom-up approaches.

For the bottom-up metal oxide nanowire growth, there are two main types: vapor-phase growth and liquid-phase growth, while the vapor-phase method can be divided into Vapor-Liquid-Solid (VLS) growth and Vapor-Solid (VS) growth.[7,8] Among all the growth methods, the VLS method is specifically used to fabricate highly crystalline nanowires and is widely used in nanotechnology. However, the high growth temperature limits its industrial applications, such as growth on many thermally unstable substrates. To solve this problem, our group proposed a rational concept to reduce the growth temperature in the VLS process by preciously controlling the vapor flux. This concept guided us to grow SnO_2 and ZnO nanowires on the ITO glass and polyimide substrates at a low temperature of 400 °C.[7] Furthermore, various semiconducting metal oxide nanowires, including zinc oxide, indium oxide, and tin oxide, often have conductive properties. However, the origin of the electrical conductivity of the metal oxide nanowires is still not clearly explained. Previously, our group proposed a model to explain the conductivity of the single SnO_2 nanowire. We proved that the VS grow sidewalls of the tapered nanowires lead to the conductivity of the nanowires, which is based on the competitive growth of VLS core growth and VS side growth. Interestingly, the nanowires with the uniform diameter exhibit insulating properties by strictly suppressing VS growth on the sidewalls of the tapered nanowires.[9]

The liquid-phase method has been demonstrated as a promising method for metal oxide nanowires because of the advantage of low growth temperature, large growth scales, low cost, and compatibility on various substrates.[10,11] Several routes to synthesize nanowires in liquid-phase solution were reported, and they can be categorized into template-assisted and template-free methods.[12,13] The template-assisted methods are often combined with the deposition methods, assisted by templates such as aluminum oxide (AAO), nano-channel glass, and porous polymer films. The nanowires fabricated by template-assisted shows a very uniform size distribution. However, this method is limited to metal. Compared to the template-assisted method, the nanowires fabricated by the template-free method are more tedious. Normally, several steps, including 1) formation of crystalline seeds; 2) crystal growth on the seeds; 3) surface stabilization by surfactant, are usually required.

Methods		Position control	Size control	Crystallinity	Temperature
Vapor Phase	VLS growth	◎	◎	◎	> 800 °C
	VS growth	△	△	○	> 800 °C
Liquid Phase	Template-assisted	△	○	△	< 100 °C
	Template-free	◎	○	△	< 100 °C

Table 1: Summary of bottom-up metal oxide nanowires fabrication methods

2.3 Control of the Nanowire Structure

Nanomaterials have been widely used as a material foundation of sensors and device application and have exhibited various degrees of success in improving detection sensitivity and selectivity.[14,15,] No other consideration, nanomaterials themselves can provide a novel platform for chemical detections because of their unique electrical, optical and catalytic properties. In addition, the large surface-to-volume ratio can provide an enormous adsorption surface for enriching the target molecular species.[16] Metal oxide nanowires with well-defined shaped and crystal planes, which have been used to improve the gas sensing selectivity, have received widespread attention. For example, Zhou *et al.* synthesized ZnO nanowires with different diameters and found the diameter-dependent sensing performance, demonstrating that ~110 nm ZnO nanowire, which displays the best gas response, has the maximum donors and minimum acceptors.[17] Zhang *et al.* group designed and synthesized ultrafine $W_{18}O_{49}$ nanowires that only expose [010] crystal plane and found that the selectivity to acetone in VOCs is significantly improved, and demonstrated high selectivity comes from the exposure of its single crystal plan [010].[18]

Thus, by controlling the growth of the nanowire, it is possible to regulate the properties of the sensors and devices.

2.3.1 Nanowire Size Control

As their geometry strongly influences the electrical, optical, and mechanical properties of nanostructured materials.[19,20] Many efforts have been made to the synthesis of monodisperse nanostructures.[21,22] Template synthesis is a straightforward chemical approach to obtain uniform nanowires.[23,24] Polymers (for example, polycarbonate) membranes[25] and anodic alumina (Al_2O_3) nanopores[26] structures are most commonly used.[27] No matter the vapor phase techniques or the solution phase techniques, both show the crucial importance of a homogeneously sized nucleation to obtain the monodisperse nanowires.[28,29] A seed patterning approach[30] has been demonstrated for controlling the initial nucleation, including nanoimprint, photolithography, and electro-beam lithography.[31,32] In addition, the lithography-free approach has also been demonstrated to obtain uniform nanowires. Koivusalo *et al.* present a lithography-free method to fabricate the oxide patterns, which provides a suitable template for the growth of uniform GaAs nanowires by Ga-catalyzed technique.[33]

2.3.2 Nanowire Morphology Control

Control of crystal growth plays a vital role in material designs and various properties modulation.[34,35] Among the tremendous efforts to control the nanostructures synthesis in the past few years, tailoring crystal faces has been an important research topic in materials science.[36,37] This is because each crystal surface has its unique characteristics.[38] And the exposed crystal facets are always the dominating factors that determine the material's geometry, structural stability, and properties.[39,40]

High temperature-based vapor phase methods have been used for growing many advanced nanomaterials.[41] Supersaturation has been revealed to play a significant role in controlling nanostructure morphology.[35] Yin *et al.* successfully observed a unique facet evolution phenomenon at the nanowire tip at different deposition supersaturation within a narrow vapor deposition window.[42] They revealed that high-energy crystal facets, including the $\{10\bar{1}3\}$ and $\{11\bar{2}\bar{2}\}$ facets, could be stably exposed at the nanowire tip. These crystal areas continuously changed with the various supersaturation. The evolution path of crystal facet starts to form (0001) to $\{10\bar{1}3\}$and subsequently to the $\{11\bar{2}\bar{2}\}$, finally go back to the (0001) facet due to the continuously decreased supersaturation.

As for the solution phase synthesized metal oxide nanowires, many strategies have been demonstrated to successfully control the nanowire morphology, such as organic-based surface capping, electrostatic interaction, and the so-called "concentration window", which depends on the difference in critical nucleation concentrations on crystal planes and the ligand exchange effect.[43,44] Elemental doping, a typical method for tuning the properties of inorganic nanomaterials, is often accompanied by various variations in the anisotropic crystal growth of metal oxide nanowires.[45,46] In the case of ZnO nanowires, our group previously demonstrated the concept of "concentration window" in the control of ZnO nanowire morphology.[47] By varying the concentration of Zn ionic species with a certain concentration range, selective anisotropic growth on the (0001) plane can be achieved. Furthermore, by means of modulating the nucleation events and impurity adsorption, we successfully demonstrated a rational way to control the ZnO nanowire morphology and tungsten doped ZnO nanowire.[37] In this study, we found that the addition of WO_4^{2-} can enhance nucleation at the $(10\bar{1}0)$ plane remarkably, which can generate a nano-platelet structure while the dopant incorporation only occurred at the (0001) plane.[37]

2.3.3 Nanowire Position Control

To control the position of nanowires, the area-selective approach which pattern the catalyst or metal oxide seed layer before the growth of nanowire has been widely used, including nanosphere lithography (NSL),[48] laser interference lithography (LIL),[49] nanoimprint lithography (NIL)[50] and electron beam lithography (EBL).[51] The nanowires can be grown in a defined position with seeds that guide nanowire growth.[52] By controlling the position of nanowires, the electrical, optical, and mechanical properties of the formed nanowires array can be modulated, resulting in a novel designation of various miniaturized nanodevices with improved performance in related applications. For example, Wei *et al.* have demonstrated a practical laser interference patterning approach for controllable wafer-scale fabrication of ZnO nanowire arrays with controlled position, size, and orientation, which can be integrated into devices or technology platforms.[53] Tomioka *et al.* demonstrated a III–V nanowire channel on silicon for fabricating high-performance vertical transistors.[54] Considering the structure of the vertical device, precise control of the position of the nanowires was required for further nano-processing of the transistor device.[54]

2.3.4 Nanowire Orientation Control

Controlling the growth orientation of nanowires is crucial for various electronic device applications. The nanowires with three kinds of growth orientations, including vertically aligned nanowire,[55] obliquely aligned nanowires[56], and planar aligned nanowires[57] have shown great promise for applications in the integration of nanowire-based optical, electrical and magnetic devices.

Epitaxial growth mechanism[58] by controlling the crystal matching effect between the crystal plane of the single crystalline substrate (like a-plane or c-plane sapphire substrates) and crystal plane of the nanowire is a commonly used method to guide the direction of nanowire growth.[59] Shalev *et al.* have demonstrated the guided growth of CdSe nanowires with several different growth orientations, including vertically aligned nanowires, obliquely aligned nanowires, and planar aligned horizontal nanowires on five different plans of sapphire.[60] After integrating the nanowires into photodetector devices, they found that nanowires with different crystallographic structures and orientations exhibit different optical and electrical properties.[60] Furthermore, some other methods without controlling the crystal plane of substrates have also been demonstrated. Yang's group previously has successfully controlled the well-defined vertically aligned Si nanowires synthesis using the Vapor-Liquid-Solid epitaxial process.[61] This method is based on the preferred vertical aligned growth direction of material natural features of $SiCl_4$ precursor. And this method to control the vertical nanowire growth is compatible with various substrates.

2.3.5 Nanowire Density Control

Since the density of nanowires is related to the optical, electrical, and mechanical interactions of nanowires, it is crucial to control the density of the nanowire arrays.[62,63] Lithography-based methods have been widely used for the density-controlled synthesis of well-aligned nanowire arrays.[64,65] These methods control the defined positions of the nucleation sites such as catalysts and seeds by writing the pattern using the lithography technique. Therefore, the density of nanowires can be controlled by the number of nucleation sites designed in the lithography pattern. This approach is compatible with most nanowire growth methods with the assistance of the catalyst and seed layers. However, these synthesis processes are time-consuming, expensive and size-limited on the wafer. Therefore, the lithography-free methods through adjusting the concentration of catalyst and the density of seed layer have also been demonstrated. For example, Park *et al.* controlled the density of the vertically aligned Si nanowires through an annealing process prior to growth via an Au-catalyzed VLS mechanism.[66] In this work, the growth sites of the Au catalyst were manipulated by pre-annealing during the formation of Au nanoparticles from Au films.

2.4 Metal Oxide Nanowires for Molecular Recognition

Molecular recognition describes the specific association of molecules.[67,68] The creative ideas of molecular design in the solution phase promote the basic science of molecular recognition. However, considering the environmental effects on molecular recognition systems, extensive research of molecular recognition in various interfaces and materials has been studied. The results show that the interfacial media significantly improve the efficiency of molecular recognition.[69,70] If transfer the assembly of recognition sites onto the device's surface, the science of interface recognition becomes sensor technology.[71,72] To achieve the transmission of the outputs from the molecular recognition surface to the external apparatus, immobilizing the molecular recognition sites on a solid surface has been exploited.[73] With the development of nanotechnology, nanostructured materials have attracted a lot of attention due to their regulated geometry, large surface-to-volume area, and sufficient channels for the easy diffusion of the target molecule. Thus, various nanostructured materials provide an appropriate platform for promoting molecular recognition, sensing, removal, and delivery.[74,75]

2.5 Modifications of Nanowire Surface

As the molecular recognition process usually takes place on the surface of the nanowire, the performance can also be enhanced by microstructure design and modification on the surface of nanowires. Significant efforts have been made to enhance the molecular recognition properties. Identifying specific molecules can be achieved by selecting different nanowire materials, controlling the crystalline surface of nanowires, controlling the size of nanowires, but this approach based on the intrinsic properties of the materials is limited in discriminating large amounts of different molecules. In other words, the variety of such nanowire materials is very limited if molecules are only identified based on their intrinsic properties of interacting with specific molecules. Therefore, alternative strategies of surface modification have been investigated to enhance the diversity of nanowire materials for various molecular recognition-based applications. In this section, we summarized several representative approaches of surface modifications for improving the selectivity of molecular recognition technique.

2.5.1 Doping/Loading of Noble Metals/Oxides on Nanowire Surface

Doping/loading of noble metal/oxide on metal-oxide nanowire surface has been widely employed to functionalize the nanowire-based sensors because of its advantage of simplicity and low cost in the fabrication process. It can be easily obtained by simple chemical and physical methods, including chemical sputter deposition,[76] spin coating,[77] thermal evaporation,[78] plasma-assisted methods, and wet chemical methods.[79,80] Considering the metal catalytic properties, doping/loading of noble metals or oxide catalysts can enhance the gas sensing properties. Currently, the effects of noble metals on the sensing performance of nanowire can be explained with two coexisting mechanisms: 1) chemical effect (spill-over phenomenon): the noble metal doped on the metal oxide nanowire can promote adsorption and dissociation of oxygen molecules in the atmosphere into atomic species and then move to the nanowire surface, resulting in an efficient chemical reaction;[81] 2) electric effect: due to their different work functions, the transfer of electrons from the conduction band of metal oxide nanowires into noble metals/oxides results in the formation of a thicker electron depletion layer, leading to a narrowing of the channel. In this case, the concentration of charge carriers is easily modulated when exposed to the target molecule.[82] For example, Kolmakov *et al.* demonstrated Pd particles functionalized SnO_2 nanowire device, which shows a sensitivity improvement toward oxygen and hydrogen. The improvement of sensing proprieties was attributed to the chemical spillover effect. In other words, the atomic oxygen dissociated on Pd nanoparticles migrates to the SnO_2 nanowire surface, while the weakly bounded molecular oxygens transfer to Pd.[83] Lee *et al.* reported a Fe_2O_3 decorated ZnO nanowire gas sensor with high sensitivity to CO and NH_3, and the formation of an α-Fe_2O_3/ZnO n–n heterojunction attributed to the enhancement of sensitivity.[84]

In addition to improving the sensing response, doping/loading noble metal and oxide can also increase the gas selectivity by utilizing the distinct catalytic activity of materials towards the specific gas.[85,86] For example, Byoun *et al.* demonstrated n-ZnO nanoclusters decorated p-TeO_2 heterostructure nanowires by the ALD technique. As the formation of p-n heterojunctions between n-ZnO and p-TeO_2, the heterostructure-based sensors are more suitable for sensing oxidizing gas, which showed desirable NO_2 selectivity compared with the interfering gas such as SO_2, CO, and C_2H_5OH.[86]

Metal oxide nanomaterials have been a promising material as photocatalyst due to their high reactivity, low toxicity, and chemical stability. However, the intrinsic band gap restricts their catalytic performance. Doping the noble metal into the metal oxide nanomaterials can regulate the band gap of metal oxide nanomaterials. So far, many great efforts have been made to develop noble metals and metal oxide hybrid nanomaterials.[87,88] Nguyen *et al.* demonstrated TiO_2/WO_3 nanoparticles decorated with Ag nanoparticles for improving the selectivity to almost 100% CO as well as the photocatalytic ability of the CO_2 to produce CO.[89] This technique can also be applied to metal oxide nanowires to improve the performance as its tunable structure significantly.

2.5.2 Molecular Assemble on Nanowire Surface

Among the surface modifications, the modifications of organic compounds on the nanowire surface hold the well designability and tunability at a molecular level, presenting specific properties which are not attainable with bulk metal oxide materials.[90,95,91] Self-assembled monolayers (SAMs) which provide a bottom-up approach for constructing new materials on multiple length scales by utilizing the molecules rather than atomic units. SAMs are formed by the chemisorption of the “head group” onto a substrate by non-covalent bonds from either the liquid or vapor phase.[92] Nowadays, organic functionalized nanomaterials have already shown improved properties in the field of molecular recognition, such as catalysis, separation, and drug delivery.[93,99,94] Previously, the molecular recognition on the nanostructures mainly depends on antibody modifications by multi-step modification process. Moreover, the antibody modifications cannot avoid the adsorption of undesired proteins in body fluids on the nanostructures. To capture the target analytes on the nanostructure surfaces instead of antibodies, Shimada *et al.* reported MPC-SH SAM modified Au/ZnO nanowires for increasing the recognition of CRP with calcium ions also reduced nonspecific adsorption.[95] In addition, organic-inorganic materials also show excellent features in the field of gas sensors. Hoffmann *et al.* demonstrated amine terminated SAMs modified SnO_2 NWs, which show both remarkable selectivity and sensitivity towards NO_2 at room temperature. The selectivity of the hybrid sensor is caused by a suitable alignment of the gas-SAM frontier molecular orbitals concerning the SAM-NW fermi-level.[96]

2.5.3 MOF Coated Modification on Nanowire Surface

Metal-organic framework (MOF), as an essential class of new materials in metal-organic materials (MOM), is a framework-structured material consisting of the metal center and organic linker. It has attracted great interest in catalysis applications, drug delivery, gas storage, separation due to its advantages of settable framework structures, large surface areas, regular pores, and open metal sites. And their extraordinary properties of gas storage and separation behavior make it very attractive for the gas sensor in air quality monitoring, chemical industry, and medical diagnostics.[97,1-4,105,106,107,108,98] As the low selectivity and exposure to the humidity of the metal oxide-based sensor, the combination of metal oxide nanowire and MOFs has been considered as a promising approach for enhancing the sensor selectivity.

Yao *et al.* obtained ZIF-CoZn coated ZnO nanowires (ZnO@ZIF-CoZn) using a simple solution method, which exhibited selectivity to acetone and remained highly stable to water vapors at 260 °C. In this work, the authors demonstrated that the selectivity in the water vapor is originated from the hydrophobic nature of the ZIF-CoZn layer, which serves as a filtration membrane to refuse the entry of water molecule and only allow the entry of acetone.[99] Tian *et al.* developed a ZnO@ZIF-8 core-shell heterostructure as a selector for formaldehyde based on the size-selective effects of the aperture of ZIF-8 shell layer. Formaldehyde (2.43 Å) can easily pass the pore of the ZIF-8 (3.40 Å), while methanol (3.63 Å), ethanol (4.53 Å), acetone (4.60 Å), and toluene (5.25 Å) cannot be filtered by the ZIF-8 shell layer.[100] Furthermore, due to the tunable pore sizes, controllable compositions, and high porosity, MOF-derived metal oxide architectures which are prepared by calcination of MOFs, have become a promising sensing material. Koo *et al.* reported a PdO@ZnO loaded hollow SnO_2 nanotubes (PdO@ZnO-SnO_2 NTs) exhibited good selectivity to acetone rather than other interfering gases. This is because the PdO@ZnO catalysts are tightly fixed on the wall of SnO_2 nanotubes, leading to the formation of n-n (ZnO-SnO_2) heterojunction and the electronic sensitization effect of PdO. Moreover, they successfully identified the patterns of the exhaled breath of healthy people and simulated diabetics with PdO@ZnO-SnO_2 NTs.[101]

Gas species	Materials	References
Formaldehyde	ZnO@ZIF-8 nanowire	Tian et al.[100]
Ethanol	ZnO@ZIF-7 nanorods	Zhou et al.[102]
Acetone	ZnO@ZIF-CoZn nanowire	Yao et al.[99]
hydrogen	ZnO@ZIF-8 nanowire	Drobek et al.[103]
	ZnO@ZIF-8 nanorod	Zhou et al.[102]
	ZnO@Pd@ZIF-8 nanowire	Weber et al.[104]

Table 2: MOF coated nanowires for specifically isolating gases

2.5.4 Molecular Imprinting on Nanowire Surface

Molecular imprinting technology (MIT) has been regarded as an attractive method to fabricate artificial structures with tailor-made sites complementary to the template molecules in shape, size, and functional groups.[105] The initial application of MIT is molecular imprinted polymers (MIPs), which is firstly fabricated by Wulff and Sarhan in 1972. They were synthesized by the polymerization of functional and cross-linking monomers in the case of a template ligand.[106] The process is as follows: first, the formation of a complex or a reversible covalent bond between the template and polymerizable functional monomers; second, the template-monomer interactions are fixed by radical polymerization into polymer network; last, the template is removed, and binding sites within the polymer which possess complementary shape and orientation of functional groups are formed. The as-formed imprinted structures can selectively recognize the template molecules. In recent years, the combination of molecular imprinting technology and other technologies is developed and applied to chromatographic separation,[107] solid phase extraction (SPE)[108] and chemical sensors,[109] and more recently is widely used in various fields such as environmental pollution treatment, health diagnosis, food inspection,[110,111,122,123,124] due to its efficient selectivity. However, the MIP also shows the disadvantages of low surface-to-volume ratio, easy aggregation, and low thermal robust properties. To overcome this problem, metal oxide nanowires-based MIPs have received increasing attention due to their physical and chemical robustness. For example, Shi *et al.* reported a 2,4-D photoelectrochemical sensor based on MIP modified TiO_2 nanotubes to enhance the selectivity of 2,4-D determination in multicomponent water samples.[112] Furthermore, Canlas *et al.* reported a novel method to fabricate imprinted metal oxide catalyst by the ALD process. By using this structure, the nanocavities can preferentially react with nitrobenzene rather than nitroxylene in the photoreduction model and react with benzyl alcohol rather than 2,4,6-trimethylbenzyl alcohol in the photo-oxidation model.[113]

2.6 References

(1) Zeng, L.; You, C.; Hong, N.; Zhang, X.; Liang, T. Large-Scale Preparation of 2D Metal Films by a Top-Down Approach. *Adv. Eng. Mater.* **2020**, *22* (3), 1901359.

(2) Wong-Leung, J.; Yang, I.; Li, Z.; Karuturi, S. K.; Fu, L.; Tan, H. H.; Jagadish, C. Engineering III–V Semiconductor Nanowires for Device Applications. *Adv. Mater.* **2020**, *32* (18), 1904359.

(3) Hobbs, R. G.; Petkov, N.; Holmes, J. D. Semiconductor Nanowire Fabrication by Bottom-up and Top-down Paradigms. *Chem. Mater.* **2012**, *24* (11), 1975–1991.

(4) Francioso, L.; Siciliano, P. Top-down Contact Lithography Fabrication of a TiO2 Nanowire Array over a SiO_2 Mesa. *Nanotechnology* **2006**, *17* (15), 3761–3767.

(5) O'Dwyer, C.; Szachowicz, M.; Visimberga, G.; Lavayen, V.; Newcomb, S. B.; Torres, C. M. S. Bottom-up Growth of Fully Transparent Contact Layers of Indium Tin Oxide Nanowires for Light-Emitting Devices. *Nat. Nanotechnol.* **2009**, *4* (4), 239–244.

(6) Han, U. Bin; Lee, J. S. Bottom-up Synthesis of Ordered Metal/Oxide/Metal Nanodots on Substrates for Nanoscale Resistive Switching Memory. *Sci. Rep.* **2016**, *6*, 1–8.

(7) Zhu, Z.; Suzuki, M.; Nagashima, K.; Yoshida, H.; Kanai, M.; Meng, G.; Anzai, H.; Zhuge, F.; He, Y.; Boudot, M.; Takeda, S.; Yanagida, T. Rational Concept for Reducing Growth Temperature in Vapor-Liquid-Solid Process of Metal Oxide Nanowires. *Nano Lett.* **2016**, *16* (12), 7495–7502.

(8) Xu, L.; Li, X.; Zhan, Z.; Wang, L.; Feng, S.; Chai, X.; Lu, W.; Shen, J.; Weng, Z.; Sun, J. Catalyst-Free, Selective Growth of ZnO Nanowires on SiO_2 by Chemical Vapor Deposition for Transfer-Free Fabrication of UV Photodetectors. *ACS Appl. Mater. Interfaces* **2015**, *7* (36), 20264–20271.

(9) Anzai, H.; Suzuki, M.; Nagashima, K.; Kanai, M.; Zhu, Z.; He, Y.; Boudot, M.; Zhang, G.; Takahashi, T.; Kanemoto, K.; Seki, T.; Shibata, N.; Yanagida, T. True Vapor–Liquid–Solid Process Suppresses Unintentional Carrier Doping of Single Crystalline Metal Oxide Nanowires. *Nano Lett.* **2017**, *17* (8), 4698–4705.

(10) Nekita, S.; Nagashima, K.; Zhang, G.; Wang, Q.; Kanai, M.; Takahashi, T.; Hosomi, T.; Nakamura, K.; Okuyama, T.; Yanagida, T. Face-Selective Crystal Growth of Hydrothermal Tungsten Oxide Nanowires for Sensing Volatile Molecules. *ACS Appl.*

Nano Mater. **2020**, *3* (10), 10252–10260.

(11) Zhang, G.; Wang, C.; Mizukami, W.; Hosomi, T.; Nagashima, K.; Yoshida, H.; Nakamura, K.; Takahashi, T.; Kanai, M.; Yasui, T.; Aoki, Y.; Baba, Y.; Yanagida, T. Monovalent Sulfur Oxoanions Enable Millimeter-Long Single-Crystalline: H-WO_3 Nanowire Synthesis. *Nanoscale* **2020**, *12* (16), 9058–9066.

(12) Ra, H. W.; Choi, K. S.; Kim, J. H.; Hahn, Y. B.; Im, Y. H. Fabrication of ZnO Nanowires Using Nanoscale Spacer Lithography for Gas Sensors. *Small* **2008**, *4* (8), 1105–1109.

(13) Clavijo, W. P.; Atkinson, G. M.; Castano, C. E.; Pestov, D. Novel Low-Temperature Fabrication Process for Integrated High-Aspect Ratio Zinc Oxide Nanowire Sensors. *J. Vac. Sci. Technol. B, Nanotechnol. Microelectron. Mater. Process. Meas. Phenom.* **2016**, *34* (2), 022203.

(14) Quesada-González, D.; Merkoçi, A. Nanomaterial-Based Devices for Point-of-Care Diagnostic Applications. *Chem. Soc. Rev.* **2018**, *47* (13), 4697–4709.

(15) Aragay, G.; Pons, J.; Merkoçi, A. Recent Trends in Macro-, Micro-, and Nanomaterial-Based Tools and Strategies for Heavy-Metal Detection. *Chem. Rev.* **2011**, *111* (5), 3433–3458.

(16) Comini, E.; Sberveglieri, G. Metal Oxide Nanowires as Chemical Sensors. *Mater. Today* **2010**, *13* (7–8), 36–44.

(17) Zhou, X.; Wang, A.; Wang, Y.; Bian, L.; Yang, Z.; Bian, Y.; Gong, Y.; Wu, X.; Han, N.; Chen, Y. Crystal-Defect-Dependent Gas-Sensing Mechanism of the Single ZnO Nanowire Sensors. *ACS Sensors* **2018**, *3* (11), 2385–2393.

(18) Zhang, W.; Fan, Y.; Yuan, T.; Lu, B.; Liu, Y.; Li, Z.; Li, G.; Cheng, Z.; Xu, J. Ultrafine Tungsten Oxide Nanowires: Synthesis and Highly Selective Acetone Sensing and Mechanism Analysis. *ACS Appl. Mater. Interfaces* **2020**, *12* (3), 3755–3763.

(19) Kuno, M. Tailoring the Inherent Optical and Electrical Properties of Nanostructures. *J. Phys. Chem. Lett.* **2014**, *5* (21), 3817–3818.

(20) Georgantzinos, S. K.; Siampanis, S. G. Size-Dependent Elastic Mechanical Properties of γ-Graphyne Structures: A Comprehensive Finite Element Investigation. *Mater. Des.* **2021**, *202*, 109524.

(21) Li, C.; Yao, J.; Huang, Y.; Xu, C.; Lou, D.; Wu, Z.; Sun, W.; Zhang, S.; Li, Y.; He,

L.; Zhang, X. Salt-Templated Growth of Monodisperse Hollow Nanostructures. *J. Mater. Chem. A* **2019**, *7* (4), 1404–1409.

(22) Wang, C.; Jiang, J.; Ding, T.; Chen, G.; Xu, W.; Yang, Q. Monodisperse Ternary NiCoP Nanostructures as a Bifunctional Electrocatalyst for Both Hydrogen and Oxygen Evolution Reactions with Excellent Performance. *Adv. Mater. Interfaces* **2016**, *3* (4), 1500454.

(23) Ganapathi, A.; Swaminathan, P.; Neelakantan, L. Anodic Aluminum Oxide Template Assisted Synthesis of Copper Nanowires Using a Galvanic Displacement Process for Electrochemical Denitrification. *ACS Appl. Nano Mater.* **2019**, *2* (9), 5981-5988.

(24) Wendisch, F. J.; Rey, M.; Vogel, N.; Bourret, G. R. Large-Scale Synthesis of Highly Uniform Silicon Nanowire Arrays Using Metal-Assisted Chemical Etching. *Chem. Mater.* **2020**, *32* (21), 9425–9434.

(25) Singh, A. P.; Roccapriore, K.; Algarni, Z.; Salloom, R.; Golden, T. D.; Philipose, U. Structure and Electronic Properties of InSb Nanowires Grown in Flexible Polycarbonate Membranes. *Nanomaterials* **2019**, *9* (9), 1260.

(26) Pribat, D.; Cojocaru, C. S.; Gowtham, M.; Marquardt, B.; Wade, T.; Wegrowe, J. E.; Kim, B. S. Organisation of Carbon Nanotubes and Semiconductor Nanowires Using Lateral Alumina Templates. *C. R. Phys*. **2009**, *10* (4), 320-329.

(27) Jafari Jam, R.; Persson, A. R.; Barrigón, E.; Heurlin, M.; Geijselaers, I.; Gómez, V. J.; Hultin, O.; Samuelson, L.; Borgström, M. T.; Pettersson, H. Template-Assisted Vapour–Liquid–Solid Growth of InP Nanowires on (001) InP and Si Substrates. *Nanoscale* **2020**, *12* (2), 888–894.

(28) Geng, X.; Duan, B. K.; Grismer, D. A.; Zhao, L.; Bohn, P. W. Monodisperse GaN Nanowires Prepared by Metal-Assisted Chemical Etching with in Situ Catalyst Deposition. *Electrochem. commun.* **2012**, *19*, 39–42.

(29) Xi, L.; Tan, W. X. W.; Boothroyd, C.; Lam, Y. M. Understanding and Controlling the Growth of Monodisperse CdS Nanowires in Solution. *Chem. Mater.* **2008**, *20* (16), 5444-5452.

(30) Layani-Tzadka, M. E.; Tirosh, E.; Markovich, G. Patterning Metal Nanowire-Based Transparent Electrodes by Seed Particle Printing. *ACS Omega* **2017**, *2* (11), 7584-7592.

(31) Ko, S. H.; Lee, D.; Hotz, N.; Yeo, J.; Hong, S.; Nam, K. H.; Grigoropoulos, C. P. Digital Selective Growth of ZnO Nanowire Arrays from Inkjet-Printed Nanoparticle Seeds on a Flexible Substrate. *Langmuir* **2012**, *28* (10), 4787–4792.

(32) Nicaise, S. M.; Cheng, J. J.; Kiani, A.; Gradečak, S.; Berggren, K. K. Control of Zinc Oxide Nanowire Array Properties with Electron-Beam Lithography Templating for Photovoltaic Applications. *Nanotechnology* **2015**, *26* (7), 075303.

(33) Koivusalo, E.; Hakkarainen, T.; Guina, M. Structural Investigation of Uniform Ensembles of Self-Catalyzed GaAs Nanowires Fabricated by a Lithography-Free Technique. *Nanoscale Res. Lett.* **2017**, *12* (1), 192.

(34) Jacobsson, D.; Panciera, F.; Tersoff, J.; Reuter, M. C.; Lehmann, S.; Hofmann, S.; Dick, K. A.; Ross, F. M. Interface Dynamics and Crystal Phase Switching in GaAs Nanowires. *Nature* **2016**, *531* (7594), 317–322.

(35) Tian, B.; Xie, P.; Kempa, T. J.; Bell, D. C.; Lieber, C. M. Single-Crystalline Kinked Semiconductor Nanowire Superstructures. *Nat. Nanotechnol.* **2009**, *4* (12), 824–829.

(36) Tu, W.; Guo, W.; Hu, J.; He, H.; Li, H.; Li, Z.; Luo, W.; Zhou, Y.; Zou, Z. State-of-the-Art Advancements of Crystal Facet-Exposed Photocatalysts beyond TiO_2: Design and Dependent Performance for Solar Energy Conversion and Environment Applications. *Mater. Today*. **2020**, 33, 75-86.

(37) Liu, J.; Nagashima, K.; Yamashita, H.; Mizukami, W.; Uzuhashi, J.; Hosomi, T.; Kanai, M.; Zhao, X.; Miura, Y.; Zhang, G.; Takahashi, T.; Suzuki, M.; Sakai, D.; Samransuksamer, B.; He, Y.; Ohkubo, T.; Yasui, T.; Aoki, Y.; Ho, J. C.; Baba, Y.; Yanagida, T. Face-Selective Tungstate Ions Drive Zinc Oxide Nanowire Growth Direction and Dopant Incorporation. *Commun. Mater.* **2020**, *1* (1), 1–2.

(38) Ottoboni, S.; Chrubasik, M.; Mir Bruce, L.; Nguyen, T. T. H.; Robertson, M.; Johnston, B.; Oswald, I. D. H.; Florence, A.; Price, C. Impact of Paracetamol Impurities on Face Properties: Investigating the Surface of Single Crystals Using TOF-SIMS. *Cryst. Growth Des.* **2018**, *18* (5), 2750-2758.

(39) Montalto, L.; Natali, P. P.; Scalise, L.; Paone, N.; Davì, F.; Rinaldi, D.; Barucca, G.; Mengucci, P. Quality Control and Structural Assessment of Anisotropic Scintillating Crystals. *Crystals*. **2019**, *9* (7), 376.

(40) Zou, Z.; Yang, X.; Albéric, M.; Heil, T.; Wang, Q.; Pokroy, B.; Politi, Y.; Bertinetti, L. Additives Control the Stability of Amorphous Calcium Carbonate via Two

Different Mechanisms: Surface Adsorption versus Bulk Incorporation. *Adv. Funct. Mater.* **2020**, *30* (23), 2000003.

(41) Morales, A. M.; Lieber, C. M. A Laser Ablation Method for the Synthesis of Crystalline Semiconductor Nanowires. *Science* **1998**, *279* (5348), 208–211.

(42) Yin, X.; Wang, X. Kinetics-Driven Crystal Facets Evolution at the Tip of Nanowires: A New Implementation of the Ostwald-Lussac Law. *Nano Lett.* **2016**, *16* (11), 7078–7084.

(43) Dev, A.; Chaudhuri, S. Uniform Large-Scale Growth of Micropatterned Arrays of ZnO Nanowires Synthesized by a Surfactant Assisted Approach. *Nanotechnology* **2007**, *18* (17), 175607.

(44) Sakai, D.; Nagashima, K.; Yoshida, H.; Kanai, M.; He, Y.; Zhang, G.; Zhao, X.; Takahashi, T.; Yasui, T.; Hosomi, T.; Uchida, Y.; Takeda, S.; Baba, Y.; Yanagida, T. Substantial Narrowing on the Width of "Concentration Window" of Hydrothermal ZnO Nanowires via Ammonia Addition. *Sci. Rep.* **2019**, *9* (1), 14160.

(45) Dayeh, S. A.; Chen, R.; Ro, Y. G.; Sim, J. Progress in Doping Semiconductor Nanowires during Growth. *Mater. Sci. Semicond. Process.* **2017**, *62*, 135–155.

(46) Kalb, J.; Dorman, J. A.; Siroky, S.; Schmidt-Mende, L. Controlling the Spatial Direction of Hydrothermally Grown Rutile TiO_2 Nanocrystals by the Orientation of Seed Crystals. *Crystals* **2019**, *9* (2), 64.

(47) He, Y.; Nagashima, K.; Kanai, M.; Meng, G.; Zhuge, F.; Rahong, S.; Li, X.; Kawai, T.; Yanagida, T. Nanoscale Size-Selective Deposition of Nanowires by Micrometer Scale Hydrophilic Patterns. *Sci. Rep.* **2015**, *4* (1), 5943.

(48) Lerose, D.; Bechelany, M.; Philippe, L.; Michler, J.; Christiansen, S. Ordered Arrays of Epitaxial Silicon Nanowires Produced by Nanosphere Lithography and Chemical Vapor Deposition. *J. Cryst. Growth* **2010**, *312* (20), 2887-2891.

(49) Schumann, T.; Gotschke, T.; Limbach, F.; Stoica, T.; Calarco, R. Selective-Area Catalyst-Free MBE Growth of GaN Nanowires Using a Patterned Oxide Layer. *Nanotechnology* **2011**, *22* (9), 095603.

(50) Zopes, D.; von Hagen, R.; Müller, R.; Fiz, R.; Mathur, S. Ink-Jetable Patterning of Metal-Catalysts for Regioselective Growth of Nanowires. *Nanoscale* **2010**, *2* (10), 2091.

(51) Lin, L.; Ou, Y.; Aagesen, M.; Jensen, F.; Herstrøm, B.; Ou, H. Time-Efficient High-

Resolution Large-Area Nano-Patterning of Silicon Dioxide. *Micromachines* **2017**, *124* (1), 1-5.

(52) Ashley, M. J.; O'Brien, M. N.; Hedderick, K. R.; Mason, J. A.; Ross, M. B.; Mirkin, C. A. Templated Synthesis of Uniform Perovskite Nanowire Arrays. *J. Am. Chem. Soc.* **2016**, *138* (32), 10096-10099.

(53) Wei, Y.; Wu, W.; Guo, R.; Yuan, D.; Das, S.; Wang, Z. L. Wafer-Scale High-Throughput Ordered Growth of Vertically Aligned ZnO Nanowire Arrays. *Nano Lett.* **2010**, *10* (9), 3414–3419.

(54) Tomioka, K.; Yoshimura, M.; Fukui, T. A III–V Nanowire Channel on Silicon for High-Performance Vertical Transistors. *Nature* **2012**, *488* (7410), 189–192.

(55) Elnathan, R.; Delalat, B.; Brodoceanu, D.; Alhmoud, H.; Harding, F. J.; Buehler, K.; Nelson, A.; Isa, L.; Kraus, T.; Voelcker, N. H. Maximizing Transfection Efficiency of Vertically Aligned Silicon Nanowire Arrays. *Adv. Funct. Mater.* **2015**, *25* (46), 7215–7225.

(56) Ku, N. J.; Wang, C. H.; Huang, J. H.; Fang, H. C.; Huang, P. C.; Liu, C. P. Energy Harvesting from the Obliquely Aligned InN Nanowire Array with a Surface Electron-Accumulation Layer. *Adv. Mater.* **2013**, *25* (6), 861-866.

(57) Fortuna, S. A.; Wen, J.; Chun, I. S.; Li, X. Planar GaAs Nanowires on GaAs (100) Substrates: Self-Aligned, Nearly Twin-Defect Free, and Transfer-Printable. *Nano Lett.* **2008**, *8* (12), 4421–4427.

(58) Tan, C.; Chen, J.; Wu, X. J.; Zhang, H. Epitaxial Growth of Hybrid Nanostructures. *Nat. Rev. Mater.* **2018**. *3* (2), 1–13.

(59) Zhuge, F.; Yanagida, T.; Nagashima, K.; Yoshida, H.; Kanai, M.; Xu, B.; Klamchuen, A.; Meng, G.; He, Y.; Rahong, S.; Li, X.; Suzuki, M.; Kai, S.; Takeda, S.; Kawai, T. Fundamental Strategy for Creating VLS Grown TiO_2 Single Crystalline Nanowires. *J. Phys. Chem. C* **2012**, *116* (45), 24367–24372.

(60) Shalev, E.; Oksenberg, E.; Rechav, K.; Popovitz-Biro, R.; Joselevich, E. Guided CdSe Nanowires Parallelly Integrated into Fast Visible-Range Photodetectors. *ACS Nano* **2017**, *11* (1), 213–220.

(61) Hochbaum, A. I.; Fan, R.; He, R.; Yang, P. Controlled Growth of Si Nanowire Arrays for Device Integration. *Nano Lett.* **2005**, *5* (3), 457–460.

(62) Kim, Y.; Joyce, H. J.; Gao, Q.; Tan, H. H.; Jagadish, C.; Paladugu, M.; Zou, J.;

Suvorova, A. A. Influence of Nanowire Density on the Shape and Optical Properties of Ternary InGaAs Nanowires. *Nano Lett.* **2006**, *6* (4), 599-604.

(63) Erfan, M.; Gnambodoe-Capochichi, M.; Leprince-Wang, Y.; Marty, F.; Sabry, Y. M.; Bourouina, T. Nanowire Length, Density, and Crystalline Quality Retrieved from a Single Optical Spectrum. *Nano Lett.* **2019**, *19* (4), 2509–2515.

(64) Yan, X. M.; Kwon, S.; Centreras, A. M.; Bokor, J.; Somorjal, G. A. Fabrication of Large Number Density Platinum Nanowire Arrays by Size Reduction Lithography and Nanoimprint Lithography. *Nano Lett.* **2005**, *5* (4), 745–748.

(65) Charaev, I.; Silbernagel, T.; Bachowsky, B.; Kuzmin, A.; Doerner, S.; Ilin, K.; Semenov, A.; Roditchev, D.; Vodolazov, D. Y.; Siegel, M. Enhancement of Superconductivity in NbN Nanowires by Negative Electron-Beam Lithography with Positive Resist. *J. Appl. Phys.* **2017**, *122* (8), 083901.

(66) Park, Y. S.; Jung, D. H.; Kim, H. J.; Lee, J. S. Annealed Au-Assisted Epitaxial Growth of Si Nanowires: Control of Alignment and Density. *Langmuir* **2015**, *31* (14), 4290–4298.

(67) Paulsen, H. International Edition in English. *Angew. Chem. Int. Ed.* **1982**, *21* (3), 155–173.

(68) Gale, P. A.; Gunnlaugsson, T. Preface: Supramolecular Chemistry of Anionic Species Themed Issue. *Chem. Soc. Rev.* **2010**, *39* (10), 3595–3596.

(69) Onda, M.; Yoshihara, K.; Koyano, H.; Ariga, K.; Kunitake, T. Molecular Recognition of Nucleotides by the Guanidinium Unit at the Surface of Aqueous Micelles and Bilayers. A Comparison of Microscopic and Macroscopic Interfaces. *J. Am. Chem. Soc.* **1996**, *118* (36), 8524–8530.

(70) Springs, B.; Haake, P. Equilibrium Constants for Association of Guanidinium and Ammonium Ions with Oxyanions. *Bioorg. Chem.* **1977**, *6* (2), 181–190.

(71) Junxiang, H.; Sato, H.; Umemura, Y.; Yamagishi, A. Sensing of Molecular Chirality on an Electrode Modified with a Clay-Metal Complex Hybrid Film. *J. Phys. Chem. B* **2005**, *109* (10), 4679–4683.

(72) Sato, Y.; Yoshioka, K.; Murakami, T.; Yoshimoto, S.; Niwa, O. Design of Biomolecular Interface for Detecting Carbohydrate and Lectin Weak Interactions. *Langmuir* **2012**, *28* (3), 1846–1851.

(73) Kuzuya, A.; Sakai, Y.; Yamazaki, T.; Xu, Y.; Komiyama, M. Nanomechanical DNA

Origami “single-Molecule Beacons” Directly Imaged by Atomic Force Microscopy. *Nat. Commun.* **2011**, *2* (1), 1–8.

(74) Oliveira, O. N.; Iost, R. M.; Siqueira, J. R.; Crespilho, F. N.; Caseli, L. Nanomaterials for Diagnosis: Challenges and Applications in Smart Devices Based on Molecular Recognition. *ACS Appl. Mater. Interfaces* **2014**, *6* (17), 14745–14766.

(75) Bertuna, A.; Faglia, G.; Ferroni, M.; Kaur, N.; Arachchige, H. M. M. M.; Sberveglieri, G.; Comini, E. Metal Oxide Nanowire Preparation and Their Integration into Chemical Sensing Devices at the SENSOR Lab in Brescia. *Sensors* **2017**, *17* (5), 1000.

(76) Sun, K.; Madsen, K.; Andersen, P.; Bao, W.; Sun, Z.; Wang, D. Metal on Metal Oxide Nanowire Co-Catalyzed Si Photocathode for Solar Water Splitting. *Nanotechnology* **2012**, *23* (19).

(77) Aksoy Akgul, F.; Akgul, G.; Turan, R.; Emrah Unalan, H. All Solution-Based Fabrication of Copper Oxide Thin Film/Cobalt-Doped Zinc Oxide Nanowire Heterojunctions. *J. Am. Ceram. Soc.* **2016**, *99* (7), 2497–2503.

(78) Woo, H. S.; Kwak, C. H.; Chung, J. H.; Lee, J. H. Highly Selective and Sensitive Xylene Sensors Using Ni-Doped Branched ZnO Nanowire Networks. *Sens. Actuators B Chem.* **2015**, *216*, 358–366.

(79) Dou, S.; Tao, L.; Wang, R.; El Hankari, S.; Chen, R.; Wang, S. Plasma-Assisted Synthesis and Surface Modification of Electrode Materials for Renewable Energy. *Adv. Mater.* **2018**, *30* (21), 1–24.

(80) Chang, Y. C.; Hsu, C. C.; Wu, S. H.; Chuang, K. W.; Chen, Y. F. Fabrication of Cu-Doped ZnO Nanoneedles on Different Substrate via Wet Chemical Approach: Structural Characterization and Photocatalytic Performance. *Appl. Surf. Sci.* **2018**, *447*, 213–221.

(81) Lee, J. H.; Mirzaei, A.; Kim, J. Y.; Kim, J. H.; Kim, H. W.; Kim, S. S. Optimization of the Surface Coverage of Metal Nanoparticles on Nanowires Gas Sensors to Achieve the Optimal Sensing Performance. *Sens. Actuators B Chem.* **2020**, *302*, 127196.

(82) Navarrete, E.; Bittencourt, C.; Umek, P.; Llobet, E. AACVD and Gas Sensing Properties of Nickel Oxide Nanoparticle Decorated Tungsten Oxide Nanowires. *J. Mater. Chem. C* **2018**, *6* (19), 5181–5192.

(83) Kolmakov, A.; Klenov, D. O.; Lilach, Y.; Stemmer, S.; Moskovitst, M. Enhanced Gas Sensing by Individual SnO_2 Nanowires and Nanobelts Functionalized with Pd Catalyst Particles. *Nano Lett.* **2005**, *5* (4), 667–673.

(84) Jeongseok, L.; Se-Hyeong, L.; So-Young, B.; Yoojong, K.; Kyoungwan, W.; Sanghyun, L.; Yooseong, L.; Moonsuk, Y. Improved Sensitivity of α-Fe_2O_3 Nanoparticle-Decorated ZnO Nanowire Gas Sensor for CO. *Sensors* **2019**, *19* (8), 1903.

(85) Kim, J. H.; Mirzaei, A.; Kim, H. W.; Kim, S. S. Pd Functionalization on ZnO Nanowires for Enhanced Sensitivity and Selectivity to Hydrogen Gas. *Sens. Actuators B Chem.* **2019**, *297*, 126693.

(86) Byoun, Y.; Jin, C.; Choi, S. W. Strategy for Sensitive and Selective NO_2 Detection at Low Temperatures Utilizing P-Type TeO_2 Nanowire-Based Sensors by Formation of Discrete n-Type ZnO Nanoclusters. *Ceram. Int.* **2020**, *46* (11), 19365–19374.

(87) Yunarti, R. T.; Lee, M.; Hwang, Y. J.; Choi, J. W.; Suh, D. J.; Lee, J.; Kim, I. W.; Ha, J. M. Transition Metal-Doped TiO_2 Nanowire Catalysts for the Oxidative Coupling of Methane. *Catal. Commun.* **2014**, *50*, 54–58.

(88) Moon, Y. K.; Jeong, S. Y.; Kang, Y. C.; Lee, J. H. Metal Oxide Gas Sensors with Au Nanocluster Catalytic Overlayer: Toward Tuning Gas Selectivity and Response Using a Novel Bilayer Sensor Design. *ACS Appl. Mater. Interfaces* **2019**, *11* (35), 32169–32177.

(89) Nguyen, C. T. K.; Quang Tran, N.; Seo, S.; Hwang, H.; Oh, S.; Yu, J.; Lee, J.; Anh Le, T.; Hwang, J.; Kim, M.; Lee, H. Highly Efficient Nanostructured Metal-Decorated Hybrid Semiconductors for Solar Conversion of CO_2 with Almost Complete CO Selectivity. *Mater. Today* **2020**, *35*, 25–33.

(90) Vutti, S.; Schoffelen, S.; Bolinsson, J.; Buch-Månson, N.; Bovet, N.; Nygård, J.; Martinez, K. L.; Meldal, M. Click Chemistry Mediated Functionalization of Vertical Nanowires for Biological Applications. *Chem. Eur. J.* **2016**, *22* (2), 496–500.

(91) Kim, S.; Carpenter, P. D.; Jean, R. K.; Chen, H.; Zhou, C.; Ju, S.; Janes, D. B. Role of Self-Assembled Monolayer Passivation in Electrical Transport Properties and Flicker Noise of Nanowire Transistors. *ACS Nano* **2012**, *6* (8), 7352–7361.

(92) Wakayama, Y. On-Surface Molecular Nanoarchitectonics: From Self-Assembly to Directed Assembly. *Jpn. J. Appl. Phys.* **2016**, *55* (11), 1102AA.

(93) Sherlala, A. I. A.; Raman, A. A. A.; Bello, M. M.; Asghar, A. A Review of the Applications of Organo-Functionalized Magnetic Graphene Oxide Nanocomposites for Heavy Metal Adsorption. *Chemosphere* **2018**, *193*, 1004–1017.

(94) Yadav, R.; Baskaran, T.; Kaiprathu, A.; Ahmed, M.; Bhosale, S. V.; Joseph, S.; Al-Muhtaseb, A. H.; Singh, G.; Sakthivel, A.; Vinu, A. Recent Advances in the Preparation and Applications of Organo-Functionalized Porous Materials. *Chem. Asian J.* **2020**, *15* (17), 2588–2621.

(95) Shimada, T.; Yasui, T.; Yokoyama, A.; Goda, T.; Hara, M.; Yanagida, T.; Kaji, N.; Kanai, M.; Nagashima, K.; Miyahara, Y.; Kawai, T.; Baba, Y. Biomolecular Recognition on Nanowire Surfaces Modified by the Self-Assembled Monolayer. *Lab Chip* **2018**, *18* (21), 3225–3229.

(96) Hoffmann, M. W. G.; Mayrhofer Dr, L.; Casals Dr, O.; Caccamo, L.; Hernez-Ramirez, F.; Lilienkamp, G.; Daum, W.; Moseler, M.; Waag, A.; Shen, H.; Prades, J. D. A Highly Selective and Self-Powered Gas Sensor via Organic Surface Functionalization of p-Si/n-ZnO Diodes. *Adv. Mater.* **2014**, *26* (47), 8017–8022.

(97) Furukawa, H.; Cordova, K. E.; O'Keeffe, M.; Yaghi, O. M. The Chemistry and Applications of Metal-Organic Frameworks. *Science* **2013**, *341* (6149), 1230444.

(98) Bakuru, V. R.; Kalidindi, S. B. Synergistic Hydrogenation over Palladium through the Assembly of MIL-101(Fe) MOF over Palladium Nanocubes. *Chem. Eur. J.* **2017**, *23* (65), 16456–16459.

(99) Yao, M. S.; Tang, W. X.; Wang, G. E.; Nath, B.; Xu, G. MOF Thin Film-Coated Metal Oxide Nanowire Array: Significantly Improved Chemiresistor Sensor Performance. *Adv. Mater.* **2016**, *28* (26), 5229–5234.

(100) Tian, H.; Fan, H.; Li, M.; Ma, L. Zeolitic Imidazolate Framework Coated ZnO Nanorods as Molecular Sieving to Improve Selectivity of Formaldehyde Gas Sensor. *ACS Sensors* **2016**, *1* (3), 243–250.

(101) Koo, W. T.; Jang, J. S.; Choi, S. J.; Cho, H. J.; Kim, I. D. Metal-Organic Framework Templated Catalysts: Dual Sensitization of PdO-ZnO Composite on Hollow SnO_2 Nanotubes for Selective Acetone Sensors. *ACS Appl. Mater. Interfaces* **2017**, *9* (21), 18069–18077.

(102) Zhou, T.; Sang, Y.; Wang, X.; Wu, C.; Zeng, D.; Xie, C. Pore Size Dependent Gas-Sensing Selectivity Based on ZnO@ZIF Nanorod Arrays. *Sensors Actuators, B*

Chem. **2018**, *258*, 1099–1106.

(103) Drobek, M.; Kim, J. H.; Bechelany, M.; Vallicari, C.; Julbe, A.; Kim, S. S. MOF-Based Membrane Encapsulated ZnO Nanowires for Enhanced Gas Sensor Selectivity. *ACS Appl. Mater. Interfaces* **2016**, *8* (13), 8323–8328.

(104) Weber, M.; Kim, J. H.; Lee, J. H.; Kim, J. Y.; Iatsunskyi, I.; Coy, E.; Drobek, M.; Julbe, A.; Bechelany, M.; Kim, S. S. High-Performance Nanowire Hydrogen Sensors by Exploiting the Synergistic Effect of Pd Nanoparticles and Metal-Organic Framework Membranes. *ACS Appl. Mater. Interfaces* **2018**, *10* (40), 34765–34773.

(105) Cheong, W. J.; Yang, S. H.; Ali, F. Molecular Imprinted Polymers for Separation Science: A Review of Reviews. *J. Sep. Sci.* **2013**, *36* (3), 609–628.

(106) Wulff, G.; and Sarhan, A. The Use of Polymers with Enzyme-Analogous Structures for the Resolution of Racemates. *Angew. Chem. Int. Ed.* **1972**, *11*, 341–344.

(107) Zhang, K.; Zhou, T.; Kettisen, K.; Ye, L.; Bülow, L. Chromatographic Separation of Hemoglobin Variants Using Robust Molecularly Imprinted Polymers. *Talanta* **2019**, *199*, 27–31.

(108) Arabi, M.; Ostovan, A.; Bagheri, A. R.; Guo, X.; Wang, L.; Li, J.; Wang, X.; Li, B.; Chen, L. Strategies of Molecular Imprinting-Based Solid-Phase Extraction Prior to Chromatographic Analysis. *TrAC Trends Anal. Chem.* **2020**, *128*, 115923.

(109) Leibl, N.; Duma, L.; Gonzato, C.; Haupt, K. Polydopamine-Based Molecularly Imprinted Thin Films for Electro-Chemical Sensing of Nitro-Explosives in Aqueous Solutions. *Bioelectrochemistry* **2020**, *135*, 107541.

(110) Huang, D. L.; Wang, R. Z.; Liu, Y. G.; Zeng, G. M.; Lai, C.; Xu, P.; Lu, B. A.; Xu, J. J.; Wang, C.; Huang, C. Application of Molecularly Imprinted Polymers in Wastewater Treatment: A Review. *Environ. Sci. Pollut. Res.* **2015**, *22* (2), 963–977.

(111) Zhang, Y.; Zhang, J.; Liu, Q. Gas Sensors Based on Molecular Imprinting Technology. *Sensors* **2017**, *17* (7), 1–14.

(112) Shi, H.; Zhao, G.; Liu, M.; Zhu, Z. A Novel Photoelectrochemical Sensor Based on Molecularly Imprinted Polymer Modified TiO_2 Nanotubes and Its Highly Selective Detection of 2,4-Dichlorophenoxyacetic Acid. *Electrochem. commun.* **2011**, *13* (12), 1404–1407.

(113) Canlas, C. P.; Lu, J.; Ray, N. A.; Grosso-Giordano, N. A.; Lee, S.; Elam, J. W.; Winans, R. E.; Van Duyne, R. P.; Stair, P. C.; Notestein, J. M. Shape-Selective

Sieving Layers on an Oxide Catalyst Surface. *Nat. Chem.* **2012**, *4* (12), 1030–1036.

Chapter III

Substantial Narrowing on the Width of "Concentration Window" of Hydrothermal ZnO Nanowires via Ammonia Addition

3.1 Abstract

A crystal growth of hydrothermal ZnO nanowires essentially requires a concentration control within so-called “concentration window”, where the anisotropic crystal growth of ZnO nanowires preferentially occurs. Although understanding what exactly determines the width of “concentration window” is important to tailor the anisotropic crystal growth process, the fundamental knowledge as to “concentration window” is still scarce. Here we report the effect of ammonia addition on the width of “concentration window” using conventional hydrothermal ZnO nanowire growth. We found that the ammonia addition substantially narrows the width of “concentration window”. Within the narrow range of zinc complex concentration, we found a significant increase of growth rate (up to 2000 nm/h) of ZnO nanowires. The narrowed “concentration window” and the resultant increased growth rate by the ammonia addition can be understood in terms of synchronized effects of both (1) a reduction of zinc hydroxide complex (precursor) concentration and (2) a fast rate limiting process of ligand exchange between different zinc complexes. Thus, the present knowledge as to “concentration window” will accelerate further tailoring an anisotropic crystal growth of hydrothermal ZnO nanowires.

3.2 Introduction

Hydrothermally grown ZnO nanowires have attracted significant attentions of many researchers in academia and industry due to their various functional properties, including optical and electrical properties[1–5]. The major useful feature of hydrothermal method is that whole hydrothermal processes can be performed under a relatively low-temperature range less than 100°C[6,7], which is hardly attainable to other conventional vapor-phase nanowire growth methods[8–13]. This low-temperature process expands the application range, particularly when integrating nanowires with other components on various substrates[2,4,14]. Preferential nucleation on ZnO (0001) polar plane is a key process for the anisotropic ZnO nanowire crystal growth[15–17]. Previous studies have revealed the roles of various parameters, such as pH, temperature, and ionic species on hydrothermal ZnO nanowire growth[18–27]. The origin of anisotropic crystal growth in hydrothermal ZnO nanowires has been interpreted in terms of the variations of ionic species in aqueous solutions and their electrostatic interactions with ZnO crystal planes[18,27]. Typically, these hydrothermal ZnO nanowires have been grown under an alkaline condition since divalent Zn ions (Zn^{2+}) do not hydroxylate in acidic environments[25–30]. This is because zinc hydroxide complexes ($Zn(OH)_n$) are necessary as precursors in solution for ZnO crystal growth[19,25]. A supplying rate of zinc hydroxide complexes to crystal growth interface on (0001) plane essentially determines a growth rate of hydrothermal ZnO nanowire growths[19,25]. Therefore, increasing a concentration of zinc hydroxide complexes in solution is effective to increase a growth rate of hydrothermal ZnO nanowires. However, there are inherent limitations for the enhancement of the nanowire growth rate within the framework of conventional strategy based on increasing a precursor concentration. First, the homogeneous nucleation in bulk solution occurs at the relatively low Zn concentration range[30]. Tis limits the supplying rate of Zn species to nanowire and the resultant growth rate of ZnO nanowires. To suppress this homogeneous nucleation in solution, an ammonia was added[27–30]. The resultant zinc ammonia complexes act as buffer for Zn species, which suppresses the homogeneous nucleation in solution even at relatively high Zn concentration range[27–30]. However, there is another inherent limitation of increasing Zn species concentration to keep an anisotropic crystal growth along [0001] direction. This is because a face selective anisotropic growth on (0001) plane emerges within a certain concentration range[16]. This is so-called as "concentration window"[16]. Above the concentration range, a crystal growth on (1010) plane tends to simultaneously occur, which suppresses an anisotropic crystal growth on (0001) plane, promoting to be a film structure rather than a nanowire structure. The precise control of the Zn species concentration therefore is necessary to maintain the nanowire morphology without lateral (1010) plane growth. This restriction of appropriate concentration range "concentration window" for anisotropic ZnO nanowire growths is essential. Although understanding what exactly determines the width of "concentration window" is important to design the anisotropic crystal growth process of ZnO nanowires, the fundamental knowledge as to "concentration window" is still scarce. It is not well understood how a growth condition affects the width of "concentration window", for example the effect of ammonia addition, which is frequently employed to suppress a seed nucleation in solution[27–30]. These backgrounds motivated us to study the effect of ammonia addition on the width of "concentration window", which is an essential requirement for the anisotropic nanowire crystal growth.

3.3 Experimental

ZnO nanowire regular arrays are employed to measure a growth rate of each crystal plane. The ZnO nanowire regular arrays are fabricated onto spatially patterned photoresist/ZnO seed layer/Al_2O_3 substrates by utilizing hydrothermal method. Epitaxial ZnO seed layers (33nm thickness) are deposited onto single crystalline Al_2O_3 (0001) substrate by pulsed laser deposition[31]. The deposition temperature and the oxygen partial pressure during film deposition are 600 °C and 1Pa, respectively. Fabricated ZnO seed layers are grown along [0001] orientation. Photoresist-AZ5206/Z5200 (2:1) (Electronic Materials), which is utilized for a mask of nanowire regular array, is coated onto ZnO/Al_2O_3 substrate by spin-coating at 5000 rpm for 60 s and subsequently bake it at 120 °C for 2 min. After this process, the circular hole array patterns with 520nm diameter and 400 nm interval distances are fabricated by nanoimprint lithography. The patterned photoresist is then solidified at 120 °C for 5 min. The photoresist residuals at the bottom of patterned hole are removed by reactive ion etching process (JEOL, JP-170). The remained photoresist thickness on nonpatterned area is ~50nm. Ten, we perform the hydrothermal ZnO nanowire growth experiments. Solutions for hydrothermal reactions are mixtures composed of zinc nitrate hexahydrate-$Zn(NO_3)_2$•$6H_2O$ (Wako, 99.0%) and hexamethylenetetramine-HMTA, $(CH_2)_6N_4$ (Wako, 99.0%) 15mM. The aqueous solution is prepared at room temperature, and the zinc nitrate hexahydrate concentration is varied from 0.1 to 40mM to examine the concentration dependence. For the ammonia contained growth condition, 500mM ammonia aqueous solution is added after mixing zinc nitrate hexahydrate and HMTA. The pH values are measured by using a pH meter (EUTECH, Cyber Scan pH310). For the pH control condition, HNO_3 is carefully added to the ammonia contained growth solution by monitoring the pH value. The patterned substrate is immersed into the solution and kept at 95 °C for a given time. Finally, the regular arrays of ZnO nanowires grown along [0001] orientation are obtained. Structural characterizations of fabricated ZnO nanowires are performed by using x-ray diffraction (PHILIPS, X'Pert MRD 45 kV, 40mA), field emission scanning electron microscopy-SEM (JEOL, JSM-7610F) and transmission electron microscopy-TEM (JEOL, JEM-ARM200F). Photoluminescence (JASCO, FP-8500), Raman spectroscopy (Tokyo Instruments, Nanofnder®30) and UV-vis absorption spectra (JASCO, V-770) are measured to examine the properties of nanowires. Visual MINTEQ software is employed to calculate equilibrium concentrations of various ionic species in solution at given temperature and pH ranges.

3.4 Results and Discussions

Figure 1a shows the fabrication process employed in this study. Epitaxial ZnO seed layers (33 nm thickness) are deposited onto single crystalline Al_2O_3 (0001) substrate by pulsed laser deposition[31]. The deposition temperature and the oxygen partial pressure during film deposition are 600°C and 1Pa, respectively. As shown in Fig. 1b, fabricated ZnO seed layers are grown along [0001] orientation. The regular arrays of ZnO nanowires grown along [0001] orientation is obtained as shown in Fig. 1b, c. Figure 2 shows the effect of ammonia addition-500 mM on the nanowire morphologies when varying the concentration of zinc nitrate hexahydrate in solution. The other experimental conditions are described in experimental method section. As seen in the SEM images, the appropriate concentration range “concentration window” for nanowire growth is consistently observed. Below the “concentration window”, there is no visible crystal growth. Within the “concentration window”, the nanowires tend to grow, and further increasing the concentration enhances a crystal growth even along lateral direction, which increases the nanowire diameter and finally showing a film structure rather than a nanowire structure. It should be highlighted that the ammonia addition substantially narrows the width of “concentration window”. Regarding the effect of ammonia addition, there are three remarkable differences on the concentration dependence data. First, the ammonia addition increases the critical concentration for nanowire growths. Second, the ammonia addition lowers the critical concentration for film structures. Third, the ammonia addition increases the nanowire growth rate. To specify more quantitatively above trends regarding the concentration dependence, we extract the length and radius data of fabricated nanowires as a function of a concentration, and the results are shown in Fig. 3. Data of nanowires grown for 5h are shown in the figure. The length data and radius data are measured over 100 nanowires in cross-sectional SEM images or top-view SEM images. Above three major trends as to the effect of ammonia addition can be more quantitatively confirmed in Fig. 3. First, the ammonia addition shifts the critical concentrations for nanowire growth to the higher value 1.5mM from 0.15mM. Note that the critical concentration value (0.15mM) for nanowire growth without the ammonia addition differs from the value (0.01–0.1mM) of our early work16, this is because our early work employed an equimolar ratio of the two, whereas the present work used the constant concentration (15mM) of hexamethylenetetramine (HMTA) when varying the concentration of zinc nitrate hexahydrate from 0.1 to 40mM. On the other hand, the ammonia addition lowers the critical concentrations for lateral crystal growth from 5mM to 2mM. In addition, as to the nanowire growth rate at the critical concentration for lateral crystal growth, the nanowire growth rate with ammonia addition is 570nm/h, which is almost 4 times higher than the nanowire growth rate (140nm/h) without ammonia addition. These concentration data highlight that the ammonia addition narrows the width of "concentration window" with the increased nanowire growth rate.

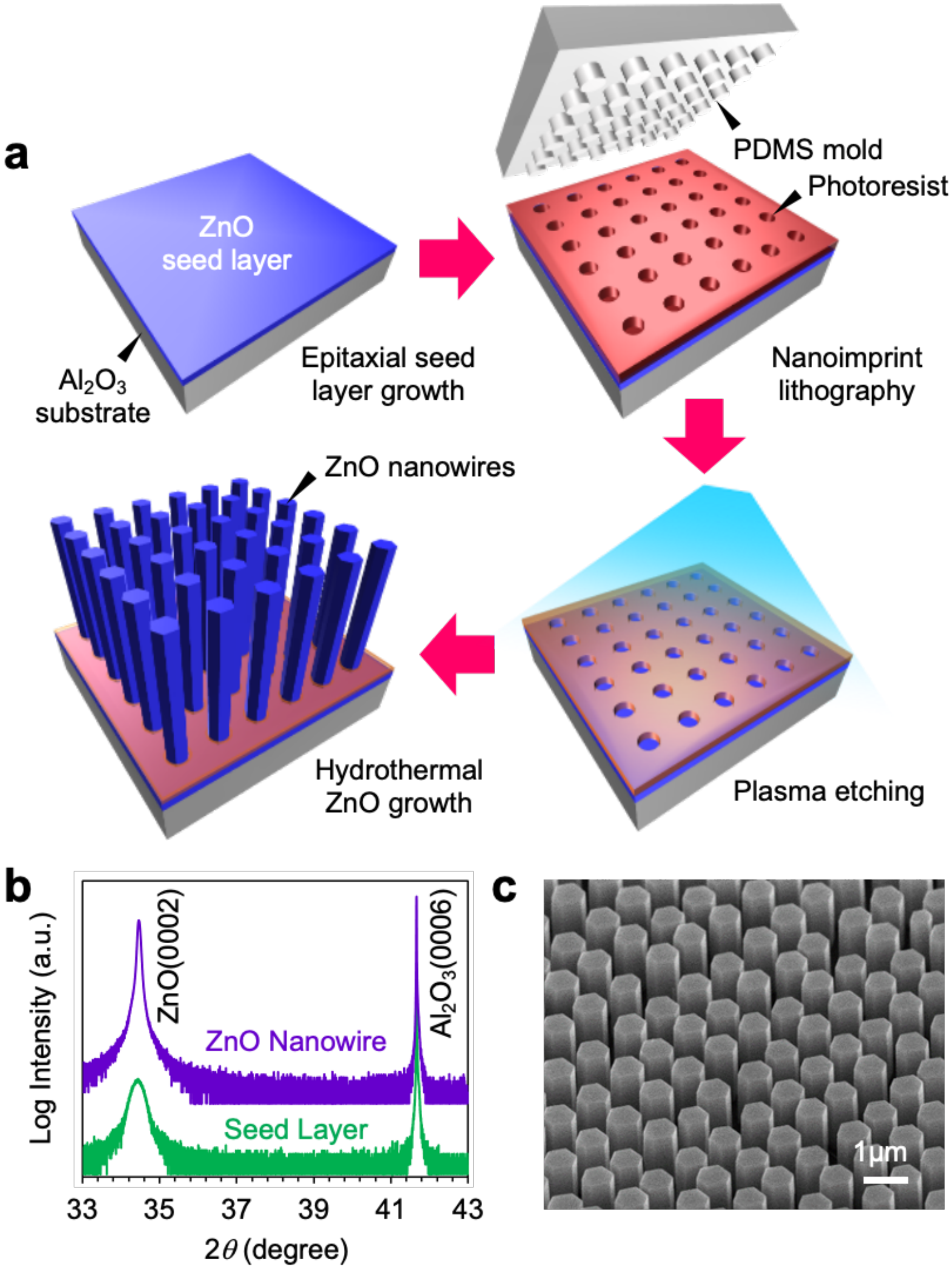

Figure 1. (a) Schematic of fabrication process for regular array of ZnO nanowires. (b) XRD data of ZnO seed layer and ZnO nanowires on Al_2O_3 substrate. (c) Typical SEM image of fabricated regular array of ZnO nanowires.

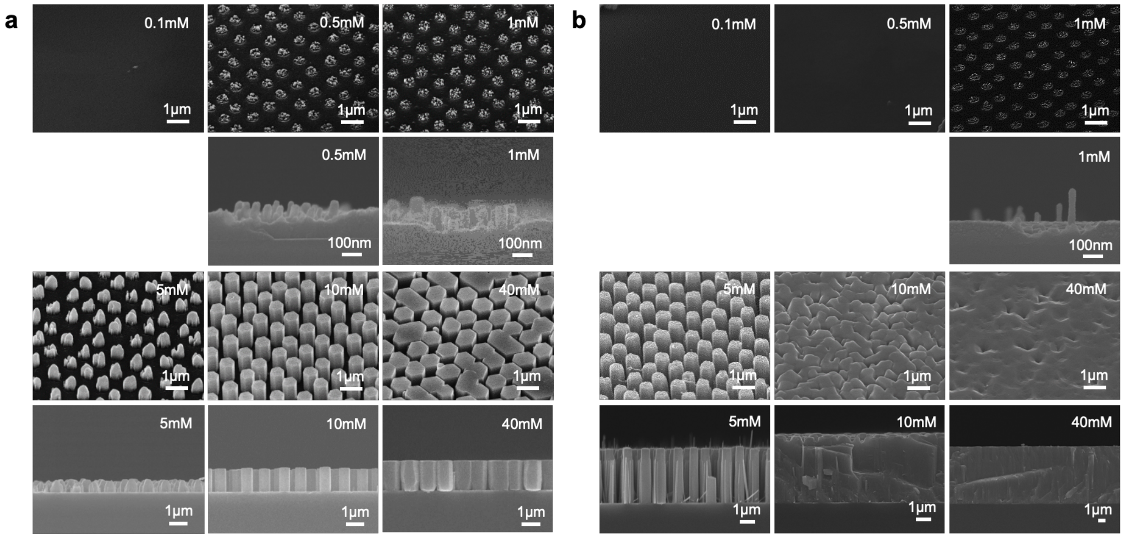

Figure 2. Effect of ammonia addition-500mM on ZnO nanowire morphologies when varying concentration of zinc nitrate hexahydrate from 0.1 to 40 mM. All growth experiments are performed for 5h. (a) SEM images of nanowires grown without ammonia, and (b) with excessive ammonia addition -500mM. Upper shows titled images and lower shows cross-sectional images, respectively.

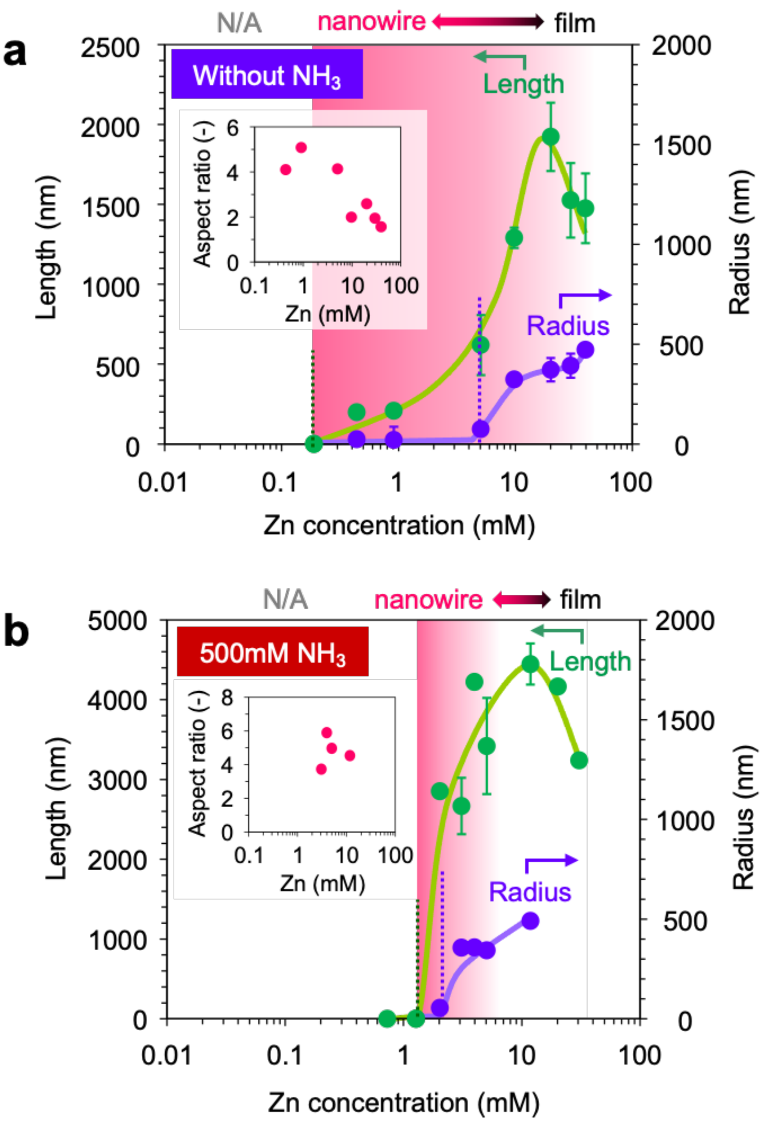

Figure 3. Zn concentration dependence on the nanowire morphology data (including length and radius), which are measured from SEM images of regular arrays. Inset shows aspect ratio. All growth experiments are performed for 5h. (a) Zn concentration dependence on ZnO nanowire morphology with HMTA 15 mM without ammonia addition. (b) Zn concentration dependence on ZnO nanowire morphology with HMTA 15 mM with ammonia addition-500 mM. In both figures, the Zn concentration range, where a nanowire can be grown, is highlighted by a red color.

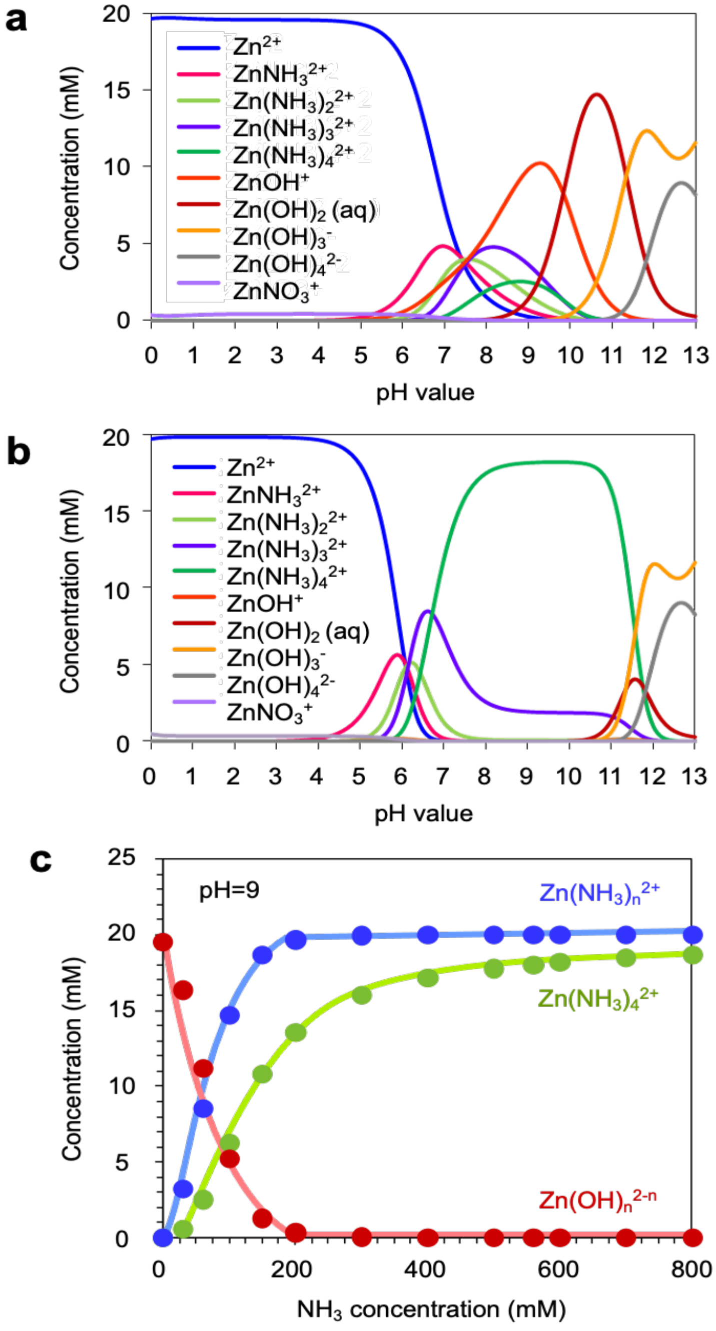

Figure4. (a) Simulation data of ionic species in solution without ammonia addition (ammonia is supplied only by decomposition of HMTA). (b) Simulation data for solution with 500 mM ammonia addition. (c) Effect of ammonia addition on concentration of various zinc complexes. In simulation, the temperature and Zn $(NO_3)_2$ concentration are set to be 95 °C and 20 mM, respectively.

We calculate the populations of existing ionic species in aqueous solution, as shown in Fig. 4. The thermodynamic calculations are performed using software-Visual MINTEQ. These calculation data reveal the effect of ammonia addition in terms of the population of ionic species in aqueous solution. Figure 4(a) shows the calculated population data of ionic species in solution without ammonia addition (ammonia is supplied only by decomposition of HMTA). Figure 4(b) shows the calculated population data of ionic species in solution with ammonia addition-500mM. In these figures, Zn^{2+}, Zn (NH_4) n, Zn (OH)x, $ZnNO_3{}^{+}$ are shown as the major ionic species in solution. When ammonia is not added, Zn^{2+} and zinc hydroxide complex ions coexist at pH values ranged from 6 to 10. The ammonia addition (500mM) results in the increase of zinc ammonia complex ions[27–30] via a ligand exchange process at pH values ranged from 6 to 11. These zinc ammonia complex ions tend to suppress the populations of zinc hydroxide complex ions at pH values ranged from 6 to 10, as increasing the ammonia concentration, as shown in Fig. 4c. The increase of zinc ammonia complexes lowers the degree of supersaturation of zinc hydroxide complex ions in the growth solution[27–30], leading to the increase of critical concentration for nanowire growth as shown in Fig. 3b. Since a pH value strongly affects the populations of existing ionic species in aqueous solution as seen in Fig. 4, we measure pH values for growth conditions of experiments in Fig. 3. The pH values for experiments without ammonia addition are ranged from 6.5 to 8 when varying the concentration of zinc nitrate hexahydrate (0.1–40mM), which is a weak acid. When ammonia-500 mM is added, the pH values are ranged from 10.2 to 11.3 for the concentration range (0.1–40 mM) of zinc nitrate hexahydrate. Tus, it is necessary to consider the effect of pH to understand the difference between Fig. 3a, b. Based on the pH value difference and thermodynamic calculation data in Fig. 4, we consider the effect of ammonia addition on the molar ratio of zinc hydroxide complex ions as precursors. The molar ratio of total zinc hydroxide complex ions in ammonia-500 mM added solution is estimated to be about 0.5 mM, which is approximately 5 times lower than the value-

2.8mM for solution without ammonia addition. Interestingly, the molar ratio difference of hydroxide complex ions is reasonably consistent with the critical concentration difference for nanowire growths in Fig. 3a, b (0.15–0.2 mM for case without ammonia and 1–1.5 mM for case with ammonia addition). Tis consistency implies that not zinc ammonia complex ions but hydroxide complex ions act as a precursor for ZnO nanowire growth. Tus, the increase of critical concentration for nanowire growth as shown in Fig. 3b can be interpreted in terms of the change of precursor complex concentration in solution. It is noted that in the presence of ammonia addition, the nanowire growth rate increases even when decreasing the total Zn concentration in solution.

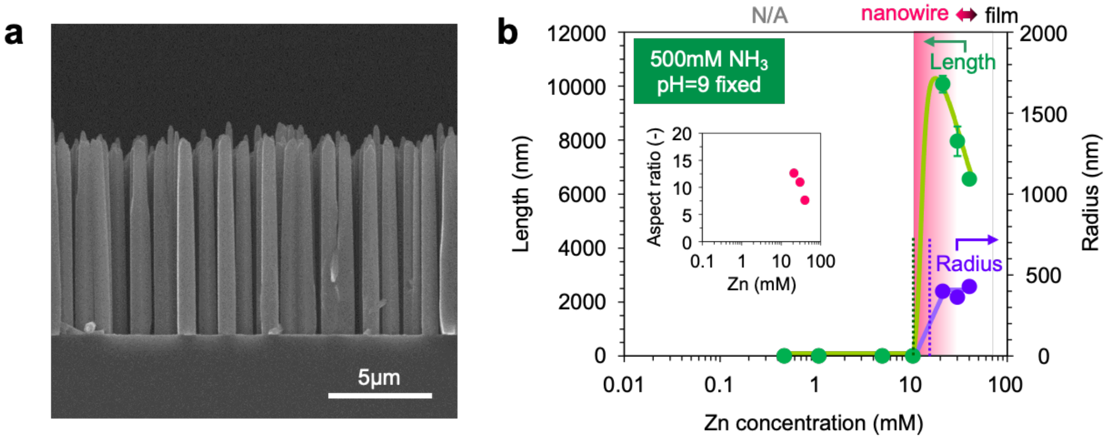

Figure 5. Effect of pH control on ZnO nanowire morphology data ((a) SEM image and (b) length and radius data) as a function of Zn concentration with HMTA 15mM, excessive ammonia addition-500mM and pH=9 control. Inset of (b) shows aspect ratio. The Zn concentration rage, where a nanowire can be grown, is heighted by a red color.

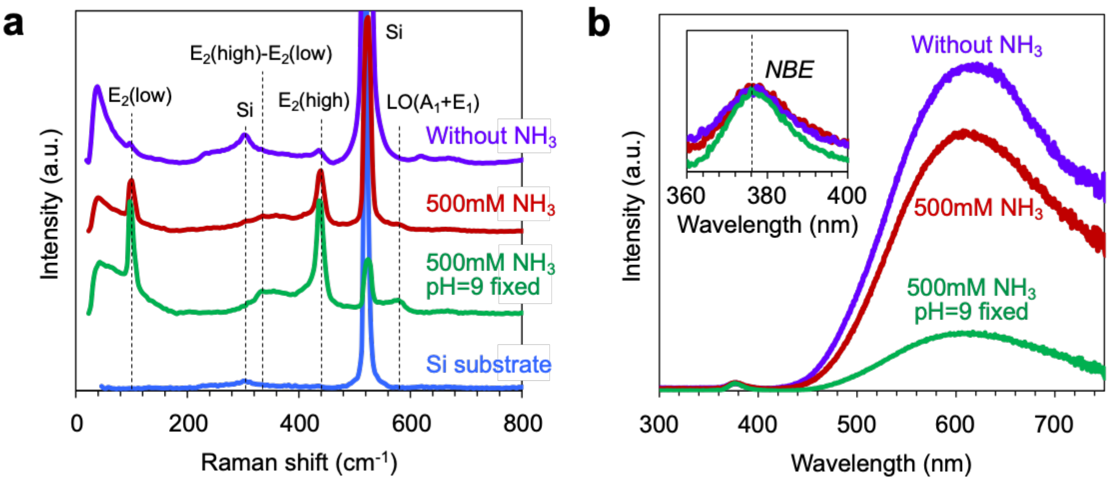

Figure 6. Effects of ammonia addition and pH control on physical properties of ZnO nanowires. (a) Raman spectra data and (b) PL spectra data.

Without NH_3	**500mM NH_3**	**500mM NH_3 pH=9 fixed**
FWHM of E_2(high) peak (cm^{-1})		
16.7	15.7	14.8

Table 1. FWHM of E2(high) peaks for Raman spectroscopy.

Next we question why the critical concentration for lateral crystal growth of nanowires shifts to the lower value from 5 mM to 2 mM with the ammonia addition. This effect cannot be interpreted in terms of our above model based on reduced molar ratio of zinc hydroxide complex ions. Here we consider the difference of pH values due to the ammonia addition to explain this effect. An effective surface charge of crystal plane varies from a positive value to a negative value below and above an isoelectric point (IEP)32,33. It has been reported that IEP value for (0001) plane of ZnO is reported to be 8.7±0.2, which is lower than that for (1010) plane-10.2±0.232,33. In other words, the effective surface charge of (1010) plane is always higher than that of (0001) plane at moderate pH range. At pH range 10–11 for ammonia addition experiments, both crystal planes must be charged more negatively than those at pH range 6.5–8 for experiments without ammonia addition. As seen in the populations of ionic species in aqueous solution, for ammonia addition experiments at pH range 10–11, the major positively charged ions are zinc ammonia complex ions-Zn $(NH_3)_4^{2+}$, and the major negatively charged ions are NO_3^-. On the other hand, for experiments without ammonia addition at pH range 6.5–8, the major positively charged ions are -Zn^{2+}, and the major negatively charged ions are NO_3^-. Since the crystal planes of ZnO at pH range-10–11 should be negatively charged, the major positively charged ions-Zn $(NH_3)_4^{2+}$ should act as a counter ion, forming an electric double layer onto crystal planes. In this case, the rate limiting process for ZnO nanowire crystal growth is a ligand exchange reaction from zinc ammonia complexes surrounding the nanowire surface to hydroxide complexes. On the other hand, the major counter ions on positively charged crystal planes at pH range 6.5–8 are NO_3^-, which do not contain Zn. In this case, the diffusion of zinc hydroxide complex ions is the rate limiting process for ZnO nanowire crystal growth. Tus, these rather contrasting results as to a polarity infers that the critical concentration for lateral crystal growth of nanowires is reduced due to the accumulated positively charged Zn source ions at the crystal growth interface.

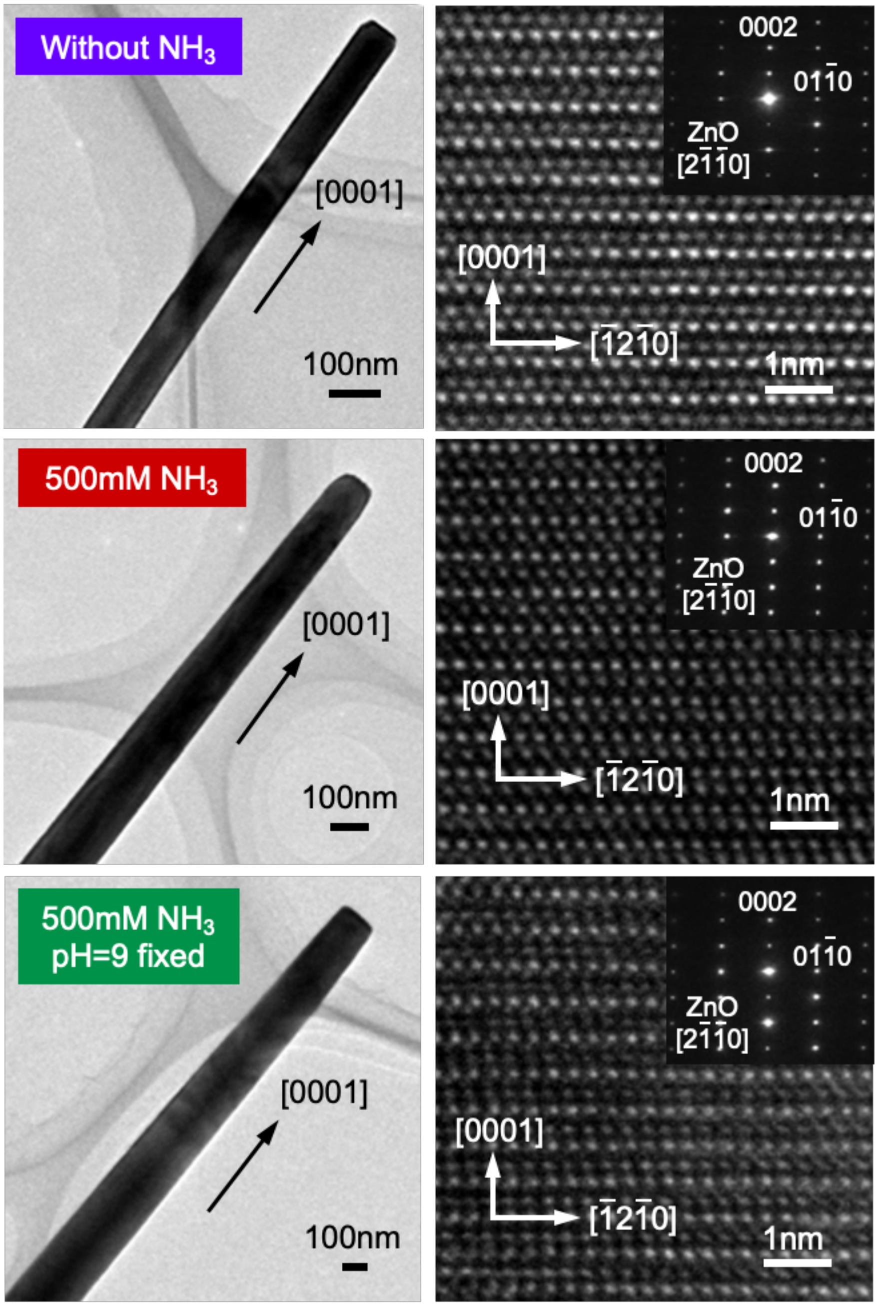

Figure 7. Effect of ammonia addition and pH control on TEM images of ZnO nanowires.

Next, we explain how the growth rate of ZnO nanowires can be enhanced when we control the zinc complex concentration within "concentration window". The increased nanowire growth rate seems to be contradictive since a nanowire heterogeneous nucleation rate is reduced by a reduction of precursor complex (Zn $(OH)_x$) concentrations. To explain this apparently contradictory observations of a reduced nanowire heterogeneous nucleation rate and an increased growth rate above the nucleation threshold, we consider the surface polarity variation and the distribution of zinc complex ion species. We propose a model based on a fast rate limiting process of a ligand exchange reaction between zinc ammonia complexes and hydroxide complexes ($Zn(NH_3)_x$ + H_2O → $Zn(OH)_x$ + $NH_3(OH)$ from a diffusion dominant process. In the presence of excessive ammonia-500mM, the major zinc complexes are zinc ammonia complexes, as calculated in Fig. 4. Since zinc hydroxide complexes are a direct precursor for ZnO crystal growth, a ligand exchange reaction between zinc ammonia complexes and hydroxide complexes becomes a rate limiting process for the crystal growth. Considering the crystal growth situation near the interface, the zinc hydroxide complexes are surrounded by a plenty of zinc ammonia complexes. Since an equiblium zinc hydroxide complex concentration is substantially lower than that of zinc ammonia complexes, the consumed zinc hydroxide complex for crystal growth can be simultaneously compensated by a plenty of surrounding zinc ammonia complexes via the ligand exchange reaction. Considering the equiblium molar ratio between the two zinc complexes as calculated in Fig. 4, the reaction must be rather dynamic. Therefore, this fast ligand exchange reaction is important to understand the nanowire growth rate enhancement with ammonia addition. Based on this model, we further enhance a nanowire growth rate. Consider the thermodynamic calculation data (Fig. 4) as to the equilibrium molar ratio of zinc hydroxide complex ions when varying PH. As seen in Fig. 4b, the equilibrium molar ratio of zinc hydroxide complex ions can be further reduced at pH=9 from pH=10–11 for experiments in Fig. 3b. Therefore, we control the pH value by using HNO_3. Figure 5 shows the Zn concentration dependence data of nanowire morphology when the pH value is set to be 9. As can be seen, the growth rate is drastically enhanced up to 2000 nm/h with maintaining the nanowire morphology, which is higher than 570 nm/h in Fig. 3b with ammonia addition and 140 nm/h in Fig. 3a without ammonia addition. As to the mechanism, looking at the critical concentration for nanowire growth is interesting, which is further increased to

10mM. In fact, this value is almost 10 times higher than that for experiments (with ammonia addition at pH=10–11) in Fig. 3b and 100 times higher than that for experiments (without ammonia at pH=6.5–8) in Fig. 3a. These results highlight that controlling zinc complex concentration with pH control can further enhance the nanowire growth rate via further reducing the equilibrium molar ratio of zinc hydroxide complex ions. The pH control further narrows the width of "concentration window".

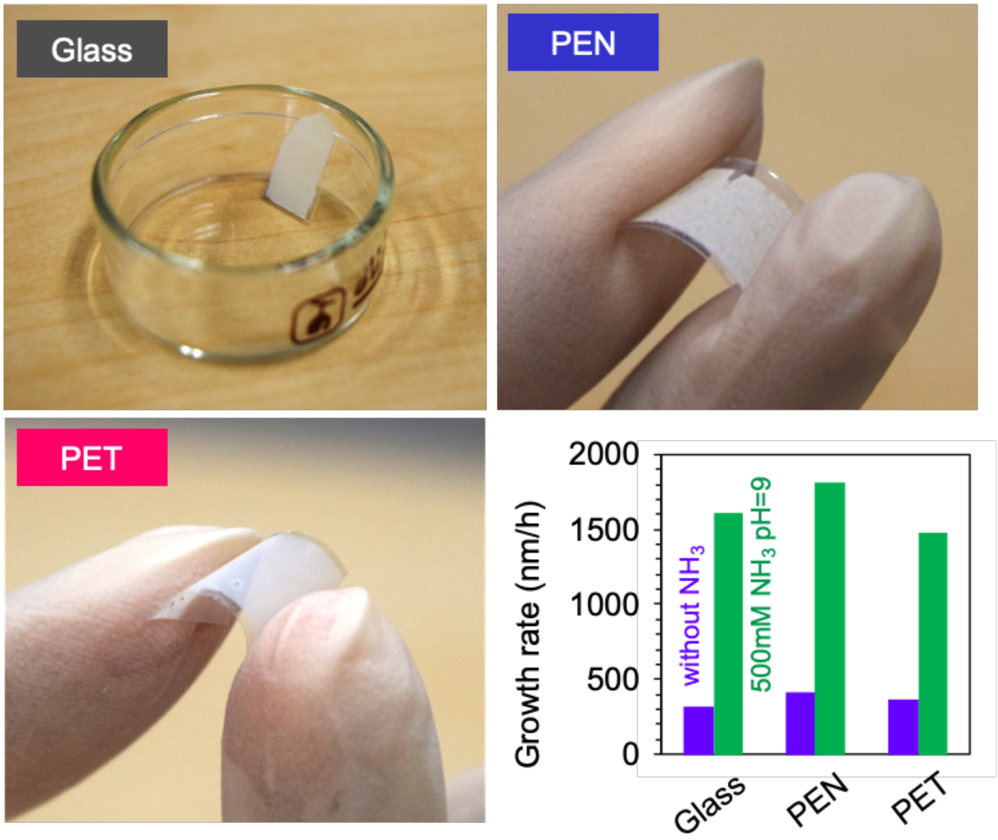

Figure 8. Applicability of the present strategy for hydrothermal ZnO nanowire growth for various substrates including glass, PEN and PET substrates (growth time: 5h, growth temperature:95°C, and Zn concentration: 20mM). For these experiments, the ZnO seed layers with polycrystalline form are deposited by sputtering at room temperature.

Effect of ammonia addition on physical properties of nanowires. Finally, we examine the effect of ammonia addition on the physical properties of fabricated ZnO nanowires. Figure 6 show the Raman spectra data and the photoluminescence (PL) spectra data of fabricated ZnO nanowires. All measurements are performed at room temperature. For Raman spectroscopy measurement, we utilize a laser with excitation wavelength of 532 nm. The observed peaks are assigned as E2 (low), E2 (high), A1 (TO), A1 (LO), LO (A1+E1), E2 (high) - E2 (low) phonon modes, which are prominent peaks of wurtzite ZnO structure.[34–36] We utilize E2 (high) peak to evaluate the crystalline quality of ZnO nanowires, which is attributed to the vibration of oxygen sublattice.[34,35] The full width half maximum (FWHM) of high frequency E2 mode (E2 (high)) peaks tends to decrease for ammonia addition and pH control, as shown in Table 1, highlighting the improvement of crystallinity. For the PL spectra data of fabricated ZnO nanowires, the broad peaks are commonly observed at the wavelength range of 500–750 nm, which are related to the deep level defects of ZnO. The intensity of spectra is normalized at near band edge emission (NBE) peaks as shown in inset. We find that the intensity of defect peaks tends to decrease by ammonia addition and pH control while the wavelength of both the NBE peaks and the defect peaks are almost unchanged, indicating the improvement of crystallinity as consistent with the Raman spectra data. Figure 7 shows the TEM images of fabricated ZnO nanowires. As can be seen, all ZnO nanowires consistently showed the single crystallinity. The TEM images show a tapering on both ammonia (and HNO_3) addition samples. This is because of narrowed concentration window width, since the occurrence of film growth at nanowire sidewall tends to be not negligible in such narrowed concentration window. All data consistently demonstrate that the ammonia addition and pH control increase the crystallinity of ZnO nanowires. These trends are contradictive to the previous report of which the crystallinity of hydrothermal ZnO nanowires decreases by the ammonia addition[37]. One possible reason to explain these contradictive results is the difference of lateral growth. Since Watanabe et al. reported that the crystal grown on (1010) plane contains more crystal imperfections than that grown on (0001) plane,[38] the decrease of crystallinity in previous study is presumably due to the promotion of crystal growth on (1010) plane by ammonia addition. On the other hand, in this study, we suppress the lateral growth by precisely control the Zn concentration within the “concentration window”. Although further systematic investigations are needed to elucidate the exact roles ammonia and pH on the crystallinity of hydrothermal ZnO nanowires, these results indicate that “concentration window” principle allows us not only to enhance the anisotropic crystal growth but also to elucidate the intrinsic property of hydrothermal ZnO nanowires. All data consistently demonstrate that the ammonia addition does not significantly alter the physical properties of ZnO nanowires. In addition, we examine the applicability of the present method for various substrates including glass, flexible polyethylene naphthalate (PEN) and polyethylene terephthalate (PET) substrates, as shown in Fig. 8. Since the applicability of nanowire arrays on flexible substrates has been demonstrated,[39] the present methodology would further promote such applications of nanowires.

3.5 Conclusion

In summary, we show the effect of ammonia addition on the width of “concentration window” using conventional hydrothermal ZnO nanowire growth. We found that the addition of ammonia substantially narrows the width of “concentration window”. Within the narrow range of zinc complex concentration, we found a significant enhancement of growth rate (up to 2000 nm/h) of ZnO nanowires. This concept of narrowed “concentration window” would be useful especially when it is necessary to increase a growth rate of hydrothermal ZnO nanowires without any additional equipment. The narrowed “concentration window” and the resultant growth enhancement by an ammonia addition can be understood in terms of two synchronized effects of both a reduction of zinc hydroxide complex concentration and a fast rate limiting process of ligand exchange between different zinc complexes when the critical nucleation emerges.

3.6 References

(1) Yeom, B.; Sain, T.; Lacevic, N.; Bukharina, D.; Cha, S.-H.; Waas, A. M.; Arruda, E. M.; Kotov, N. A. Abiotic Tooth Enamel. *Nature* **2017**, *543* (7643), 95–98.

(2) Wu, W.; Wen, X.; Wang, Z. L. Taxel-Addressable Matrix of Vertical-Nanowire Piezotronic Transistors for Active and Adaptive Tactile Imaging. *Science (80-.).* **2013**, *340* (6135), 952–957.

(3) Qin, Y.; Wang, X.; Wang, Z. L. Microfibre–Nanowire Hybrid Structure for Energy Scavenging. *Nature* **2008**, *451* (7180), 809–813.

(4) Wei, Y.; Xu, C.; Xu, S.; Li, C.; Wu, W.; Wang, Z. L. Planar Waveguide−Nanowire Integrated Three-Dimensional Dye-Sensitized Solar Cells. *Nano Lett.* **2010**, *10* (6), 2092–2096.

(5) Xu, S.; Wang, Z. L. One-Dimensional ZnO Nanostructures: Solution Growth and Functional Properties. *Nano Research* **2011**, *15*, 1013–1098.

(6) Vayssieres, L. Growth of Arrayed Nanorods and Nanowires of ZnO from Aqueous Solutions. *Adv. Mater.* **2003**, *15* (5), 464–466.

(7) Greene, L. E.; Law, M.; Goldberger, J.; Kim, F.; Johnson, J. C.; Zhang, Y.; Saykally, R. J.; Yang, P. Low-Temperature Wafer-Scale Production of ZnO Nanowire Arrays. *Angew. Chem. Int. Ed.* **2003**, *42* (26), 3031–3034.

(8) Heo, Y. W.; Varadarajan, V.; Kaufman, M.; Kim, K.; Norton, D. P.; Ren, F.; Fleming, P. H. Site-Specific Growth of Zno Nanorods Using Catalysis-Driven Molecular-Beam Epitaxy. *Appl. Phys. Lett.* **2002**, *81* (16), 3046–3048.

(9) Yao, B. D.; Chan, Y. F.; Wang, N. Formation of ZnO Nanostructures by a Simple Way of Thermal Evaporation. *Appl. Phys. Lett.* **2002**, *81* (4), 757–759.

(10) Huang, M. H.; Wu, Y.; Feick, H.; Tran, N.; Weber, E.; Yang, P. Catalytic Growth of Zinc Oxide Nanowires by Vapor Transport. *Adv. Mater.* **2001**, *13* (2), 113–116.

(11) Yanagida, T.; Marcu, A.; Matsui, H.; Nagashima, K.; Oka, K.; Yokota, K.; Taniguchi, M.; Kawai, T. Enhancement of Oxide VLS Growth by Carbon on Substrate Surface. *J. Phys. Chem. C* **2008**, *112* (48), 18923–18926.

(12) Klamchuen, A.; Suzuki, M.; Nagashima, K.; Yoshida, H.; Kanai, M.; Zhuge, F.; He, Y.; Meng, G.; Kai, S.; Takeda, S.; Kawai, T.; Yanagida, T. Rational Concept for Designing Vapor-Liquid-Solid Growth of Single Crystalline Metal Oxide Nanowires. *Nano Lett.* **2015**, *15* (10), 6406–6412.

(13) Zhu, Z.; Suzuki, M.; Nagashima, K.; Yoshida, H.; Kanai, M.; Meng, G.; Anzai, H.; Zhuge, F.; He, Y.; Boudot, M.; Takeda, S.; Yanagida, T. Rational Concept for Reducing Growth Temperature in Vapor–Liquid–Solid Process of Metal Oxide Nanowires. *Nano Lett.* **2016**, *16* (12), 7495–7502.

(14) Zhang, S.; Shen, Y.; Fang, H.; Xu, S.; Song, J.; Wang, Z. L. Growth and Replication of Ordered ZnO Nanowire Arrays on General Flexible Substrates. *J. Mater. Chem.* **2010**, *20* (47), 10606.

(15) Cheng, J. J.; Nicaise, S. M.; Berggren, K. K.; Gradečak, S. Dimensional Tailoring of Hydrothermally Grown Zinc Oxide Nanowire Arrays. *Nano Lett.* **2016**, *16* (1), 753–759.

(16) He, Y.; Yanagida, T.; Nagashima, K.; Zhuge, F.; Meng, G.; Xu, B.; Klamchuen, A.; Rahong, S.; Kanai, M.; Li, X.; Suzuki, M.; Kai, S.; Kawai, T. Crystal-Plane Dependence of Critical Concentration for Nucleation on Hydrothermal ZnO Nanowires. *J. Phys. Chem. C* **2013**, *117* (2), 1197–1203.

(17) Liu, B.; Zeng, H. C. Hydrothermal Synthesis of ZnO Nanorods in the Diameter Regime of 50 Nm. *J. Am. Chem. Soc.* **2003**, *125* (15), 4430–4431.

(18) Joo, J.; Chow, B. Y.; Prakash, M.; Boyden, E. S.; Jacobson, J. M. Face-Selective Electrostatic Control of Hydrothermal Zinc Oxide Nanowire Synthesis. *Nat. Mater.* **2011**, *10* (8), 596–601.

(19) Xu, S.; Adiga, N.; Ba, S.; Dasgupta, T.; Wu, C. F. J.; Wang, Z. L. Optimizing and Improving the Growth Quality of ZnO Nanowire Arrays Guided by Statistical Design of Experiments. *ACS Nano* **2009**, *3* (7), 1803–1812.

(20) Yamabi, S.; Imai, H. Growth Conditions for Wurtzite Zinc Oxide Films in Aqueous Solutions. *J. Mater. Chem.* **2002**, *12* (12), 3773–3778.

(21) Xu, S.; Wei, Y.; Kirkham, M.; Liu, J.; Mai, W.; Davidovic, D.; Snyder, R. L.; Wang, Z. L. Patterned Growth of Vertically Aligned ZnO Nanowire Arrays on Inorganic Substrates at Low Temperature without Catalyst. *J. Am. Chem. Soc.* **2008**, *130* (45), 14958–14959.

(22) Xu, S.; Lao, C.; Weintraub, B.; Wang, Z. L. Density-Controlled Growth of Aligned ZnO Nanowire Arrays by Seedless Chemical Approach on Smooth Surfaces. *J. Mater. Res.* **2008**, *23* (8), 2072–2077.

(23) Zhang, D.; Wang, S.; Cheng, K.; Dai, S.; Hu, B.; Han, X.; Shi, Q.; Du, Z.

Controllable Fabrication of Patterned ZnO Nanorod Arrays: Investigations into the Impacts on Their Morphology. *ACS Appl. Mater. Interfaces* **2012**, *4* (6), 2969–2977.

(24) Govender, K.; Boyle, D. S.; Kenway, P. B.; O'Brien, P. Understanding the Factors That Govern the Deposition and Morphology of Thin Films of ZnO from Aqueous Solution. *J. Mater. Chem.* **2004**, *14* (16), 2575–2591.

(25) Xu, C.; Shin, P.; Cao, L.; Gao, D. Preferential Growth of Long ZnO Nanowire Array and Its Application in Dye-Sensitized Solar Cells. *J. Phys. Chem. C* **2010**, *114* (1), 125–129.

(26) Akhavan, O.; Mehrabian, M.; Mirabbaszadeh, K.; Azimirad, R. Hydrothermal Synthesis of ZnO Nanorod Arrays for Photocatalytic Inactivation of Bacteria. *J. Phys. D. Appl. Phys.* **2009**, *42* (22), 225305.

(27) Richardson, J. J.; Lange, F. F. Controlling Low Temperature Aqueous Synthesis of ZnO. 1. Thermodynamic Analysis. *Cryst. Growth Des.* **2009**, *9* (6), 2570–2575.

(28) Richardson, J. J.; Lange, F. F. Controlling Low Temperature Aqueous Synthesis of ZnO. 2. A Novel Continuous Circulation Reactor. *Cryst. Growth Des.* **2009**, *9* (6), 2576–2581.

(29) Xu, F.; Yuan, Z. Y.; Du, G. H.; Ren, T. Z.; Bouvy, C.; Halasa, M.; Su, B. L. Simple Approach to Highly Oriented ZnO Nanowire Arrays: Large-Scale Growth, Photoluminescence and Photocatalytic Properties. *Nanotechnology* **2006**, *17* (2), 588–594.

(30) Syrrokostas, G.; Govatsi, K.; Yannopoulos, S. N. High-Quality, Reproducible ZnO Nanowire Arrays Obtained by a Multiparameter Optimization of Chemical Bath Deposition Growth. *Cryst. Growth Des.* **2016**, *16* (4), 2140–2150.

(31) Erdélyi, R.; Nagata, T.; Rogers, D. J.; Teherani, F. H.; Horváth, Z. E.; Lábadi, Z.; Baji, Z.; Wakayama, Y.; Volk, J. Investigations into the Impact of the Template Layer on ZnO Nanowire Arrays Made Using Low Temperature Wet Chemical Growth. *Cryst. Growth Des.* **2011**, *11* (6), 2515–2519.

(32) Kunze, C.; Valtiner, M.; Michels, R.; Huber, K.; Grundmeier, G. Self-Localization of Polyacrylic Acid Molecules on Polar ZnO (0001)–Zn Surfaces. *Phys. Chem. Chem. Phys.* **2011**, *13* (28), 12959.

(33) Valtiner, M.; Borodin, S.; Grundmeier, G. Stabilization and Acidic Dissolution Mechanism of Single-Crystalline ZnO (0001) Surfaces in Electrolytes Studied by *In-*

Situ AFM Imaging and *Ex-Situ* LEED. *Langmuir* **2008**, *24* (10), 5350–5358.

(34) Rana, A. K.; Kumar, Y.; Rajput, P.; Jha, S. N.; Bhattacharyya, D.; Shirage, P. M. Search for Origin of Room Temperature Ferromagnetism Properties in Ni-Doped ZnO Nanostructure. *ACS Appl. Mater. Interfaces* **2017**, *9* (8), 7691–7700.

(35) Lupan, O.; Postica, V.; Gröttrup, J.; Mishra, A. K.; de Leeuw, N. H.; Carreira, J. F. C.; Rodrigues, J.; Ben Sedrine, N.; Correia, M. R.; Monteiro, T.; Cretu, V.; Tiginyanu, I.; Smazna, D.; Mishra, Y. K.; Adelung, R. Hybridization of Zinc Oxide Tetrapods for Selective Gas Sensing Applications. *ACS Appl. Mater. Interfaces* **2017**, *9* (4), 4084–4099.

(36) Wang, J. B.; Huang, G. J.; Zhong, X. L.; Sun, L. Z.; Zhou, Y. C.; Liu, E. H. Raman Scattering and High Temperature Ferromagnetism of Mn-Doped ZnO Nanoparticles. *Appl. Phys. Lett.* **2006**, *88* (25), 252502.

(37) Chen, L. Y.; Yin, Y. T.; Chen, C. H.; Chiou, J. W. Influence of Polyethyleneimine and Ammonium on the Growth of ZnO Nanowires by Hydrothermal Method. *J. Phys. Chem. C* **2011**, *115* (43), 20913–20919.

(38) Watanabe, K.; Nagata, T.; Oh, S.; Wakayama, Y.; Sekiguchi, T.; Volk, J.; Nakamura, Y. Arbitrary Cross-Section SEM-Cathodoluminescence Imaging of Growth Sectors and Local Carrier Concentrations within Micro-Sampled Semiconductor Nanorods. *Nat. Commun.* **2016**, *7* (1), 10609.

(39) Yasui, T.; Yanagida, T.; Ito, S.; Konakade, Y.; Takeshita, D.; Naganawa, T.; Nagashima, K.; Shimada, T.; Kaji, N.; Nakamura, Y.; Thiodorus, I. A.; He, Y.; Rahong, S.; Kanai, M.; Yukawa, H.; Ochiya, T.; Kawai, T.; Baba, Y. Unveiling Massive Numbers of Cancer-Related Urinary-MicroRNA Candidates via Nanowires. *Sci. Adv.* **2017**, *3* (12), e1701133.

Chapter IV

Synthesis of Monodispersedly Sized ZnO Nanowires from Randomly Sized Seeds

4.1 Abstract

We demonstrate the facile, rational synthesis of monodispersed sized zinc oxide (ZnO) nanowires from randomly sized seeds by hydrothermal growth. Uniformly shaped nanowire tips constructed in ammonia-dominated alkaline conditions serve as a foundation for the subsequent formation of the monodisperse nanowires. By precisely controlling the sharp tip formation and the nucleation, our method substantially narrows the distribution of ZnO nanowire diameters from $\sigma = 13.5$ nm down to $\sigma = 1.3$ nm and controls their diameter by a completely bottom-up method, even initiating from randomly sized seeds. The proposed concept of sharp tip based monodisperse nanowires growth can be applied to the growth of diverse metal oxide nanowires and thus paves the way for bottom-up grown metal oxide nanowires-integrated nanodevices with a reliable performance.

4.2 Introduction

Spontaneously assembled (i.e., bottom-up grown) metal oxide nanomaterials are a rapidly expanding research topic in both fundamental sciences[1-5] and interactive nanodevice applications[6-17] due to their intriguing properties and their high thermal and chemical robustness.[18] In bottom-up nanomaterials synthesis, structural control is the most fundamental challenging issue. In fact, the cost of commercial nanomaterials raises rapidly as their size distribution narrows. This is because the electrical, optical and mechanical properties of nanostructured materials are strongly influenced by their geometry.[19-24] In nanowires, in particular, the field effect becomes more relevant in electrical conduction as the diameter decreases, and the mechanical flexibility is enhanced[19,23]. Additionally, the absorption spectrum widely varies with the diameter.[21,22] These structure-induced variations in nanowire properties lead to a batch-to-batch variability in the performance of the devices. Therefore, the synthesis of monodisperse nanomaterials is strongly required for device applications with selected properties and reliable performance based on metal oxide nanomaterials.

In order to synthesize such monodisperse metal oxide nanowires, most fundamental research has been devoted to understand the principles of nanowire growth using various techniques, including vapor-phase[25-27] and solution-phase synthesis.[28-38] Many studies consistently showed the crucial importance of a homogeneously sized initial nucleation to obtain the monodisperse nanowires. For controlling the initial nucleation, a seed pre-patterning approach on substrate that defines the seed size has been demonstrated via different lithographic techniques.[33-35,39,40] However, these techniques are highly costly and restricted to operation in limited areas. This has held back the usage of bottom-up grown metal oxide nanowires in fundamental science and device applications. Therefore, an alternative lithography-free, scalable approach for synthesizing monodisperse nanowires is strongly demanded.

In this study, we demonstrate a very facile, rational synthesis of monodisperse zinc oxide (ZnO) nanowires by seed-assisted hydrothermal growth. ZnO nanowires are among the most intensively investigated metal oxide nanowires due to their outstanding electrical and chemical properties.[5,6,12-14,16,25,29] Our method enables the unprecedented growth of monodispersed sized ZnO nanowires from randomly sized seeds.

4.3 Experimental

The ZnO nanowires used in this study were fabricated via a seed-assisted hydrothermal method. Before the hydrothermal process, a ZnO seed layer with a thickness of ca. 30 nm was deposited on a SiO_2/Si (100) substrate by radio frequency (RF) sputtering at room temperature with a power of 50 W, Ar pressure of 0.3 Pa, and deposition time of 20 min. Note that a Ti layer of 1 nm was introduced between the ZnO layer and the substrate to ensure adhesion. The growth solution was prepared at room temperature by dissolving in deionized (DI) water zinc nitrate hexahydrate $Zn(NO_3)_2 \cdot 6H_2O$ (Wako, 99.0% pure), hexamethylenetetramine (HMTA) $(CH_6)_2N_4$ (Wako, 99.0% pure), and polyethylenimine (PEI) $[-CH_2CH_2NH-]_n$ with average molecular weight (m.w.) of 1800 (Aldrich, 50wt.% in H_2O); the ratio of $Zn(NO_3)_2$:HMTA:PEI = 1:1:0.1. In the two-step growth, we added 50 mM of NH_3 in step 1. The hydrothermal growth process was conducted by immersing the seed layer-coated substrate into 100 ml growth solution upside-down. The pH value of the solution was measured before nanowire growth. A growth temperature of 95 °C was maintained during the whole growth process. The growth time and Zn concentration C_{Zn} were varied to unravel their contribution to the nanowire growth. In the two-step growth, the samples were rinsed in DI water after the first step and moved into the solution for the second one without prior drying. After the whole growth, the samples were rinsed in DI water and dried with an air blower. The morphology of the ZnO nanostructures was characterized by field emission scanning electron microscopy (FESEM, JEOL JSM-7610F 30 kV). To characterize the crystallinity and the tip angle of ZnO nanowires, transmission electron microscopy (TEM, JEOL JEM-2100F and ARM-200F 200 kV) was used. The nanowire diameter and the tip angle were statistically evaluated from 100 nanowires. Visual MINTEQ software was employed to calculate the equilibrium concentrations of ionic species in the growth solution at given temperature and pH conditions.

4.4 Results and Discussions

We serendipitously found the emergence of monodisperse ZnO nanowires from randomly sized seeds when hydrothermal synthesis[28-31,33-38] was conducted by a two-step process composed of an ammonia-added 'step 1' and an ammonia-free 'step 2'. Figure 1 (a) and (b) show typical field emission scanning electron microscopy (FESEM) images of ZnO nanowires fabricated by two-step and single-step growth, respectively. Detailed growth conditions are reported in the Experimental Section. Nanowires with a narrow diameter distribution are clearly observed when we employ the two-step growth. The details of the monodisperse ZnO nanowires are shown in figure S1. Oppositely, a wide diameter distribution is observed in the single-step-grown ZnO nanowires. These trends are evidenced by the statistical analysis of Figure 1 (c). The mean diameter d_{ave} and the standard deviation σ of the ZnO nanowires are d_{ave}=17.5 nm, σ=1.3 nm for the nanowires of Figure 1 (a) and d_{ave}=28.2 nm, σ=13.5 nm for those of Figure 1 (b), as summarized in Table 1. Such a narrow size distribution of two-step grown nanowires cannot be obtained in single-step growth, where only the nucleation rate can be controlled by tuning the precursor concentration (Figure S2)[32-34]. Note that the diameter distribution of the two-step grown nanowires becomes narrower than that of the seeds (d_{ave}=19.1 nm, σ=4.3 nm) (Figure S3). These results, obtained in absence of a specific treatment, indicate that the two-step growth allows to synthesize monodisperse ZnO nanowires even from randomly sized seeds.

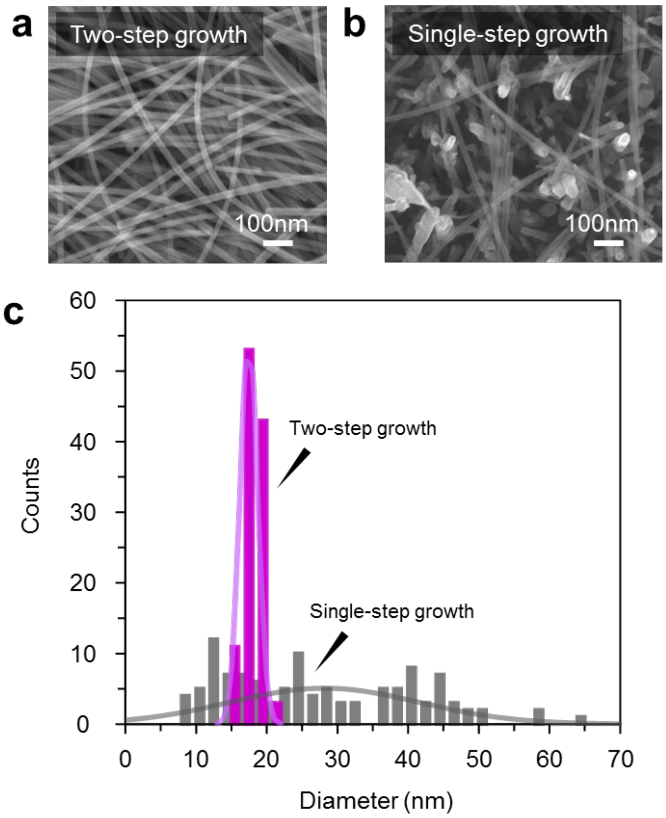

Figure 1. Typical FESEM images of the ZnO nanowires grown on a Si substrate by (a) two-step growth (with 50 mM NH_3 and $C_{Zn} = 2.5$ mM for step 1, no NH_3 and $C_{Zn} = 5$ mM for step 2) and (b) single-step growth (no NH_3 and $C_{Zn} = 5$ mM). In the two-step growth, the growth time for step 1 and step 2 are 3 and 12 h, respectively. The single-step growth time is 12 h. (c) The diameter distribution of (a) and (b).

In order to find out if any of the growth processes crucially contributes to the synthesis of monodisperse ZnO nanowires, we examined each in detail. Figure 2 (a) shows the FESEM images of ZnO nanowires grown by step 1 only, step 2 only, two-step process (step 1 → step 2), and inverse two-step process (step 2 → step 1). As seen, monodisperse ZnO nanowires are only grown by a step 1 → step 2 two-step process. We found that the short, sharp-tip nanostructures are formed in the ammonia-added step 1, and the monodisperse nanowires are grown in the subsequent step 2. Note that the diameter of two-step grown nanowires is smaller than that of nanostructures grown by step 1 only. This indicates that the diameter of the two-step grown nanowires does not follow the size of the preformed seeds or nanostructures, unlike that of seed assisted grown ZnO nanowires of previous studies.[35] Figure 2 (b) shows the effect of step 1 growth time on the standard deviation and the diameter (inset) of two-step grown ZnO nanowires. In these experiments, the step 2 conditions are kept constant. In the FESEM observations of the ZnO nanostructures after step 1 (Figure S4), no morphological variation in sharp-tip ZnO nanostructures is seen when varying the step 1 growth time. On the contrary, both the diameter and the standard deviation of two-step grown nanowires continuously decrease when increasing the step 1 growth time, stabilizing after 2 hours. This shows the impact of this step in narrowing the size distribution. Thus, the results of Figure 2 (a) and (b) evidence that the ammonia-added step 1 is the crucial one to synthesize monodisperse ZnO nanowires.

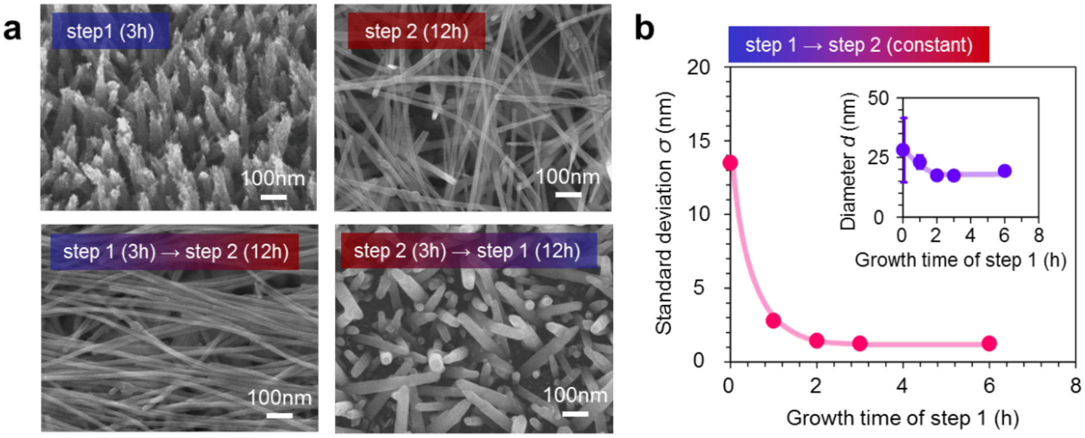

Figure 2. (a) FESEM images of the ZnO nanowires/nanostructures grown by step 1 only (upper left), step 2 only (upper right), two-step process (step 1 → step 2, lower left), and inversed two-step process (step 2 → step 1, lower right), respectively. The growth time for step 1 and step 2 is 3 h and 12 h, respectively. Note that the growth time of step 1 and step 2 in the inversed sequence is also inverted in order to clarify the effect of the growth sequence independently from the growth time. (b) Standard deviation σ for the diameter of the two-step grown ZnO nanowires as a function of the growth time of step 1. The inset graph shows the nanowire diameters d. For this experiment, the growth time of step 2 is kept constant. In all the above experiments, the ammonia and Zn concentrations were NH_3 50 mM, C_{Zn}=2.5 mM for step 1 and no NH_3, C_{Zn}=5 mM for step 2, respectively.

Because the monodisperse ZnO nanowires are grown from the sharp-tip nanostructures obtained by the ammonia-added step 1, the formation of sharp tips is a key process in the monodisperse nanowire growth. In fact, monodisperse nanowires are grown only when the sharp tips are formed (Figure S5). Here, we investigate the sharp tip formation in the ammonia-added step 1. Since zinc hydroxide $[Zn(OH)_m]^{2-m}$ ions and zinc amine complex $[Zn(NH_3)_n]^{2+}$ ions are stabilized in the ammonia-added alkaline solution (Figure S6), it is natural to assume that the formation of sharp tips is related to the simultaneous dissociation of ZnO during crystal growth. In fact, sharp-tip ZnO nanowire formation in ammonia-contained alkaline solution has been reported previously, although the details of the formation mechanism are still controversial[41-44]. To elucidate the role of sharp tip formation in ammonia, we performed ammonia-based chemical etching of the flat-top ZnO nanowires, as shown in Figure 3. Figure 3 (a) shows a time series of FESEM images of the ammonia etched ZnO nanowires and the subsequent nanowire growth. When increasing the etching time, the nanowire tip tends to sharpen without significant modifications of the stem nanowire diameter. In addition, we find that monodisperse nanowires are successfully grown by forming sharp tips even if their diameter distribution is wide (σ= 21.1 nm, Figure S7). The sharp tip formation and the nanowire growth from the tip are also confirmed by the transmission electron microscopy (TEM) characterization of Figure 3 (b). Since the sharp tips are not formed by NaOH etching (Figure S8), the key role in sharp tip formation is played by ammonia rather than by the pH value. Thus, these results reveal that the ammonia-formed sharp tips serve as a foundation for the growth of monodisperse nanowires.

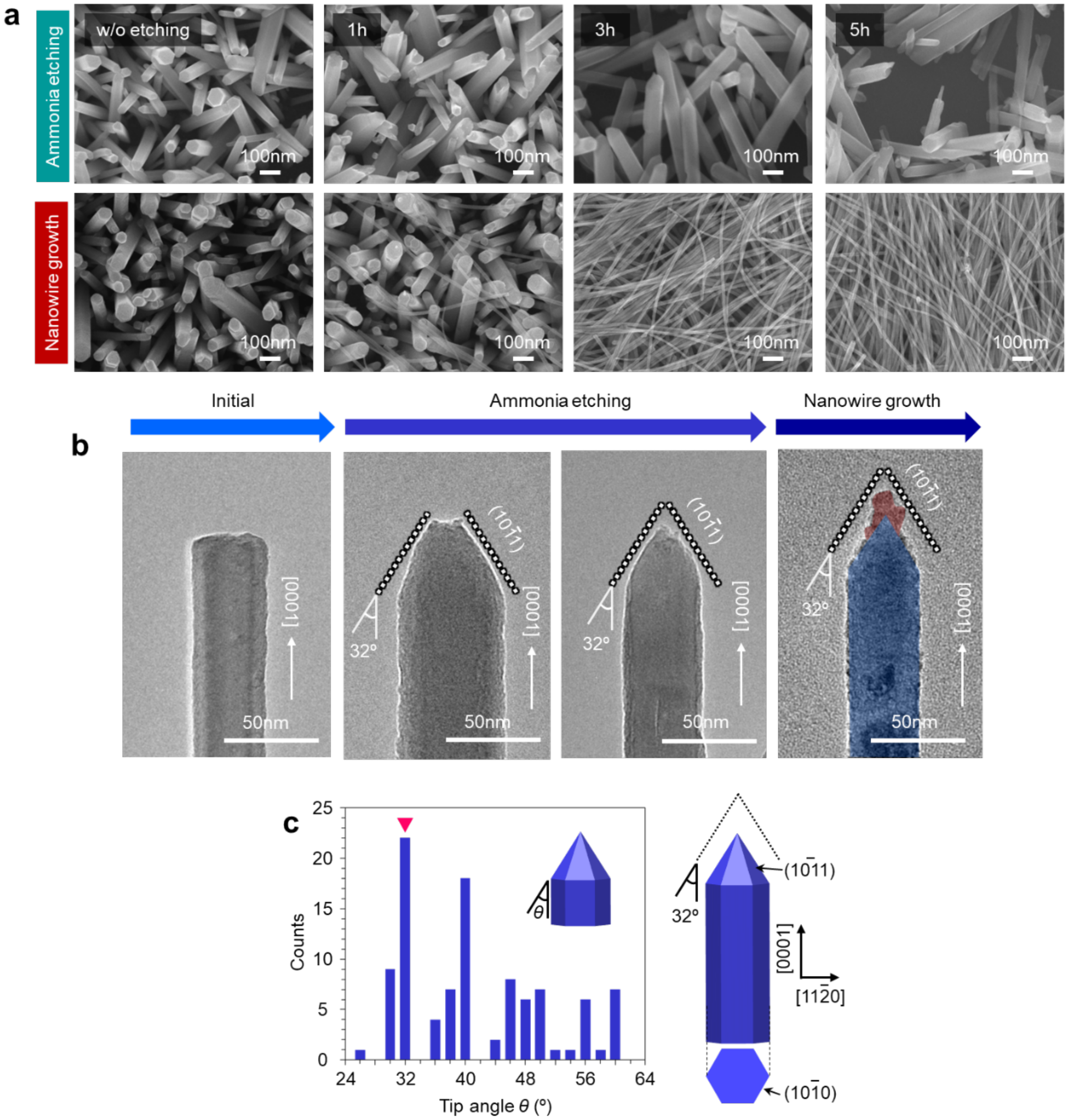

Figure 3. (a) Time series of FESEM images for the ammonia-based chemical etching (pH=11.4) of the ZnO nanowires (upper series) and the results of subsequent nanowires growth (lower series). In this experiment, the ZnO nanowires with flat top are first fabricated by no NH_3 and C_{Zn}=25 mM for 12 h before the chemical etching, and the subsequent nanowire growth is conducted with no NH_3 and C_{Zn}=5 mM for 12 h. (b) TEM images of the initial ZnO nanowires, the etched ZnO nanowires and the ZnO nanowires after the subsequent growth. The chemically etched part and the subsequently grown part are colored by blue and red, respectively. (c) Distribution of ZnO nanowires tip angle

after performing ammonia-etching for 3 h. Structural information of the ZnO nanowires exposing the $(10\bar{1}1)$ plane is also shown.

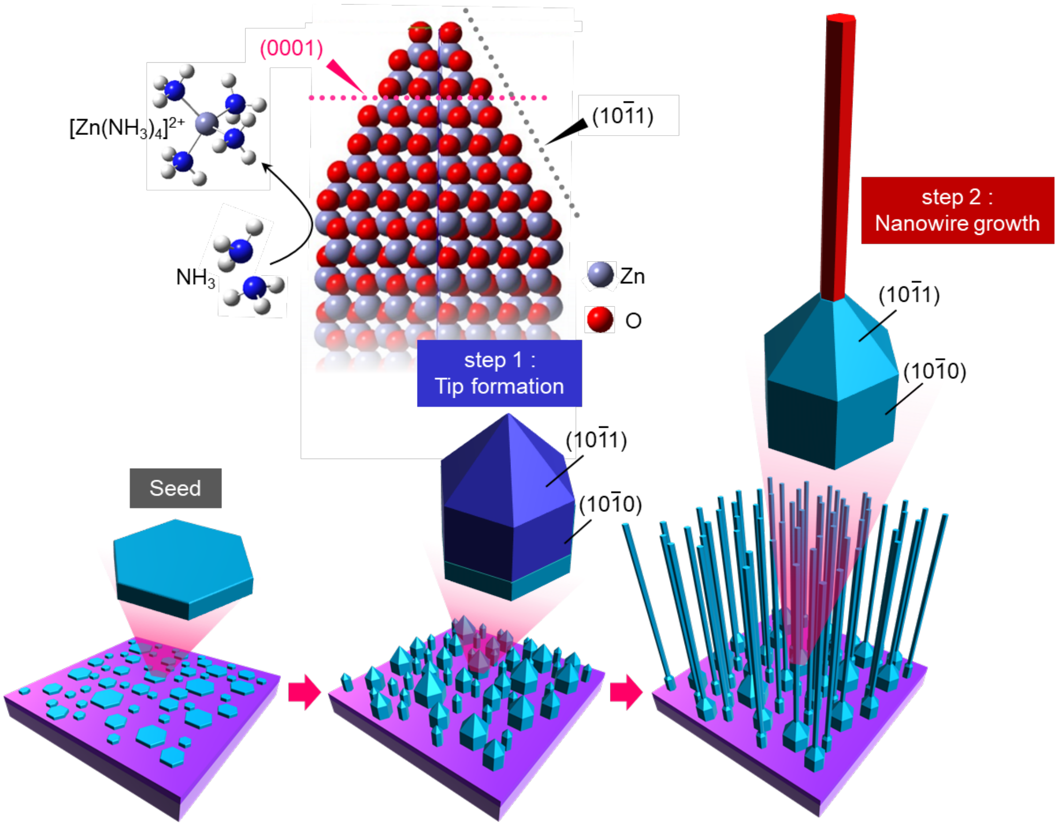

Figure 4. Schematic illustration of the growth process of the monodisperse ZnO nanowires from randomly sized seeds. The sharp tips faceted by $\{10\bar{1}1\}$ planes are formed by ammonia-etching, associated with the formation of $[Zn(NH_3)_4]^{2+}$ ions via the coordination of NH_3 molecules to the Zn sites. The energetically unfavorable tips serve as nucleation points for the subsequent nanowire growth. The nucleation on uniformly shaped and spatially separated seed/nanowire tips are of critical importance for the monodisperse nanowires growth.

We now discuss why the monodisperse ZnO nanowires can be grown on the sharp-tip nanostructures/nanowires. From the TEM images and the tip angle distribution of Figure 3 (b) and (c), respectively, we found that chemical etching maintains the crystal planes tilted by 32° from the [0001] growth direction, consistently with the ZnO $\{10\bar{1}1\}$ planes.[45] Combining such $\{10\bar{1}1\}$ planes lead to the formation of uniformly shaped sharp tips independently of the initial size and morphology of the seeds/nanowires. Next, we consider the nanowire growth from sharp tips, which is a crucial mechanism for the formation of monodisperse nanowires. Since the tips of the seeds/nanowires have energetically unfavorable dangling bonds, nucleation preferentially occurs at such bonds in order to eliminate the tips. Regarding the size and shape of the nuclei, these are determined by minimizing their total Gibbs free energy. According to the SEM image (Figure S7), the ZnO nanowires mainly expose the (0001) and $(10\bar{1}0)$ planes, with the latter appearing to be energetically favored over the former in ammonia-free growth conditions. In this case, i.e., when the degree of supersaturation is sufficiently low, nanowires with a small diameter grow at the tips to minimize the appearance of the (0001) plane. Because the (0001) plane is no longer found after forming the sharp tips in the ammonia-added step 1, the nuclei size is determined solely by the thermodynamic conditions; thereby, a homogeneously sized nucleation can be obtained at the tip of the nanowires. Recently, Demes *et al.*[46] found that anisotropic nanowire growth starts when the nuclei size is around 20-25 nm at a relatively low concentration of Zn precursor (C_{Zn} ~ 1 mM) and a growth temperature of 90 °C. Our growth conditions ($C_{Zn} = 5$ mM and T = 95 °C) and the observed nanowire diameter ($d_{ave} = 17.5$ nm) are similar to these, suggesting that the size of the monodisperse nanowires grown in step 2 is governed by the thermodynamic conditions. Note that despite the similar growth conditions, Demes *et al.* did not observe monodispersed sizes of the nanowires. This might be due to the presence of randomly sized (0001) planes on the seeds, assuming that the diameter of each nanowire depends on the size of the pre-existing (0001) plane. Furthermore, in their study, adjacent nuclei merged during the growth of nanowires, which is detrimental for synthetizing monodisperse nanowires. The tips of our seeds/nanowires are loosely distributed, differently from the densely deposited grains of the conventional seed layer. This promotes the growth of separate nanowires by suppressing the merging of the nuclei. Thus, homogeneously sized nucleation from spatially separated nanowire tips significantly contributes to the synthesis of monodisperse nanowires, as schematically shown in Figure 4.

In the growth mechanism, the size of the nanowires must be monodispersed as long as the size of the nanowires grown on the tips does not exceed the diameter of the stem seeds/nanowires. To confirm this hypothesis, we examine the size of the monodisperse ZnO nanowires. As reported in our previous study, [32,33] the morphology of ZnO nanowires can be designed by controlling the competitive nucleation from the (0001) and $(10\bar{1}0)$ planes, i.e., by tuning the supersaturation degree of the growth solution. This is because a critical concentration for a nucleation strongly depends on interfacial energy of crystal planes, e.g. (0001) plane with higher interfacial energy has lower free energy barrier than $(10\bar{1}0)$ plane with lower interfacial energy (the detailed mechanism is described in supporting information). In particular, the nanowire diameter is varied by controlling the Zn precursor concentration at above the critical concentration for the $(10\bar{1}0)$ plane nucleation. Figure 5 (a) shows the dependence of the Zn concentration on the diameter of single-step nanowires grown in ammonia-free conditions. Threshold concentrations of 3 mM for nanowire growth and 5 mM for lateral growth are seen, corresponding to the critical concentrations for (0001) and $(10\bar{1}0)$ planes' nucleation, respectively. This implies that the diameter of monodisperse nanowires can be modulated by controlling the Zn concentration above 5 mM. Figure 5 (b)-(d) show the dependence of the diameter of two-step grown nanowires on the Zn concentration C_{Zn}, its magnification for C_{Zn} in the 10^0-10^2 mM range, and the dependence of the standard deviation on C_{Zn} in the same range, respectively. In this experiment, only the Zn concentration in step 2 is varied, keeping the other conditions constant (the details are reported in the caption). As expected from the results of Figure 5 (a), the nanowire diameter is successfully modulated by maintaining the standard deviation $\sigma < 2$ nm when controlling the Zn concentration at above 5 mM. We also found that the size can no longer be controlled when the diameter exceeds that of the stem nanowires at ca. 30 nm; that is, the diameter distribution greatly widens as the diameter increases up to 30 nm. In principle, the diameter of monodisperse nanowires could be controlled in a wide range by growing the nanowires at the tip of nanowires with a larger diameter. Thus, our two-step growth method provides a rational approach for the previously unreported synthesis of monodisperse metal oxide nanowires and for tuning their diameter even when starting from randomly sized seeds.

4.5 Conclusion

In conclusion, we proposed a very facile, rational synthesis of monodisperse ZnO nanowires from randomly sized seeds. Nanowire tips formed in ammonia-dominated alkaline conditions serve as a seed for the growth of the monodisperse nanowires. The shape uniformity and the spatial separation of the seed/nanowire tips is of critical importance for the growth. By a seed-engineering approach, we successfully synthesized monodisperse ZnO nanowires (σ=1.3 nm) from randomly sized seeds (σ=4.3 nm) and nanowires (σ=21.1 nm) without any high-cost lithographic techniques. The most important point of proposed method is to synthesize the sharp nanowire tips, where the size of crystal plane dominating a nanowire growth is extremely minimized. Since the size of nuclei on the sharp tips is simply dominated by thermodynamic condition, monodisperse nanowires are available by precisely controlling the nucleation event in the secondary growth step. In practice, the ammonia-etching approach utilized for the formation of sharp tips of ZnO nanowires cannot be directly applied to different metal oxide nanowires. Nevertheless, the proposed concept of two-step growth consisting of the sharp tip formation and the subsequent nucleation control on the sharp tips must be general for monodisperse nanowire synthesis in diverse metal oxide nanowires. Thus, we believe that this study paves the way for bottom-up grown metal oxide nanowires-integrated nanodevices with a reliable performance.

4.6 References

(1) Tian, Y.; Bakaul, S. R.; Wu, T. Oxide nanowires for spintronics: materials and devices. *Nanoscale* **2012**, *4*, 1529-1540.

(2) Shao, Z.; Cao, X.; Luo, H.; Jin, P. Recent progress in the phase-transition mechanism and modulation of vanadium dioxide materials. *NPG Asia Mater.* **2018**, *10*, 581-605.

(3) Nagashima, K.; Yanagida, T.; Oka, K.; Kanai, M.; Klamchuen, A.; Kim, J. S.; Park, B. H.; Kawai, T. Intrinsic Mechanisms of Memristive Switching. *Nano Lett.* **2011**, *11*, 2114-2118.

(4) Anzai, H.; Suzuki, M.; Nagashima, K.; Kanai, M.; Zhu, Z.; He, Y.; Boudot, M.; Zhang, G.; Takahashi, T.; Kanemoto, K.; Seki, T.; Shibata, N.; Yanagida, T. True Vapor−Liquid−Solid Process Suppresses Unintentional Carrier Doping of Single Crystalline Metal Oxide Nanowires. *Nano Lett.* **2017**, *17*, 4698-4705.

(5) Wang, C.; Hosomi, T.; Nagashima, K.; Takahashi, T.; Zhang, G.; Kanai, M.; Zeng, H.; Mizukami, W.; Shioya, N.; Shimoaka, T.; Tamaoka, T.; Yoshida, H.; Takeda, S.; Yasui, T.; Baba, Y.; Aoki, Y.; Terao, J.; Hasegawa, T.; Yanagida, T. Rational Method of Monitoring Molecular Transformations on Metal-Oxide Nanowire Surfaces. *Nano Lett.* **2019**, *19*, 2443-2449.

(6) Comini, E. Metal oxide nanowire chemical sensors: innovation and quality of life. *Mater. Today* **2016**, *19*, 559-567.

(7) Meng, G.; Zhuge, F.; Nagashima, K.; Nakao, A.; Kanai, M.; He, Y.; Boudot, M.; Takahashi, T.; Uchida, K.; Yanagida, T. Nanoscale Thermal Management of Single SnO_2 Nanowire: pico-Joule Energy Consumed Molecule Sensor. *ACS Sens.* **2016**, *1*, 997-1002.

(8) Koga, H.; Nagashima, K.; Huang, Y.; Zhang, G.; Wang, C.; Takahashi, T.; Inoue, A.; Yan, H.; Kanai, M.; He, Y.; Uetani, K.; Nogi, M.; Yanagida, T. Paper-Based Disposable Molecular Sensor Constructed from Oxide Nanowires, Cellulose Nanofibers, and Pencil-Drawn Electrodes. *ACS Appl. Mater. Interfaces* **2019**, *11*, 15044-15050.

(9) Kim, D.; Sakimoto, K. K.; Hong, D.; Yang, P. Artificial Photosynthesis for Sustainable Fuel and Chemical Production. *Angew. Chem. Int. Ed.* **2015**, *54*, 3259-3266.

(10) Dai, B.; Wang, J.; Xiong, Z.; Zhan, X.; Dai, W.; Li, C. C.; Feng, S.-P.; Tang, J. Programmable artificial phototactic microswimmer. *Nat. Nanotechnol.* **2016**, *11*, 1087-1092.

(11) Xie, X.; Li, Y.; Liu, Z.-Q. Haruta, M.; Shen, W. Low-temperature oxidation of CO catalysed by Co_3O_4 nanorods. *Nature* **2009**, *458*, 746-749.

(12) Qin, Y.; Wang, X.; Wang, Z. L. Microfibre–nanowire hybrid structure for energy scavenging. *Nature* **2018**, *451*, 809-813.

(13) Xu, S.; Qin, Y.; Xu, C.; Wei, Y.; Yang, R.; Wang, Z. L. Self-powered nanowire devices. *Nat. Nanotechnol.* **2010**, *5*, 366-373.

(14) Fan, F. R.; Tang, W.; Wang, Z. L. Flexible Nanogenerators for Energy Harvesting and Self-Powered Electronics. *Adv. Mater.* **2016**, *28*, 4283-4305.

(15) Yasui, T.; Rahong, S.; Motoyama, K.; Yanagida, T.; Wu, Q.; Kaji, N.; Kanai, M.; Doi, K.; Nagashima, K.; Tokeshi, M.; Taniguchi, M.; Kawano, S.; Kawai, T.; Baba, Y. DNA Manipulation and Separation in Sublithographic-Scale Nanowire Array. *ACS Nano* **2013**, *7*, 3029-3035.

(16) Yasui, T.; Yanagida, T.; Ito, S.; Konakade, Y.; Takeshita, D.; Naganawa, T.; Nagashima, K.; Shimada, T.; Kaji, N.; Nakamura, Y.; Thiodorus, I. A.; He, Y.; Rahong, S.; Kanai, M.; Yukawa, H.; Ochiya, T.; Kawai, T.; Baba, Y. Unveiling massive numbers of cancer-related urinary-microRNA candidates via nanowires. *Sci. Adv.* **2017**, *3*, e1701133.

(17) Yasui, T.; Yanagida, T.; Shimada, T.; Otsuka, K.; Takeuchi, M.; Nagashima, K.; Rahong, S.; Naito, T.; Takeshita, D.; Yonose, A.; Magofuku, R.; Zhu, Z.; Kaji, N.; Kanai, M.; Kawai, T.; Baba, Y. Engineering Nanowire-Mediated Cell Lysis for Microbial Cell Identification. *ACS Nano* **2019**, *13*, 2262-2273.

(18) Zhou, Z.; Lan, C.; Wei, R.; Ho, J. C. Transparent metal-oxide nanowires and theirapplications in harsh electronics. *J. Mater. Chem. C* **2019**, *7*, 202-217.

(19) Sahay, S.; Kumar, M. J. Diameter Dependence of Leakage Current in Nanowire Junctionless Field Effect Transistors. *IEEE Trans. Electron. Dev.* **2017**, *64*, 1330-1335.

(20) Lee, S. H.; Jo, G.; Park, W.; Lee, S.; Kim, Y.-S.; Cho, B. K.; Lee, T.; Kim, W. B. Diameter-Engineered SnO_2 Nanowires over Contact-Printed Gold Nanodots Using Size-Controlled Carbon Nanopost Array Stamps. *ACS Nano* **2010**, *4*, 1829-1836.

(21) Wang, J.; Xiong, Z.; Zhan, X.; Dai, B.; Zheng, J.; Liu, J.; Tang, J. A Silicon Nanowire as a Spectrally Tunable Light-Driven Nanomotor. *Adv. Mater.* **2017**, 29, 1701451.

(22) Mokkapati, S.; Saxena, D.; Tan, H. H.; Jagadish, C. Optical design of nanowire absorbers for wavelength selective photodetectors. *Sci. Rep.* **2015**, *5*, 15339.

(23) Asthana, A.; Momeni, K.; Prasad, A.; Yap, Y. K.; Yassar, R. S. *In situ* observation of size-scale effects on the mechanical properties of ZnO nanowires. *Nanotechnology* **2011**, *22*, 265712.

(24) Kim, D. H.; Lu, N.; Ghaffari, R.; Rogers, J. A. Inorganic semiconductor nanomaterials for flexibleand stretchable bio-integrated electronics. *NPG Asia Mater.* **2012**, *4*, e15.

(25) Huang, M. H.; Mao, S.; Feick, H.; Yan, H.; Wu, Y.; Kind, H.; Weber, E.; Russo, R.; Yang, P. Room-Temperature Ultraviolet Nanowire Nanolasers. *Science* **2001**, *292*, 1897-1899.

(26) Klamchuen, A.; Suzuki, M.; Nagashima, K.; Yoshida, H.; Kanai, M.; Zhuge, F.; He, Y.; Meng, G.; Kai, S.; Takeda, S.; Kawai, T.; Yanagida, T. Rational Concept for Designing Vapor−Liquid−Solid Growth of Single Crystalline Metal Oxide Nanowires. *Nano Lett.* **2015**, *15*, 6406-6412.

(27) Zhu, Z.; Suzuki, M.; Nagashima, K.; Yoshida, H.; Kanai, M.; Meng, G.; Anzai, H.; Zhuge, F.; He, Y.; Boudot, M.; Takeda, S.; Yanagida, T. Rational Concept for Reducing Growth Temperature in Vapor−Liquid−Solid Process of Metal Oxide Nanowires. *Nano Lett.* **2016**, *16*, 7495-7502.

(28) Joo, J.; Chow, B. Y.; Prakash, M.; Boyden, E. S.; Jacobson, J. M. Face-selective electrostatic control of hydrothermal zinc oxide nanowire synthesis. *Nat. Mater.* **2011**, *10*, 596-601.

(29) Law, M.; Greene, L. E.; Johnson, J. C.; Saykally, R.; Yang, P. Nanowire dye-sensitized solar cell. *Nat. Mater.* **2005**, *4*, 455-459.

(30) Greene, L. E.; Law, M.; Goldberger, J.; Kim, F.; Johnson, J. C.; Zhang, Y.; Saykally, R. J.; Yang, P. Low-Temperature Wafer-Scale Production of ZnO Nanowire Arrays. *Angew. Chem.* **2003**, *115*, 3139-3142.

(31) Morin, S. A.; Jin, S. Screw Dislocation-Driven Epitaxial Solution Growth of ZnO Nanowires Seeded by Dislocations in GaN Substrates. *Nano Lett.* **2010**, *10*, 3459-3463.

(32) Akihiro, Y.; Nagashima, K.; Hosomi, T.; Kanai, M.; Anzai, H.; Takahashi, T.; Zhang, G.; Yasui, T.; Baba, Y.; Yanagida, T. Water−Organic Cosolvent Effect on Nucleation of Solution-Synthesized ZnO Nanowires. *ACS Omega* **2019**, 4, 8299-8304.

(33) He, Y.; Yanagida, T.; Nagashima, K.; Zhuge, F.; Meng, G.; Xu, B.; Klamchuen, A.; Rahong, S.; Kanai, M.; Li, X.; Suzuki, M.; Kai, S.; Kawai, T. Crystal-Plane Dependence of Critical Concentration for Nucleation on Hydrothermal ZnO Nanowires. *J. Phys. Chem. C* **2013**, *117*, 1197-1203.

(34) Sakai, D.; Nagashima, K.; Yoshida, H.; Kanai, M.; He, Y.; Zhang, G.; Zhao, X.; Takahashi, T.; Yasui, T.; Hosomi, T.; Uchida, Y.; Takeda, S.; Baba, Y.; Yanagida, T. Substantial Narrowing on the Width of "Concentration Window" of Hydrothermal ZnO Nanowires via Ammonia Addition. *Sci. Rep.* **2019**, *9*, 14160.

(35) Lee, J. M.; No, Y.-S.; Kim, S.; Park, H.-G.; Park, W. I. Strong interactive growth behaviours in solution-phase synthesis of three-dimensional metal oxide nanostructures. *Nat. Commun.* **2015**, *6*, 6325.

(36) Apostoluk, A.; Parize, R.; Vilquin, B.; Nguyen, T.-H.; Consonni, V.; Appert, E.; Gaillard, F.; Masenelli, B. Room temperature optical response of zinc oxide nanowires synthesized by chemical bath deposition to toluene vapors. *Phys. Status Solidi A* **2016**, *213*, 1115-1119.

(37) Cossuet, T.; Roussel, H.; Chauveau, J.-M.; Chaix-Pluchery, O.; Thomassin, J.-L.; Appert, E.; Consonni, V. Well-ordered ZnO nanowires with controllable inclination on semipolar ZnO surfaces by chemical bath deposition. *Nanotechnology* **2018**, *29*, 475601.

(38) Verrier, C.; Appert, E.; Chaix-Pluchery, O.; Rapenne, L.; Rafhay, Q.; Kaminski-Cachopo, A.; Consonni, V. Tunable Morphology and Doping of ZnO Nanowires by Chemical Bath Deposition Using Aluminum Nitrate. *J. Phys. Chem. C* **2017**, *121*, 3573-3583.

(39) Klamuchuen, A.; Yanagida, T.; Kanai, M.; Nagashima, K.; Oka, K.; Rahong, S.; Meng, G.; Horprathum, M.; Suzuki, M.; Hidaka, Y.; Kai, S.; Kawai, T. Study on

transport pathway in oxide nanowire growth by using spacing-controlled regular array. *Appl. Phys. Lett.* **2011**, *99*, 193105.

(40) Wei, Y.; Wu, W.; Guo, R.; Yuan, D.; Das, S.; Wang, Z. L. Wafer-Scale High-Throughput Ordered Growth of Vertically Aligned ZnO Nanowire Arrays. *Nano Lett.* **2010**, *10*, 3414-3419.

(41) Wang, H.; Xie, J.; Yan, K.; Duan, M. Growth Mechanism of Different Morphologies of ZnO Crystals Prepared by Hydrothermal Method. *J. Mater. Sci. Technol.* **2011**, *27*, 153-158.

(42) Zhang, H.; Yang, D.; Li, D.; Ma, X.; Li, S.; Que, D. Controllable Growth of ZnO Microcrystals by a Capping-Molecule-Assisted Hydrothermal Process. *Cryst. Growth Des.* **2005**, *5*, 547-550.

(43) Wei, M.; Qi, Z.-M.; Ichihara, M.; Honma, I.; Zhou, H. Single-crystal ZnO nanorods fabricated with different end morphologies. *Nanotechnology* **2007**, *18*, 095608.

(44) Wang, H. Q.; Li, G. H.; Jia, L. C.; Wang, G. Z.; Li, L. General *in situ* chemical etching synthesis of ZnO nanotips array. *Appl. Phys. Lett.* **2008**, *93*, 153110.

(45) Liu, B.; Zeng, H. C. Hydrothermal Synthesis of ZnO Nanorods in the Diameter Regime of 50 nm. *J. Am. Chem. Soc.* **2003**, *125*, 4430-4431.

(46) Demes, T.; Ternon, C.; Morisot, F.; Riassetto, D.; Legallais, M.; Roussel, H.; Langlet, M. Mechanisms involved in the hydrothermal growth of ultra-thin and high aspect ratio ZnO nanowires. *Appl. Surf. Sci.* **2017**, *410*, 423-431.

4.7 Supporting Information

4.7.1 Structural characterization of the fabricated ZnO nanowires

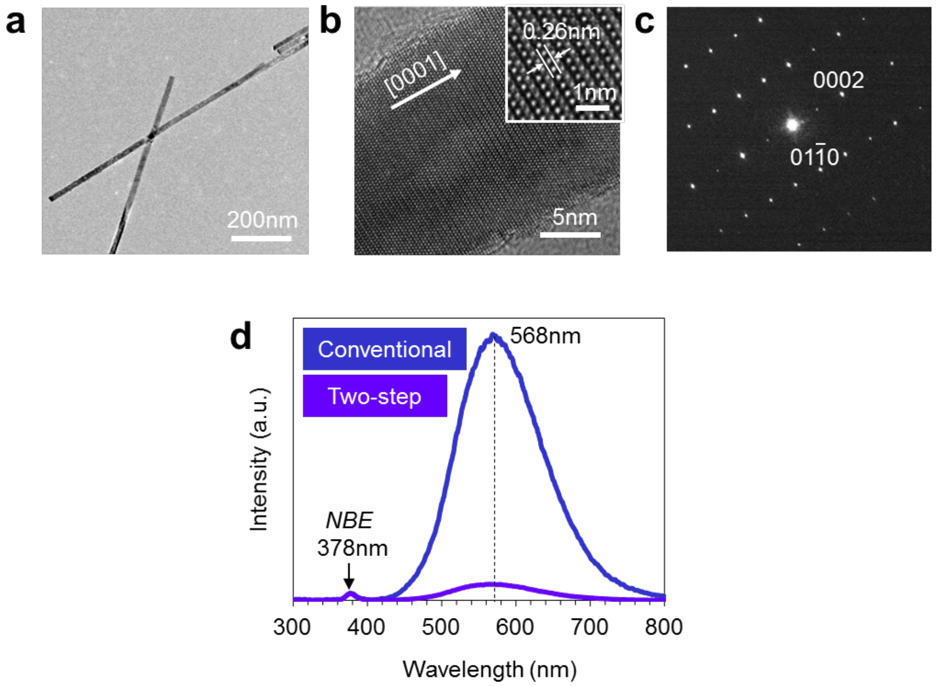

Figure S1. The characterization of the two-step grown ZnO nanowires. (a) Low magnification TEM image, (b) high magnification TEM image, and (c) selected area electron diffraction (SAED) pattern of the two-step grown ZnO nanowires. Inset of (b) shows the atomically resolved TEM image. For the two-step grown nanowires, step 1 with NH_3 50 mM, C_{Zn} 2.5 mM for 3 h, and step 2 with no NH_3, C_{Zn} 5 mM for 12 h are utilized. The TEM analysis represents that the fabricated nanowires are single crystalline with a growth direction along [0001], which is consistent with the conventional hydrothermally grown ZnO nanowires. (d) Room temperature photoluminescence spectroscopy data of two-step grown ZnO nanowires. The wavelength of excitation light is 256 nm. As a comparison, the data of single-step grown ZnO nanowires (no NH_3, C_{Zn} 25 mM for 12 h) is shown. Two peaks at 378 nm and 568 nm are observed, which are respectively corresponding to near-band edge (NBE) emission and the emission related to crystal imperfections (e.g. oxygen vacancies, Zn interstitials, surface state). The data shows that the crystal imperfections in the two-step grown nanowires are less than that of conventional ZnO nanowires. The better crystal quality of the two-step grown nanowires than the single-step grown ones might result from the suppressed nucleation on $(10\bar{1}0)$

plane. Watanabe *et al.* [1] demonstrated that more crystal imperfections are induced on $(10\bar{1}0)$ plane rather than on (0001) plane in the hydrothermal growth of ZnO nanowires. Since the single-step growth is conducted at C_{Zn} 25 mM, where it is above the critical concentration for nucleation on $(10\bar{1}0)$ plane, the plenty of crystal imperfections could be induced into the nanowires. On the contrary in the two-step grown nanowires, the nucleation on $(10\bar{1}0)$ plane is precisely suppressed by controlling C_{Zn}, leading to the better crystal quality as seen in PL spectrum.

1. Watanabe, K.; Nagata, T.; Oh, S.; Wakayama, Y.; Sekiguchi, T.; Volk, J.; Nakamura, Y. Arbitrary cross-section SEM-cathodoluminescence imaging of growth sectors and local carrier concentrations within micro-sampled semiconductor nanorods. *Nat. Commun.* **2016**, *7*, 10609.

4.7.2 Zn concentration dependence on the diameter of single step grown ZnO nanowires

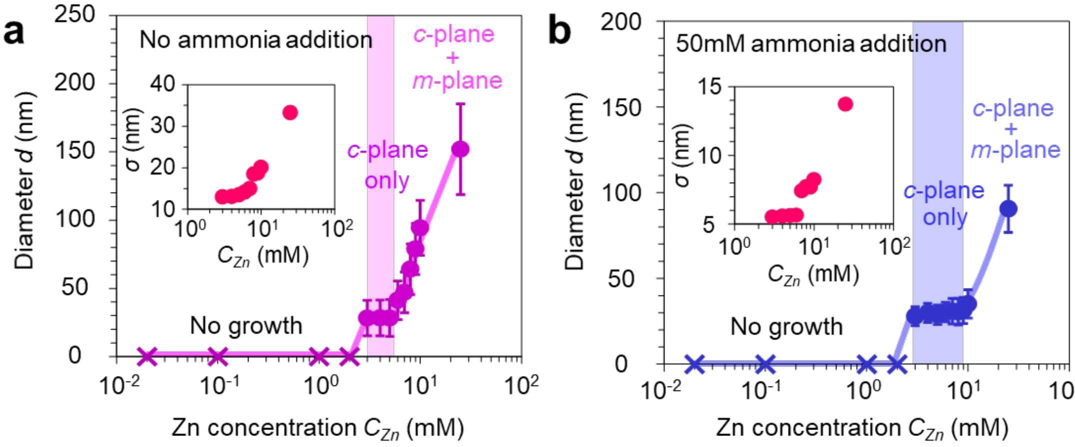

Figure S2. Zn concentration dependence on the diameter of single step grown ZnO nanowires with (a) no ammonia addition and (b) 50 mM ammonia addition. Insets show the standard deviation value of nanowire diameter. The growth time is constant to be 12 h. When increasing the Zn concentration, the nanowire growth is fist observed at above 3 mM in (a) and (b) with maintaining their diameter. Further increase of the Zn concentration above 5 mM in (a) and 9 mM in (b) leads to the increase of diameter. These two threshold concentrations correspond to the critical nucleation concentrations on (0001) plane (*c*-plane) and $(10\bar{1}0)$ plane (*m*-plane). The concentration range between these two threshold values promotes the anisotropic growth of ZnO nanowires by suppressing the sidewall growth. These threshold values are influenced by various parameters such as capping agent, surface potential at given pH condition and supersaturation degree in growth solution. As seen in the insets, the minimum diameter distributions of the nanowires are given at the condition where the sidewall growth is suppressed. However, the narrow diameter distribution of the two-step grown nanowires in figure 1 (a) cannot be achievable by solely controlling the precursor concentration in single-step growth.

Crystal plane dependent critical concentrations for a nucleation: In the nucleation theory, the nucleation phenomenon is dominated by adsorption and desorption of atoms. When increasing the precursor concentration, the adsorption rate of atoms increases. Since the nucleation in solution occurs when the size of nuclei exceeds the critical nucleation size by the sufficient precursor supply, the precursor concentration is one of the most important parameters for controlling nucleation event. For a nucleation in the presence of solid surface, an interaction between a nucleus and a solid surface should be taken into account with free energy barrier for a nucleation. The presence of solid surface significantly reduces the free energy barrier for a nucleation since an interaction between a nucleus and a solid surface is much stronger than that between a nucleus and liquid. If a surface energy (an interfacial energy in solution system) is different among crystal planes, the free energy barrier for a nucleation on each crystal plane should be different. In the ZnO crystal, (0001) polar plane has higher surface energy compared with $(10\bar{1}0)$ plane. In general, the free energy barrier for a nucleation becomes lower on a crystal plane with larger surface energy. Therefore, the critical concentration for nucleation on (0001) plane is lower than that on $(10\bar{1}0)$ plane. Although the interfacial energy in solution system differs from the surface energy, the interfacial energy on (0001) plane remains higher than that on $(10\bar{1}0)$ plane by considering the preferential crystal growth on (0001) plane in the fabricated nanowires. Based on this principle, when increasing the Zn precursor concentration, none of nanowire growth is first observed under the critical concentration on (0001) plane and then the preferential crystal growth on (0001) plane is observed in the concentration window where is above the critical concentration on (0001) plane and below that on $(10\bar{1}0)$ plane. By further increasing the Zn precursor concentration over the critical concentration on $(10\bar{1}0)$ plane, the crystal growth both on (0001) plane and $(10\bar{1}0)$ plane. Thus the Zn precursor concentration can control the competitive nucleation event on (0001) plane and $(10\bar{1}0)$ plane, which is important to design the anisotropic crystal growth of ZnO nanowires.

4.7.3 Size distribution data of the ZnO seed layer deposited onto SiO_2/Si substrate by RF sputtering

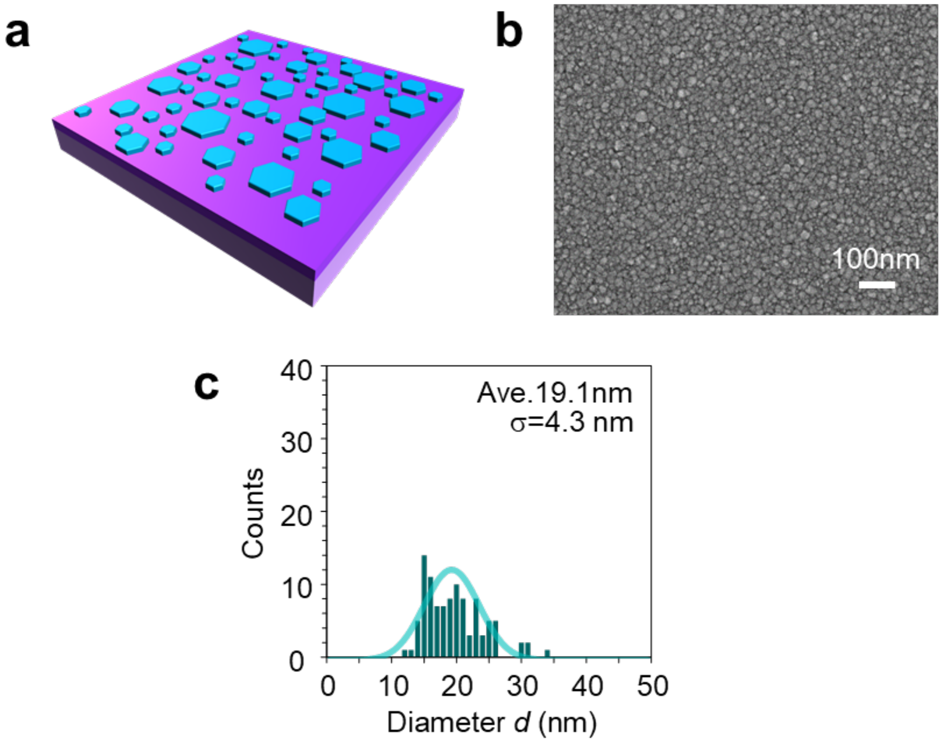

Figure S3. (a) Schematic image, (b) FESEM image and (c) size distribution data of the ZnO seed layer deposited onto SiO_2/Si substrate by RF sputtering. The thickness of seed layer is about 30 nm. In the FESEM image, the densely deposited grains are seen. The size distribution of ZnO seed layer is wider than that of two-step grown monodispersedly sized ZnO nanowires shown in figure 1 (a).

4.7.4 The growth time dependence on the morphologies of the two-step grown ZnO nanostructures/nanowires

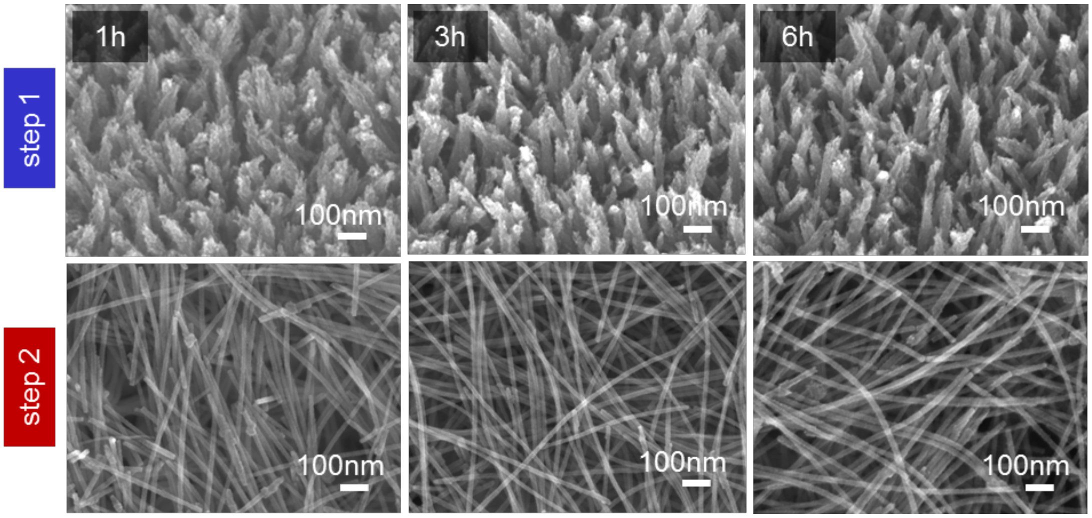

Figure S4. The growth time dependence on the morphologies of the two-step grown ZnO nanostructures/nanowires observed after step 1 (upper) and two-step growth with step 2 (lower). In this experiment, only the growth time of step 1 is varied (1 h, 3 h, 6 h) and the other conditions are kept constant (NH_3 50 mM, C_{Zn} 2.5 mM for step 1 and no NH_3, C_{Zn} 5 mM for step 2). The growth time of step 2 is 12 h.

4.7.5 The Zn concentration dependence on the morphologies of the two-step grown ZnO nanostructures/nanowires.

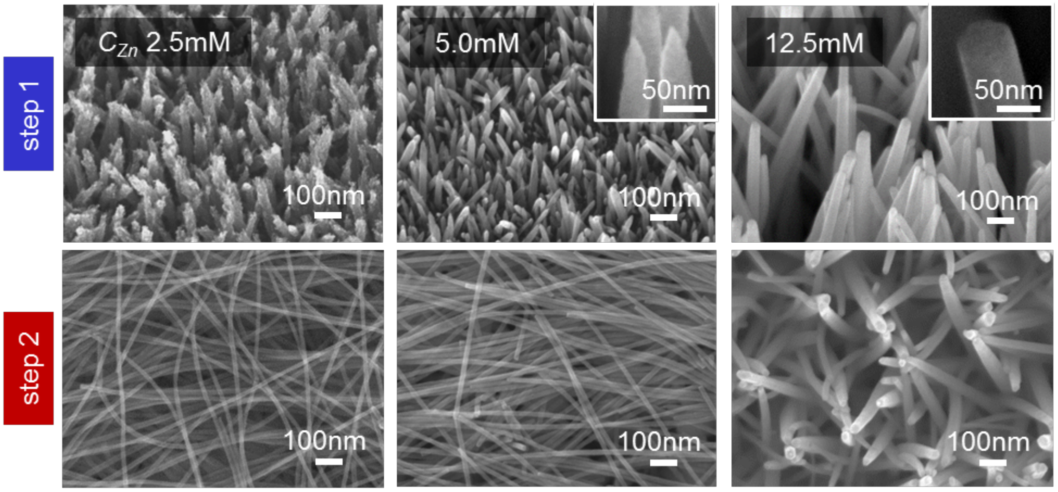

Figure S5. The Zn concentration dependence on the morphologies of the two-step grown ZnO nanostructures/nanowires observed after step 1 (upper) and two-step growth with step 2 (lower). In this experiment, only the Zn concentrations of step 1 is varied (2.5 mM, 5.0 mM, 12.5 mM) and the other conditions are kept constant (NH_3 50 mM, 3 h for step 1 and no NH_3, C_{Zn} 5 mM, 12 h for step 2). Insets show the magnified images at the tip of nanostructures/nanowires. Clearly, the secondary nanowire growth is observed only when the sharp-tips are constructed by step 1 and no longer observable from the flat-tips.

4.7.6 Simulation data of ionic species in solution for step 1 and step 2

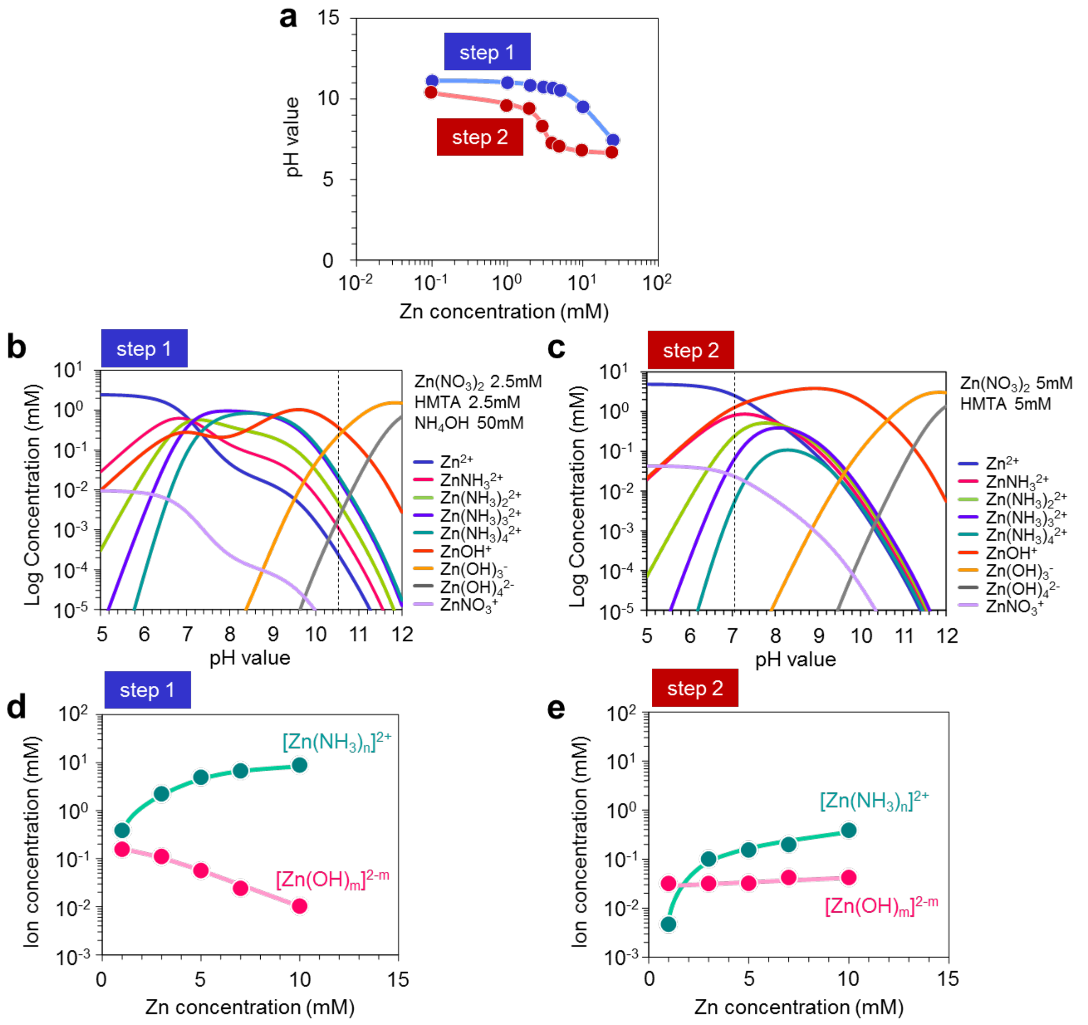

Figure S6. (a) The experimentally measured pH values of the solutions for step 1 and step 2 when varying the Zn concentration. (b,c) The calculated data of pH dependent equilibrium concentrations of ionic species existing in the growth solutions of (b) step 1 and (c) step 2. The dash lines show the experimentally measured pH values for each condition. (c,d) The Zn concentration dependence on the ion concentrations of $[Zn(NH_3)_n]^{2+}$ and $[Zn(OH)_m]^{2-m}$ species for the growth solutions of (d) step 1 and (e) step 2, respectively. The ion concentrations were calculated by using the measured pH values.

4.7.7 SEM image of the flat-top ZnO nanowires grown on Si substrate by the single-step growth

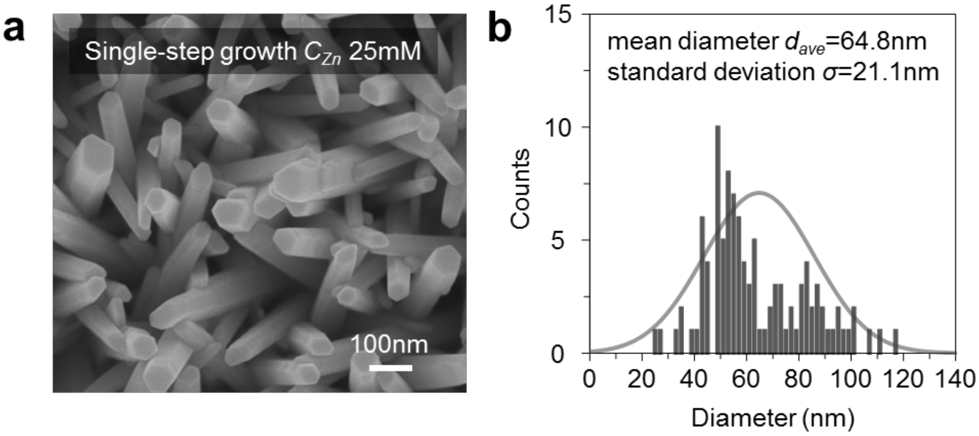

Figure S7. (a) Typical FESEM image and (b) diameter distribution data of the flat-top ZnO nanowires grown on Si substrate by the single-step growth with C_{Zn} 25 mM. In this growth, no NH_3 is added. The growth time is 12 h. The mean diameter d_{ave} and the standard deviation value σ are also shown.

4.7.8 The time-series FESEM images for NaOH-based chemical etching of the ZnO nanowires

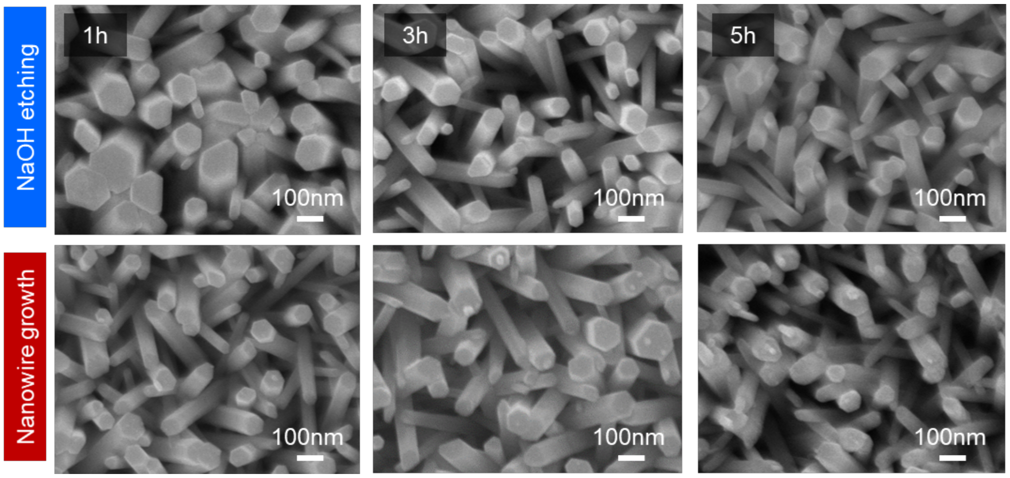

Figure S8. (a) The time-series FESEM images for NaOH-based chemical etching of the ZnO nanowires (upper) and the results of subsequent nanowire growths (lower). The pH value of NaOH solution is controlled to be 11.4, which is same condition as the ammonia-etching in figure 4 (a) and step 1 in figure 1 (c). In this experiment, the randomly sized ZnO nanowires with flat-top are first fabricated prior to the chemical etching (Figure S7) and the subsequent nanowire growth is conducted with no NH_3 and C_{Zn} 5 mM for 12 h. Contrary to the ammonia-based etching, the formations of the sharp-tip nanowires and the secondary ZnO nanowire growths are not observed in case of NaOH-based etching. This indicates that the effect of ammonia-etching observed in figure 4 (a) is due to the ammonia species rather than pH value.

4.7.9 Dependence of the diameter of the two-step grown ZnO nanowires and the standard deviation (inset) on the Zn concentration.

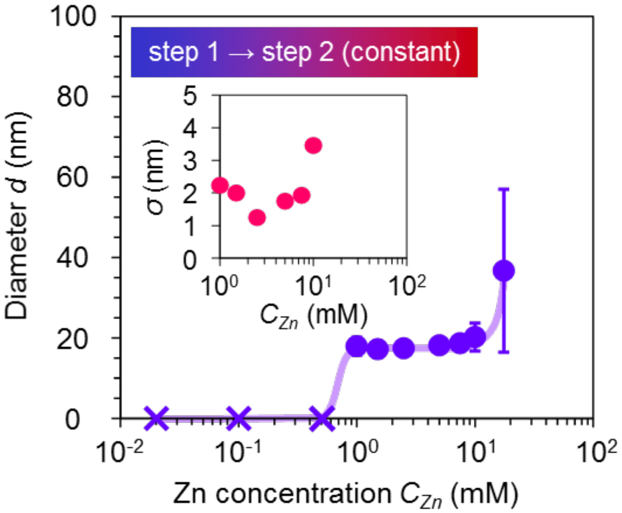

Figure S9. Dependence of the diameter of the two-step grown ZnO nanowires and the standard deviation (inset) on the Zn concentration. Only the Zn concentration in step 1 was varied, and the other conditions were kept constant (with NH_3 50 mM for step 1, no NH_3 and C_{Zn}=5 mM for step 2). The growth time for step 1 and step 2 was 3 h and 12 h, respectively. We found that the diameter and the standard deviation of the two-step grown nanowires were almost unchanged when the Zn precursor concentration C_{Zn} was varied under the critical concentration for nucleation on $(10\bar{1}0)$ plane. This is because the size of (0001) plane is not changed in this condition once the sharp-tip is formed. On the other hand, when increasing C_{Zn} above the critical concentration on $(10\bar{1}0)$ plane, the diameter increases together with the standard deviation value, implying the increase of (0001) plane size.

Discussion as to the sharp-tip formation by ammonia-etching.

Considering the difference of the growth conditions between step 1 and step 2, ammonia plausibly affects the sharp-tip formation. Here we consider how ammonia affects the ZnO formation in the growth process. In our hydrothermal process, the formation of ZnO can be explained by the following chemical reactions:

$$[\mathrm{Zn(NH_3)}_n]^{2+} + m\mathrm{OH^-} \leftrightarrow \mathrm{Zn^{2+}} + m\mathrm{OH^-} + n\mathrm{NH_3}$$

$$\leftrightarrow [\mathrm{Zn(OH)}_m]^{2-m} + n\mathrm{NH_3} \leftrightarrow \mathrm{ZnO} + \mathrm{H_2O} + (m\text{-}2)\mathrm{OH^-} + n\mathrm{NH_3},$$

where NH_3 is supplied through two routes, i.e., the ammonia addition and the decomposition of hexamethylenetetramine (HMTA). In this chemical reaction, the formation and the dissociation of ZnO simultaneously occur, and the dissociation reaction should be enhanced by adding ammonia, i.e. $[\mathrm{Zn(OH)}_m]^{2-m}$ ions and $[\mathrm{Zn(NH_3)}_n]^{2+}$ ions increase with increasing OH^- ions and NH_3 concentrations. In our experiments, the pH value and the equilibrium concentrations of $[\mathrm{Zn(OH)}_m]^{2-m}$ ions and $[\mathrm{Zn(NH_3)}_n]^{2+}$ ions become higher when ammonia is added in the growth solution (Figure S6). Since the nanowire top remains flat when the NaOH solution is employed as an etchant (Figure S8), the sharp-tip formation is caused by the ammonia species and is associated with the formation of $[\mathrm{Zn(NH_3)}_n]^{2+}$ ions rather than $[\mathrm{Zn(OH)}_m]^{2-m}$ ions. Thus, the sharp-tips are formed by an assist of dissociation reaction in the ammonia added step 1.

Now we question why the $\{10\bar{1}1\}$ planes are preferentially formed during ammonia etching. The energetically unfavourable roughened surface and high Miller index planes immediately disappear at early stage of etching process. In this regard, the lower index (0001) and $\{10\bar{1}0\}$ planes can survive during the etching. Considering the arrangement of atom in ZnO crystal, $\{10\bar{1}0\}$ planes are composed of successive Zn-aligned and O-aligned polar plane as well as (0001) plane. Since the O-aligned plane is stable and serves as a protective layer for the etchant, the $\{10\bar{1}1\}$ planes are able to remain during etching process. On the other hand, the morphology of crystal is configured by the remaining crystal planes and a plane with faster etching rate tends to be exposed when the etching proceeds. Since the ammonia etching is associated with the formation of $[Zn(NH_3)_n]^{2+}$ ions, a coordination of NH_3 to the Zn site is of critical importance for the etching. Based on the facts that the $(10\bar{1}1)$ plane possesses Zn-aligned polar plane and the number density of in-plane bond for Zn is less than (0001) plane, the etching rate on $(10\bar{1}1)$ plane must be faster than that of (0001) plane and non-polar $(10\bar{1}0)$ plane. As a consequence, the $\{10\bar{1}1\}$ planes remain and the uniformly-shaped tips facetted by the $\{10\bar{1}1\}$ planes are deterministically formed during the ammonia etching.

Chapter V

Molecularly Templated Metal Oxide Surface Discriminates Length of Aliphatic Chains with Long-Term Thermal Robustness

5.1 Abstract

Creating a thermally robust molecular selectivity on metal oxide surfaces is of immense practical utility for heterogeneous catalysts and chemical sensors. Satisfying both such thermal robustness and precise molecular selectivity within nanostructures however has been a challenging issue. Here, we demonstrate an emergence of a thermally robust molecular selectivity with one carbon resolution for aliphatic chains of aldehydes on molecularly templated single crystalline ZnO nanowire surfaces with amorphous TiOx shell layers grown by atomic layer deposition. Spectroscopic, spectrometric and microstructural measurements revealed that such molecular selectivity only emerged when controlling the number of atomic layer deposition cycles (thickness, 1.5-2.5 nm) with anchoring spatially isolated target-aliphatic aldehyde molecules on the ZnO surface during shell layer formations. Furthermore, the created molecular selectivity was found to be thermally robust, being maintained at up to 400 °C at least over 30 days under atmospheric environments. We propose a phenomenological model by numerical simulations, which explains the emerged molecular selectivity on oxide surfaces in terms of the presence of surface molecularly footprints defined by a characteristic length between the carboxyl group and the terminal methyl group. This present method to create thermally robust molecular selectivity on abundant oxide surfaces is shown to be simple and highly reproducible and holds promise for scalability and applicability to various molecules.

5.2 Introduction

Molecular recognition technology plays a crucial role in discriminating biological and chemical molecules for various applications such as disease diagnosis, health monitoring, environmental monitoring, security checking, and drug delivery.[1,2,3,4,5,6,7] For example, the selective detection of disease-related biomolecules,[8,9,10] such as viruses,[11,12] proteins[13,14] or DNAs,[15,16] in body fluids[17,18] including the blood,[19,20] saliva[21,22] and urine[23,24] provides strong evidence for the diagnosis of specific diseases, which is often used in medical diagnostics.[25,26] In recent years, as the volatile organic compounds (VOCs) in our exhaled breath are associated with diseases such as various cancers,[27,28,29] a novel diagnostic technique based on discriminating disease-related VOCs biomarkers has attracted the attention of researchers.[30,31,32] However, many similar molecules with different size, functional groups in the exhaled breath makes difficulties for selective detection of disease-related biomarkers.[33,34,35] Despite the excellent performance of gas chromatography-mass spectrometry (GC-MS) in discriminating similar molecules,[36,37] its high cost, large size, and long duration limit its practical applications in sudden illness or real-time disease monitoring.[38] Therefore, the design and development of a miniaturized portable device with excellent recognition performance for analyzing the disease-related biomarkers in exhaled gas are highly desired.[39]

Recognition elements have attracted a lot of attention as a critical component of recognition-based devices.[40,41] Many efforts have been made to develop recognition elements with higher sensitivity, higher selectivity, and better stability.[42] However, except for bioreceptors derived from body fluids and materials with properties that act selectively on target molecules, most recognition elements designed based on chemical reactions and porous structures have poor selectivity for similar molecules.[43,44] In other words, functional group modified materials can only discriminate molecules with different functional groups, while the MOF and nanocage-based materials can only discriminate molecules with different sizes.[45,46] Until now, it is completely impossible to distinguish between very similar molecules, such as those with only one carbon difference of chain length.

In this work, we successfully created a nonanal imprinted surface on the ZnO nanowires by atomic layer deposition (ALD) process, which can surprisingly discriminate the target aldehydes with only one carbon difference. By preheating the nonanal absorbed ZnO nanowires, we confirmed that isolation of the aggregated template molecules during the formation process plays a critical role in the formation of the molecular recognition surface. Furthermore, we proposed a phenomenological model by numerical simulations to interpret the emerged molecular selectivity on oxide surfaces, which describes the presence of surface molecularly footprints defined by a characteristic length between the carboxyl group and the terminal methyl group. Finally, this metal oxides-based recognition surface exhibits high thermal robustness of toleration at 400 °C for more than 720 hours. This present method creates thermally robust molecular selectivity on abundant oxide surfaces.

5.3 Experimental

Growth of ZnO Nanowires. ZnO nanowires were grown on a double-side polished Si (100) wafer (2*4 cm) substrate by hydrothermal method. First, a 1 nm Ti buffer layer and 20 nm ZnO seed layer were sequentially deposited on the substrate by radio frequency (RF) sputtering at room temperature with a power of 100 W and 50 W separately. Then immersing the seed layer-coated substrate into 200 ml growth solution upside-down containing 100 mM zinc nitrate hexahydrate ($Zn(NO_3)_2 \cdot 6H_2O$, Wako, 99.0%), 100 mM hexamethylenetetramine (HMTA, Wako, 99.0%), and 10mM branched polyethyleneimine (PEI, $M_n = 1800$, Aldrich, 50 wt.% in H_2O). The solution was kept at 95 °C for 6 h to grow the ZnO nanowires, followed by rinsing with ionized water and drying with flowing air.

Synthesis of Molecular Recognition Surface. Firstly, as-grown ZnO nanowires were annealed at 400 °C for 30 min in the air atmosphere. Secondly, immerse the thermally treated ZnO nanowire into the pure template molecule solution for 5 min at room temperature. Thirdly, put the template molecule absorbed ZnO nanowires in the ALD chamber with the flow of 5 sccm of purity N_2, and keep stable for 2 min before the ALD process, the O precursor was 18.2 MΩ cm^{-1} Millipore H_2O, the Ti precursor was Tetrakis(dimethylamido)titanium (TDMAT, $Ti(NMe_2)_4$). TiO_2 layer was deposited in cycles of TDMAT (0.1 s), purge N_2 (20 s), H_2O (0.015 s), purge N_2 (20 s) with the ALD system held at 100 °C and Ti precursor held at 75 °C. ALD cycles up to 20, 40, 60, 100, and 600 cycles were studied in this work. After the deposition of the TiO_2 shell layer, the template molecules were removed by annealing at 400 °C for 30 min, forming the molecular recognition surface with template molecule imprinting.

Characterization of Nanowires. The field emission scanning electron microscopy (SEM) and transmission microscopy (TEM) were used to characterize the morphology and ALD deposition rate.

Molecular Adsorption Process. Saturated mixture gas vapor such as hexanal, nonanal and undecanal were prepared by evaporating the liquid hexanal, nonanal, and undecanal with 2 μl separately in a brown bottle (20 ml) for 30 min at room temperature. Next, the nanowire arrays were put into the bottle and left for 5 min. The molecules adsorbed nanowires were then used for the subsequent measurement.

IR p-MAIRS Measurement. A Thermo Fisher Scientific Nicolet iS5 spectrometer equipped with a mercury-cadmium-telluride (MCT) detector was employed to measure the FT-IR spectra with the restroom purged with dry air. A series of eight single-beam sample measurements were carried out at angles of incidence from 9 to 44° at 5° steps with a resolution of 4 cm^{-1}.

GC-MS Analysis of Desorbed Gas. Mix gas adsorption was conducted by using bare ZnO nanowires, ZnO/TiO_2 nanowires with template molecule imprinting, and ZnO/TiO_2

nanowires without template molecule imprinting. The sample size was 0.2 cm*2 cm. Before adsorption, the samples were pretreated at 400 °C for 30min in an air atmosphere. Also, the saturated gas was prepared by dipping hexanal (2 µl), nonanal (2 µl), and undecanal (2 µl) liquid into a 25 ml closed brown bottle and held for 30 min in vaporing mixture gas. After that, the sample was put into the brown bottle, which was filled with saturated mixture gas for 5 min. The sample was quickly transferred into the inlet port of the GC-MS instrument (SHIMADZU GC-MS 5050A) with OPTIC-4 inlet temperature control system. The inlet procedure kept the heating temperature at 300 °C for 35 min and then dropped to 35 °C immediately. An IntertCap FFAP column was used as the capillary column, heated from 40 °C to 230 °C at a rate of 7 °C/min. The detail can be seen in Figure *S5*.

5.4 Results and Discussions

The molecular recognition surfaces for discriminating the length of aliphatic chains molecules were prepared by atomic layered deposition of ultrathin TiO_2 layers on ZnO nanowires with the assistance of molecular imprinting. Detailed fabrication conditions are shown in the *Experimental* Section. Fig.1 (a and d) shows the schematics of the selectivity of the nanowires with and without nonanal (C9) imprinted surface to hexanal (C6), nonanal (C9), and undecanal (C11) targets. The desorption amounts of each molecule on the ALD cycle-dependent ZnO/TiO_2 nanowires were measured by GC-MS, and the comparative results of amounts were shown in Fig.1 (b and d). We found that nonanal (C9) among C6, C9, and C11 targets was selectively adsorbed on the ZnO/TiO_2 nanowires with nonanal (C9) imprinting, while the nanowires without imprinting were not selectively adsorbed. The ratios of the desorbed amounts of C9 to C6 and C11 on the imprinted nanowires was as high as 18 and 8, respectively, indicating the remarkable selectivity of presented nanowires, as shown in Fig.1 (f). Furthermore, to further evaluate the recognition ability of the proposed recognition surface, we tested the selectivity towards targets of chain molecules with different functional groups and only one carbon length difference. Interestingly, these nonanal imprinted nanowires can selectively adsorb the nonanal in the mixture of molecules with different functional groups, including nonanal, 1-nonanol and nonanoic acid (Fig. *S6*) and one carbon different chain aldehydes, including hexanal (C6), octanal (C8), nonanal (C9), decanal (C10) and undecanal (C11) (Fig. *S7*). In addition, the applicability of this structure to other templates was also verified by the selective adsorption of undecanal (C11) in C6, C9, and C11 targets by C11 imprinted nanowires with 40 deposition cycles, as shown in Fig. *S8.* This selectivity of the ZnO/TiO_2 nanowires with various imprinted aldehyde templates demonstrated a deposition cycle dependence of the TiO_2 layer. Finally, we confirmed that a precise controlling of the ALD cycles when changing the template aldehydes enabled us to recognize chain aldehydes with only one carbon difference, as showed in Fig.1 (g-i). All the above results powerfully demonstrate that we have succeeded in creating an excellent molecular recognition surface, which can discriminate even one carbon different chain aldehydes.

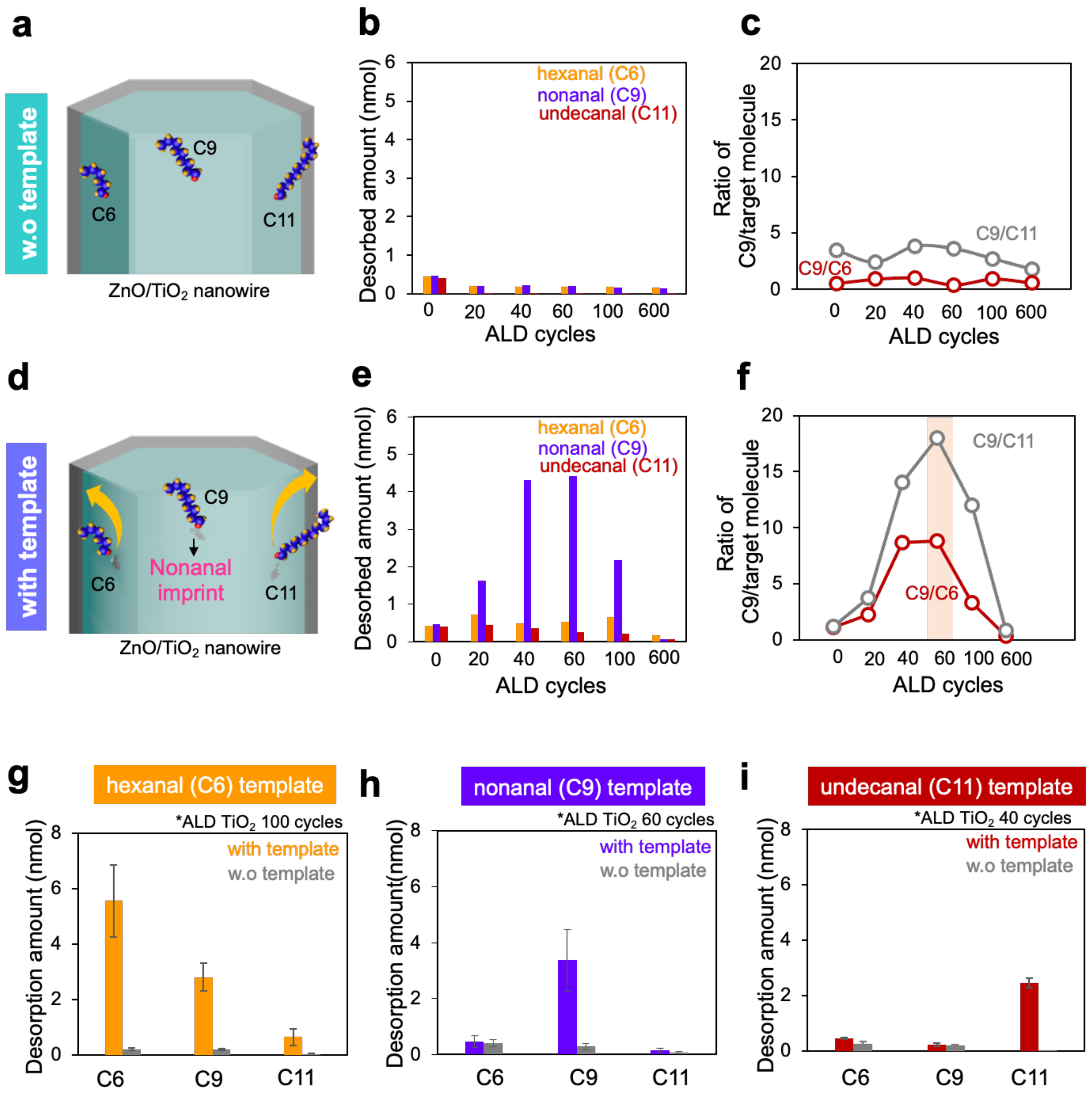

Figure 1. (a) Schematic illustration of target molecules (C6, C9, C11) adsorption on ZnO/TiO2 nanowires without nonanal imprinting, (b) Desorbed amount of target molecules (C6, C9, C11) from ZnO/TiO2 nanowires without nonanal imprinting, (c) Calculated ratio of C9/C6 and C9/C11 from ZnO/TiO2 nanowires without nonanal imprinting. (d) Schematic illustration of target molecules (C6, C9, C11) adsorption on ZnO/TiO2 nanowires with nonanal imprinting, (e) Desorbed amounts of target molecules (C6, C9, C11) from ZnO/TiO2 nanowires with nonanal imprinting, (f) Calculated ratio of C9/C6 and C9/C11 from ZnO/TiO2 nanowires with nonanal imprinting. (g)-(i) Selectivity of nanowires with and without imprinted surfaces to carbon chain length-dependent aldehydes when varying the template molecules: (g) hexanal imprinting, (h) nonanal imprinting, (i) undecanal imprinting.

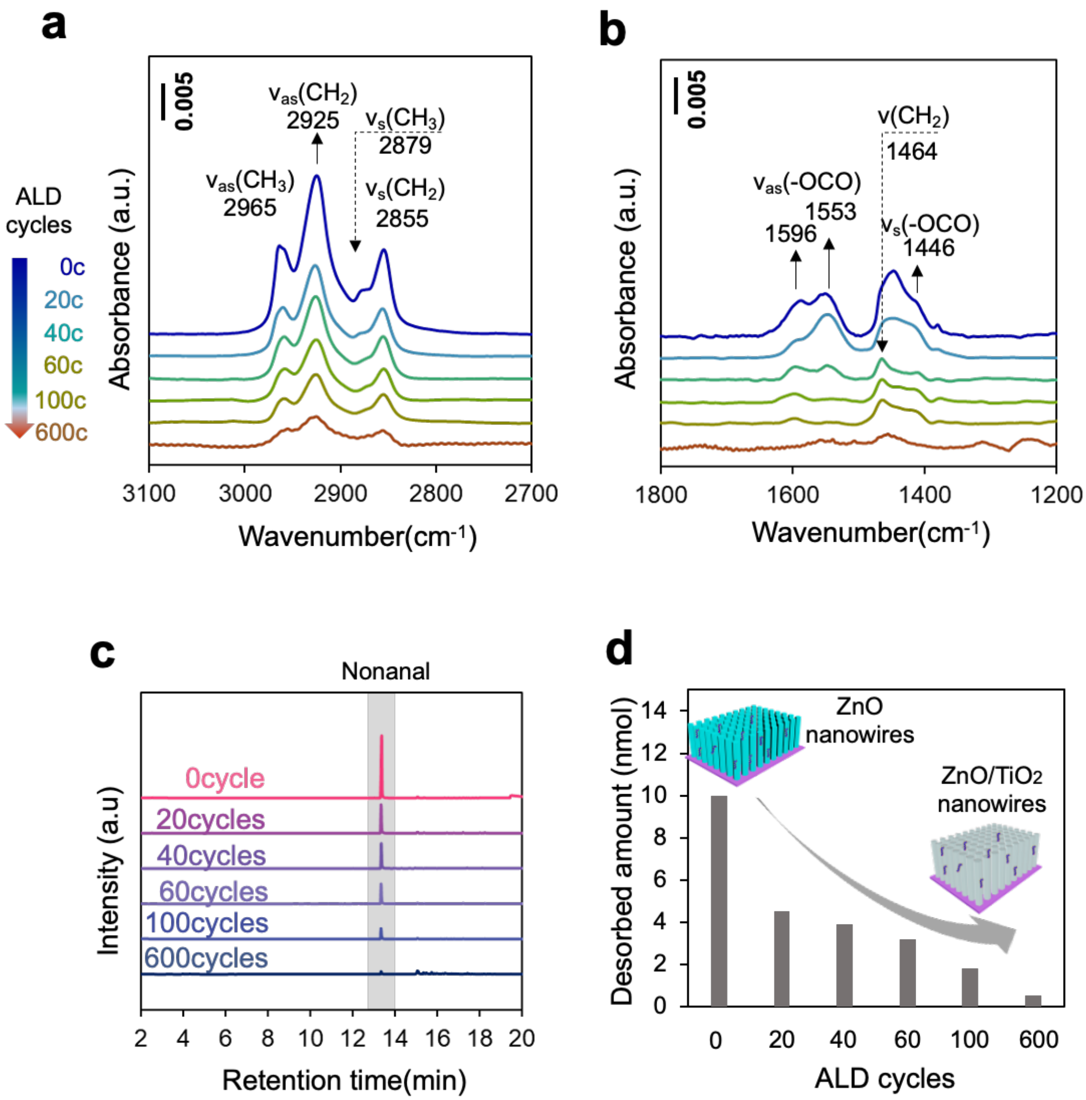

Figure 2. (a and b) FT-IR spectra of nonanal template absorbed on ZnO NWs at different TiO_2 deposition cycles. (c and d) GC-MS spectra of desorbed nonanal templates from ZnO NWs at different TiO_2 deposition cycles. Note that the 0 cycle represents the nonanal adsorbed ZnO NWs that are stabilized in the hot ALD chamber for 2 min.

To clarify the effect of templated molecules on the formation of molecularly recognized surfaces, we attempted to analyze the formation and evolution processes of imprinted surface by monitoring the status of the nonanal templates as we increased the TiO_2 deposition cycle. From the FT-IR spectra and GC-MS in Fig.2, it can be seen that both the adsorption and desorption amount of nonanal templates decrease with the increased number of ALD cycles during the TiO_2 deposition. This can be interpreted as a decrease in residual nonanal templates as the ALD cycle increases. As TiO_2 deposition cycle determines the selectivity of imprinted nanowires with various chain-length differential templates, we hypothesize that template desorption has a critical influence on the formation of imprinted surface. Furthermore, the optimized cycles (60 cycles for nonanal) to have the best selectivity is not consistent with the cycles (0 cycle for nonanal) to have the maximum amount of residual template on the surface, indicating that the selectivity of molecularly recognized surfaces is not proportional to the amount of remained template. In addition, As the chain length of the templated molecules increase from C6 to C11, the ALD cycle, which determines the thickness of the TiO_2 layer, also does not show an increasing trend, as shown in Fig. *S10*. Therefore, the cycle-dependent selectivity is also not dependent on the chain length of templated molecules.

Since the models of cycle-dependent selectivity based on the remained amount of template molecules and the size of template molecules are denied, we proposed a model based on the dispersion of aggregated templated molecules to descript the formation process of recognition surface. Fig.3 shows a schematic illustration of our model where the reduction in molecular aggregation favors the formation of an isolated nonanal imprinting during ALD process. Depending on the adsorption state of the template molecules, the formation of the recognition surface can be divided into three steps. Firstly, short preheating of the nonanal adsorbed ZnO nanowires in the hot chamber before ALD deposition allows forming a monolayer of template molecules on the nanowire surface. Testing the desorption of nonanal on nanowires at different preheating time, proved that preheating in the ALD chamber can rapidly desorb excess multilayers of nonanal and form a stable monolayer of nonanal, as shown in Fig. *S11* and Fig. *S12*. Secondly, during the deposition of the TiO_2 layer, slow desorption of the aggregated monolayer of nonanal on the nanowires leads to the formation of an isolated monolayer of nonanal. Note that desorption of monolayered nonanal is possibly caused by the interactions between precursors (TDMAT) and nonanal templates. Thirdly, after the formation of the isolated nonanal monolayer, the thickness of the TiO_2 imprinted layer becomes the dominant factor in the formation of a molecularly recognized surface with selectivity, as evidenced by the poor selectivity in the case of very thin and very thick recognition layers. This is because neither the ultra-thin layer (20 cycles) that does not close the template nor the thick layer (600 cycles) that completely covers the template is not conducive to forming an effective identification surface. Therefore, a rational model to descript the formation of the recognition surface on nanowires was proposed.

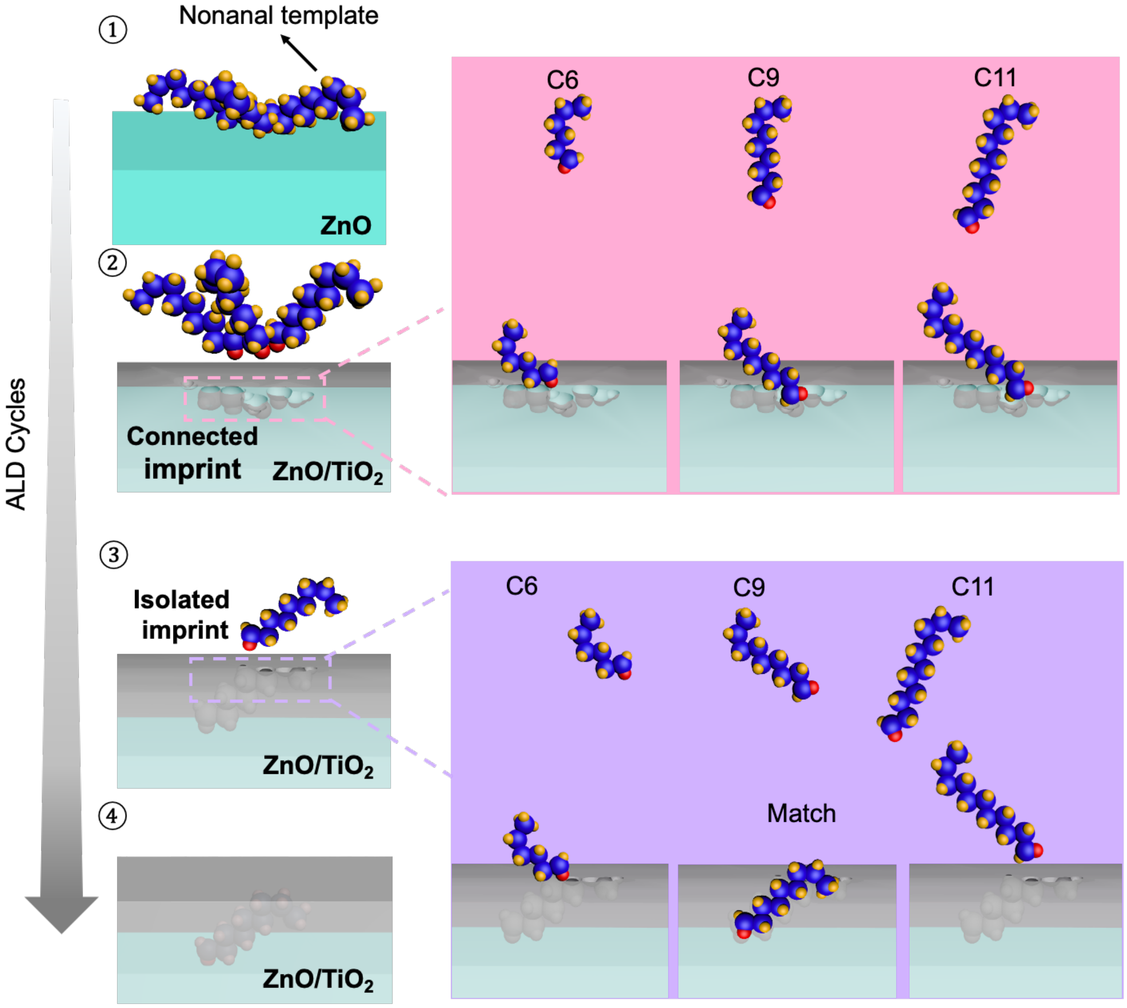

Figure 3. Schematic illustration of the dispersion of aggregated nonanal templates during ALD process.

Next, we validated the model of dispersion of aggregated templates by experimentally simulating the state of nonanal adsorbed ZnO nanowires in the pre-heating process. Fig.4 (a) shows the FT-IR spectra of nonanal template adsorbed ZnO nanowires as the pre-heating temperature is increased from 100 °C to 200 °C. As expected, the template molecules reduced as the pre-heating temperature increased, as shown in Fig.4 (b). Furthermore, Fig.4 (c) shows that C9 imprinted nanowires with only 20 cycles TiO_2 deposition can selectively adsorbed C9 targets in C6, C9 and C11 when the pre-heating temperature was increased from 150 °C to 175 °C. The extracted ratios of C9/C6 and C9/C11 in Fig.4 (d) provide a clearer view of the improved selectivity. Furthermore, by pre-treating nanowires at 175 °C, the optimal deposition cycle of TiO_2 on the molecularly recognized surface became 40 cycles, which is lower than the 60 cycles of 150 ^{o}C heating treatment, as shown in Fig.1 (e). We believe that this is because it is easier to obtain isolated nonanal templates on nanowires by desorption of aggregated templates at higher temperature. Thus, these results reveal that the dispersion of aggregation templates plays a critical role in forming molecularly recognized surfaces.

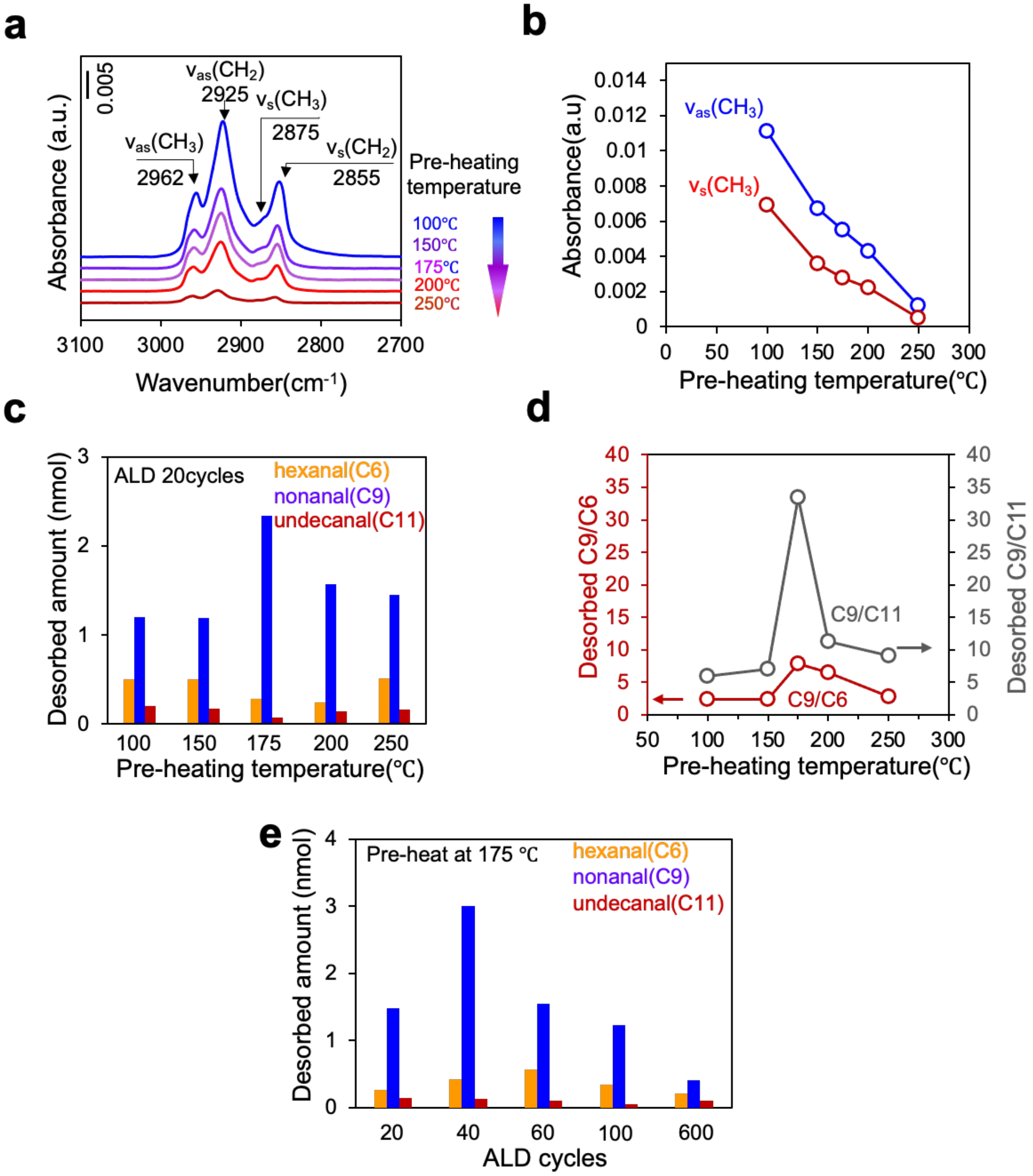

Figure 4. (a) FTIR spectra of nonanal templates adsorbed ZnO nanowires at different pre-heating temperatures from 100 °C to 200 °C, (b) Intensity of -CH_3 group at different pre-heating temperature. (c) Desorption of target molecules from ZnO/TiO_2 nanowires with nonanal imprinting (TiO_2 layer with 20 cycles) at different pre-heating temperatures, (d) Calculated ratios of desorbed C9 to desorbed C6 and C11. (e) The cycle-dependent selectivity of the recognition surface of nonanal imprinted ZnO/TiO_2 nanowires when preheated at 175 °C.

We then discussed why the surface of the imprinted nanowires was selective for the target molecules. As shown in Fig *S6*, the selectivity of recognition surface towards targets with different functional groups indicates that the functional group plays a critical role in target molecule recognition. However, since the target molecules of C6, C9 and C11 are terminated with the same functional group, we assume that the H-O-Ti interaction between molecule and surface affects selectivity. And we tried to demonstrate the effect of H-O-Ti interaction on selectivity by replacing the target molecules from H-nonanal to D-nonanal. As shown in Fig.5 (a), for the H-nonanal imprinted ZnO/TiO_2 nanowires, the desorbed H-nonanal was higher than the desorbed D-nonanal, while the ZnO/TiO_2 nanowires without imprinting showed the opposite trend. This implies the importance of the alkyl chain for molecular selectivity. According to the entropy effect, when the active aldehyde group on nonanal binds to the nanowire surface, the terminal alkyl group at the opposite side exhibits a dynamically rotatable gauche structure. In this case, with the rotation of gauche structural alkyl terminal during the nonanal imprinting process, we envisage that the shape of the molecular imprinting may be dumbbell-shaped, as shown in Fig.6 (b). To validate this assumption, molecular dynamics calculations using AMBER were used to simulate the structures of the molecules and the formation of the imprinted structure (Fig. *S17*). The results clearly show that the carboxyl group firmly adsorbed in the (100) plane of ZnO nanowires, while the alkyl-terminal part is dynamic gauche structure. Fig.6 (d) shows gauche form ratio of C6, C9 and C11 at different C-C bond positions. The results show that the shorter the carbon chain, the higher the proportion of gauche structure at the C-C bond away from the carboxyl group. Therefore, the imprinted structure formed by the long carbon chains is too narrow to prevent the entry of molecules from the short carbon chains. This explains why even the shorter length of the C6 chain cannot enter the imprinted structure of C9. Moreover, we have also experimentally verified assumption by recognizing the target molecules with the same chain length, as shown in Fig.5 (e). We found that the imprinted nanowires can’t discriminate the corresponding nonanal and 8,8-dimethynonanal which have the same chain length, regardless of which template was used for imprinting. All the above results confirmed our model based on the gauche structure of the adsorbed molecules.

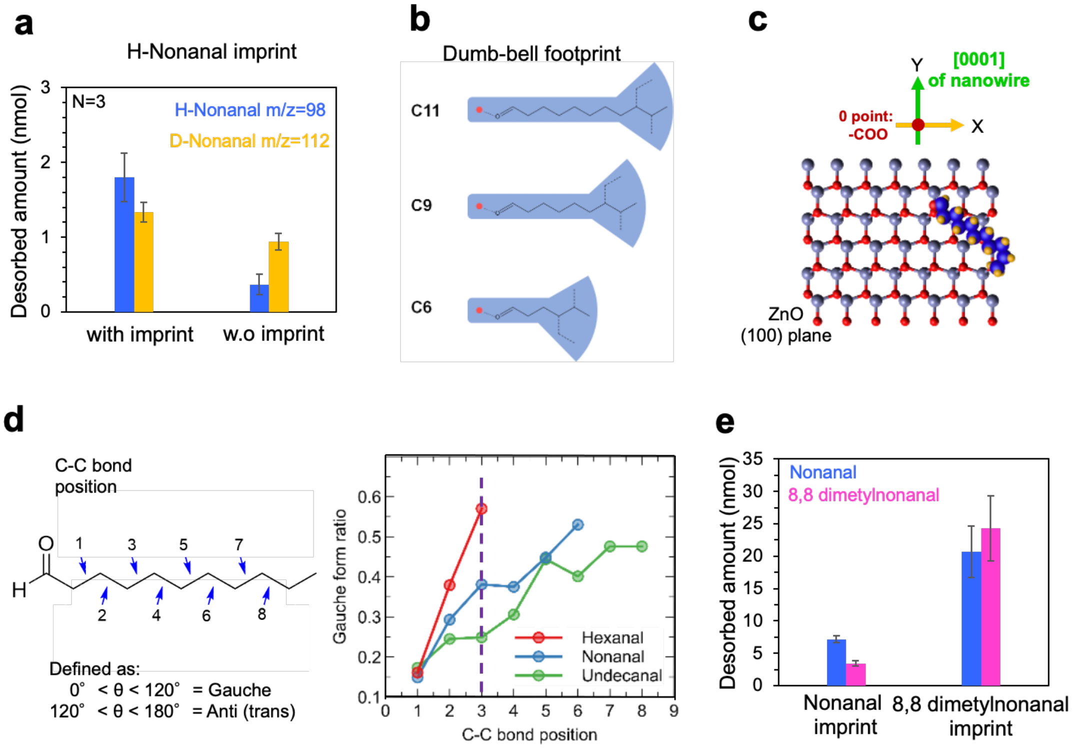

Figure 5. (a) Desorbed H-nonanal and D-nonanal on ZnO/TiO$_2$ nanowires surface with H-nonanal imprinting from a mixture gas of H-nonanal and D-nonanal. (b) Model of conformations of different template molecules (C6, C9, C11). (c) Schematic illustration of nonanal templates adsorbed on (100) plane of ZnO nanowires. (d) Calculated result of the conformations of different templated molecules. (e) Desorbed nonanal and 8,8-dimethynonanal from nonanal and 8,8-dimethynonanal imprinted ZnO/TiO$_2$ nanowires.

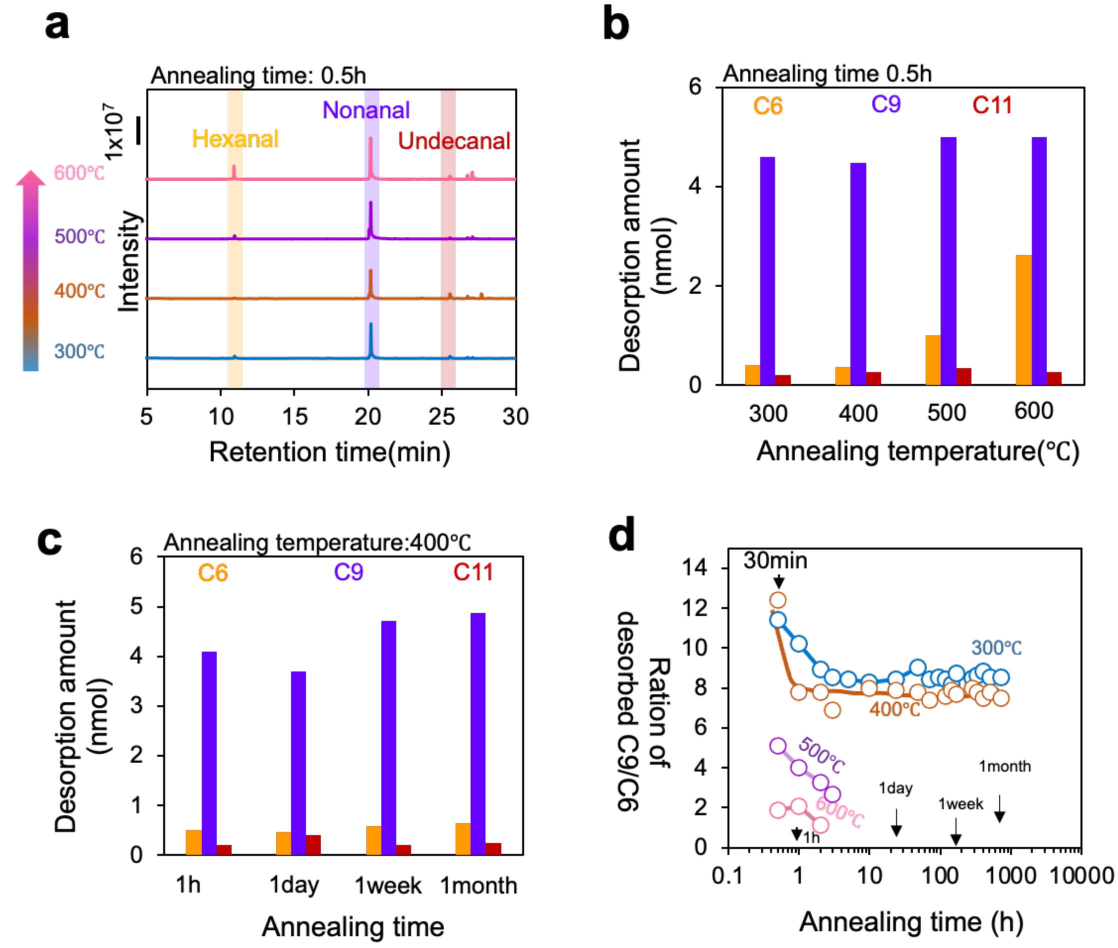

Figure 6. (a) GC-MS spectra for desorbed C6, C9 and C11 on ZnO/TiO$_2$ nanowires with nonanal imprinting at different annealing temperature, (b) Extracted desorption amount of C6, C9 and C11 on ZnO/TiO$_2$ nanowires surface with nonanal imprinting. (c) Long-term stability of the ZnO/TiO$_2$ nanowires surfaces with nonanal imprinting. (d) Time series data of selectivity performance expressed in terms of the ratio of desorbed C9/C6 when varying the annealing temperature.

Finally, we examined the thermal stability of the presented molecular recognition surfaces. Fig.6 (a) shows GC-MS spectra for desorbed C6, C9, and C11 on ZnO/TiO$_2$ nanowires surface with nonanal imprinting at the different annealing temperatures. Fig.6 (b) shows the desorption amount of C6, C9, and C11 on ZnO/TiO$_2$ nanowires surface with nonanal imprinting, an extract from Fig.6 (a). The thermal stability can be maintained up to an annealing temperature of 400 ℃, which is robust enough for future electrical sensing. Fig.6 (c) shows the long-term stability of the ZnO/TiO_2 nanowires surface with nonanal imprinting. Fig.6 (d) shows time series data of selectivity performance expressed in terms of the ratio of desorbed C9/C6 when varying the annealing temperature. The thermal robust of the molecular recognition surface can be maintained at up to 400 °C for more than 720 hours. This method creates a thermally stable molecular recognition surface on the metal oxide surface, and we believe this recognition surface can be applied to various portable devices.

5.5 Conclusion

In summary, we created a nonanal imprinted surface on the ZnO nanowires by atomic layer deposition (ALD) process, which can discriminate the target aldehydes with only one carbon difference. Isolation of the aggregated template molecules during the formation process plays an important role in formation of the molecular recognition surface and has been experimentally verified by pre-heating nonanal absorbed ZnO nanowires. A combination of numerical simulation and experiments based on the selectivity of target molecules with different chain lengths interpret the emerged molecular selectivity on the oxide surface. Furthermore, we confirm the thermal stability of the recognition surface, which can be maintained up to 400 °C for more than 720 hours. The current strategy provides a potential method to create thermally robust molecular selectivity based portable devices for developing a novel exhaled gas-based disease diagnostic instrument.

5.6 References

(1) Budhathoki-Uprety, J.; Shah, J.; Korsen, J. A.; Wayne, A. E.; Galassi, T. V.; Cohen, J. R.; Harvey, J. D.; Jena, P. V.; Ramanathan, L. V.; Jaimes, E. A.; Heller, D. A. Synthetic Molecular Recognition Nanosensor Paint for Microalbuminuria. *Nat. Commun.* **2019**, *10* (1), 3605.

(2) Tian, H.; Fan, H.; Li, M.; Ma, L. Zeolitic Imidazolate Framework Coated ZnO Nanorods as Molecular Sieving to Improve Selectivity of Formaldehyde Gas Sensor. *ACS Sensors* **2016**, *1* (3), 243–250.

(3) Habibi, N.; Kamaly, N.; Memic, A.; Shafiee, H. Self-Assembled Peptide-Based Nanostructures: Smart Nanomaterials toward Targeted Drug Delivery. *Nano Today* **2016**, *11* (1), 41–60.

(4) Sarfo, D. K.; Izake, E. L.; O'Mullane, A. P.; Ayoko, G. A. Molecular Recognition and Detection of Pb (II) Ions in Water by Aminobenzo-18-Crown-6 Immobilised onto a Nanostructured SERS Substrate. *Sens. Actuators B Chem.* **2018**, *255*, 1945–1952.

(5) Khan, S.; Le Calvé, S.; Newport, D. A Review of Optical Interferometry Techniques for VOC Detection. *Sens. Actuator A Phys.* **2020**, *302*.

(6) Moon, H. G.; Jung, Y.; Han, S. D.; Shim, Y. S.; Shin, B.; Lee, T.; Kim, J. S.; Lee, S.; Jun, S. C.; Park, H. H.; Kim, C.; Kang, C. Y. Chemiresistive Electronic Nose toward Detection of Biomarkers in Exhaled Breath. *ACS Appl. Mater. Interfaces* **2016**, *8* (32), 20969–20976.

(7) Liu, J.; Liu, W.; Zhang, K.; Shi, J.; Zhang, Z. A Magnetic Drug Delivery System with "OFF–ON" State via Specific Molecular Recognition and Conformational Changes for Precise Tumor Therapy. *Adv. Healthc. Mater.* **2020**, *9* (3), 1901316.

(8) Pluta, R.; Ułamek-Kozioł, M.; Januszewski, S.; Czuczwar, S. J. Exosomes as Possible Spread Factor and Potential Biomarkers in Alzheimer's Disease: Current Concepts. *Biomark. Med.* **2018**, *12* (9), 1025–1033.

(9) Han, Y.; Chen, T.; Li, Y.; Chen, L.; Wei, L.; Xiao, L. Single-Particle Enumeration-Based Sensitive Glutathione S-Transferase Assay with Fluorescent Conjugated Polymer Nanoparticle. *Anal. Chem.* **2019**, *91* (17), 11146–11153.

(10) Zhang, P.; Cui, Y.; Anderson, C. F.; Zhang, C.; Li, Y.; Wang, R.; Cui, H. Peptide-Based Nanoprobes for Molecular Imaging and Disease Diagnostics. *Chem. Soc. Rev.*

2018, *47* (10), 3490–3529.

(11) Liu, W.; Li, H.; Sheng, H.; Liu, X.; Chi, P.; Wang, X.; Mao, M. A Randomized Controlled Trial on Evaluation of Plasma Epstein-Barr Virus Biomarker for Early Diagnosis in Patients With Nasopharyngeal Carcinoma. *Adv. Ther.* **2020**, *37* (10), 4280–4290.

(12) Balcioglu, M.; Rana, M.; Hizir, M. S.; Robertson, N. M.; Haque, K.; Yigit, M. V. Rapid Visual Screening and Programmable Subtype Classification of Ebola Virus Biomarkers. *Adv. Healthc. Mater.* **2017**, *6* (2), 1600739.

(13) Cohen, J. D.; Javed, A. A.; Thoburn, C.; Wong, F.; Tie, J.; Gibbs, P.; Schmidt, C. M.; Yip-Schneider, M. T.; Allen, P. J.; Schattner, M.; Brand, R. E.; Singhi, A. D.; Petersen, G. M.; Hong, S.-M.; Kim, S. C.; Falconi, M.; Doglioni, C.; Weiss, M. J.; Ahuja, N.; He, J.; Makary, M. A.; Maitra, A.; Hanash, S. M.; Dal Molin, M.; Wang, Y.; Li, L.; Ptak, J.; Dobbyn, L.; Schaefer, J.; Silliman, N.; Popoli, M.; Goggins, M. G.; Hruban, R. H.; Wolfgang, C. L.; Klein, A. P.; Tomasetti, C.; Papadopoulos, N.; Kinzler, K. W.; Vogelstein, B.; Lennon, A. M. Combined Circulating Tumor DNA and Protein Biomarker-Based Liquid Biopsy for the Earlier Detection of Pancreatic Cancers. *Proc. Natl. Acad. Sci.* **2017**, *114* (38), 10202–10207.

(14) Fu, Y.; Wang, N.; Yang, A.; Law, H. K.; Li, L.; Yan, F. Highly Sensitive Detection of Protein Biomarkers with Organic Electrochemical Transistors. *Adv. Mater.* **2017**, *29* (41), 1703787.

(15) Ziegler, A.; Koch, A.; Krockenberger, K.; Großhennig, A. Personalized Medicine Using DNA Biomarkers: A Review. *Human Genetics* **2012**, *131* (10), 1627–1638.

(16) Constâncio, V.; Nunes, S. P.; Henrique, R.; Jerónimo, C. DNA Methylation-Based Testing in Liquid Biopsies as Detection and Prognostic Biomarkers for the Four Major Cancer Types. *Cells* **2020**, *9* (3), 624.

(17) Senf, B.; Yeo, W. H.; Kim, J. H. Recent Advances in Portable Biosensors for Biomarker Detection in Body Fluids. *Biosensors* **2020**, *10* (9), 127.

(18) Silva, S. S.; Lopes, C.; Teixeira, A. L.; Sousa, M. C. De; Medeiros, R. Forensic MiRNA: Potential Biomarker for Body Fluids? *Forensic Sci. Int. Genet.* **2015**, *14*, 1–10.

(19) Altuna-Azkargorta, M.; Mendioroz-Iriarte, M. Blood Biomarkers in Alzheimer's Disease. *Neurologia* **2018**, doi.org/10.1016/j.nrleng.2018.03.006

(20) Parnetti, L.; Gaetani, L.; Eusebi, P.; Paciotti, S.; Hansson, O.; El-Agnaf, O.; Mollenhauer, B.; Blennow, K.; Calabresi, P. CSF and Blood Biomarkers for Parkinson's Disease. *Lancet Neurol.* **2019**, *18* (6), 573–586.

(21) Arias-Bujanda, N.; Regueira-Iglesias, A.; Balsa-Castro, C.; Nibali, L.; Donos, N.; Tomás, I. Accuracy of Single Molecular Biomarkers in Saliva for the Diagnosis of Periodontitis: A Systematic Review and Meta-Analysis. *J. Clin. Periodontol*. **2020**, *47* (1), 2-18.

(22) Gleerup, H. S.; Hasselbalch, S. G.; Simonsen, A. H. Biomarkers for Alzheimer's Disease in Saliva: A Systematic Review. *Dis. Markers* **2019**, *2019*, 1–11.

(23) Yokota, K.; Uchida, H.; Sakairi, M.; Abe, M.; Tanaka, Y.; Tainaka, T.; Shirota, C.; Sumida, W.; Oshima, K.; Makita, S.; Amano, H.; Hinoki, A. Identification of Novel Neuroblastoma Biomarkers in Urine Samples. *Sci. Rep.* **2021**, *11* (1), 1–9.

(24) Xu, M. Y.; Sun, Y. J.; Wang, P.; Yang, L.; Wu, Y. J. Metabolomic Biomarkers in Urine of Rats Following Long-Term Low-Dose Exposure of Cadmium and/or Chlorpyrifos. *Ecotoxicol. Environ. Saf.* **2020**, *195*, 110467.

(25) Mascini, M.; Tombelli, S. Biosensors for Biomarkers in Medical Diagnostics. *Biomarkers*. **2008**, *13* (7-8), 637–657.

(26) Guk, K.; Han, G.; Lim, J.; Jeong, K.; Kang, T.; Lim, E. K.; Jung, J. Evolution of Wearable Devices with Real-Time Disease Monitoring for Personalized Healthcare. *Nanomaterials*. **2019**, *9* (6), 813.

(27) Zuo, W.; Bai, W.; Gan, X.; Xu, F.; Wen, G.; Zhang, W. Detection of Lung Cancer by Analysis of Exhaled Gas Utilizing Extractive Electrospray Ionization-Mass Spectroscopy. *J. Biomed. Nanotechnol.* **2019**, *15* (4), 633-646.

(28) Sakumura, Y.; Koyama, Y.; Tokutake, H.; Hida, T.; Sato, K.; Itoh, T.; Akamatsu, T.; Shin, W. Diagnosis by Volatile Organic Compounds in Exhaled Breath from Lung Cancer Patients Using Support Vector Machine Algorithm. *Sensors* **2017**, *17* (2), 287.

(29) Smolinska, A.; Klaassen, E. M. M.; Dallinga, J. W.; van de Kant, K. D. G.; Jobsis, Q.; Moonen, E. J. C.; van Schayck, O. C. P.; Dompeling, E.; van Schooten, F. J. Profiling of Volatile Organic Compounds in Exhaled Breath As a Strategy to Find Early Predictive Signatures of Asthma in Children. *Plos One* **2014**, *9* (4), e95668.

(30) Selvaraj, R.; Vasa, N. J.; Nagendra, S. M. S.; Mizaikoff, B. Advances in Mid-Infrared Spectroscopy-Based Sensing Techniques for Exhaled Breath Diagnostics. *Molecules*

2020, *25* (9), 2227.

(31) Krilaviciute, A.; Leja, M.; Kopp-Schneider, A.; Barash, O.; Khatib, S.; Amal, H.; Broza, Y. Y.; Polaka, I.; Parshutin, S.; Rudule, A.; Haick, H.; Brenner, H. Associations of Diet and Lifestyle Factors with Common Volatile Organic Compounds in Exhaled Breath of Average-Risk Individuals. *J. Breath Res.* **2019**, *13* (2), 026006.

(32) Broza, Y. Y.; Har-Shai, L.; Jeries, R.; Cancilla, J. C.; Glass-Marmor, L.; Lejbkowicz, I.; Torrecilla, J. S.; Yao, X.; Feng, X.; Narita, A.; Müllen, K.; Miller, A.; Haick, H. Exhaled Breath Markers for Nonimaging and Noninvasive Measures for Detection of Multiple Sclerosis. *ACS Chem. Neurosci.* **2017**, *8* (11), 2402-2413.

(33) Rezk-Hanna, M.; Mosenifar, Z.; Benowitz, N. L.; Rader, F.; Rashid, M.; Davoren, K.; Moy, N. B.; Doering, L.; Robbins, W.; Sarna, L.; Li, N.; Chang, L. C.; Elashoff, R. M.; Victor, R. G. High Carbon Monoxide Levels from Charcoal Combustion Mask Acute Endothelial Dysfunction Induced by Hookah (Waterpipe) Smoking in Young Adults. *Circulation* **2019**, *139* (19), 2215-2224.

(34) Chang, Y.; Tang, N.; Qu, H.; Liu, J.; Zhang, D.; Zhang, H.; Pang, W.; Duan, X. Detection of Volatile Organic Compounds by Self-Assembled Monolayer Coated Sensor Array with Concentration-Independent Fingerprints. *Sci. Rep.* **2016**, *6* (1), 23970.

(35) Kusuma, V. A.; Freeman, B. D.; Borns, M. A.; Kalika, D. S. Influence of Chemical Structure of Short Chain Pendant Groups on Gas Transport Properties of Cross-Linked Poly (Ethylene Oxide) Copolymers. *J. Memb. Sci.* **2009**, *327* (1-2), 195-207.

(36) Moufid, M.; Hofmann, M.; El Bari, N.; Tiebe, C.; Bartholmai, M.; Bouchikhi, B. Wastewater Monitoring by Means of E-Nose, VE-Tongue, TD-GC-MS, and SPME-GC-MS. *Talanta* **2021**, *221*, 121450.

(37) Capone, S.; Tufariello, M.; Francioso, L.; Montagna, G.; Casino, F.; Leone, A.; Siciliano, P. Aroma Analysis by GC/MS and Electronic Nose Dedicated to Negroamaro and Primitivo Typical Italian Apulian Wines. *Sens. Actuators B Chem.* **2013**, *179*, 259–269.

(38) Luo, Z.; Ang, M. J. Y.; Chan, S. Y.; Yi, Z.; Goh, Y. Y.; Yan, S.; Tao, J.; Liu, K.; Li, X.; Zhang, H.; Huang, W.; Liu, X. Combating the Coronavirus Pandemic: Early Detection, Medical Treatment, and a Concerted Effort by the Global Community.

Research **2020**, *2020*, 1–35.

(39) Petruci, J. F. D. S.; Cardoso, A. A. Portable and Disposable Paper-Based Fluorescent Sensor for in Situ Gaseous Hydrogen Sulfide Determination in Near Real-Time. *Anal. Chem.* **2016**, *88* (23), 11714–11719.

(40) Lee, J.-O.; So, H.-M.; Jeon, E.-K.; Chang, H.; Won, K.; Kim, Y. H. Aptamers as Molecular Recognition Elements for Electrical Nanobiosensors. *Anal. Bioanal. Chem.* **2008**, *390* (4), 1023–1032.

(41) Muzzi, C.; Fuoco, A.; Monteleone, M.; Esposito, E.; Jansen, J. C.; Tocci, E. Optical Analysis of the Internal Void Structure in Polymer Membranes for Gas Separation. *Membranes (Basel).* **2020**, *10* (11), 328.

(42) Thaler, M.; Luppa, P. B. Highly Sensitive Immunodiagnostics at the Point of Care Employing Alternative Recognition Elements and Smartphones: Hype, Trend, or Revolution? *Anal. Bioanal. Chem.* **2019**, *411* (29), 7623–7635.

(43) Peltomaa, R.; Benito-Peña, E.; Barderas, R.; Moreno-Bondi, M. C. Phage Display in the Quest for New Selective Recognition Elements for Biosensors. *ACS Omega* **2019**, *4* (7), 11569–11580.

(44) Zhao, M.; Wang, J.; Yu, H.; He, Y.; Duan, T. A Highly Selective and Sensitive Colorimetric Assay for Specific Recognition Element-Free Detection of Uranyl Ion. *Sens. Actuators B Chem.* **2020**, *307*, 127664.

(45) Wu, Y.; Liu, J.; Huang, W.; He, Z.; Zhou, J.; Li, Y. Recognition Mechanism of Molecularly Imprinted Polymers by Aggregation-Induced Emission. *J. Mater. Chem. C* **2020**, *8* (39), 13574–13581.

(46) Mandal, T. N.; Karmakar, A.; Sharma, S.; Ghosh, S. K. Metal-Organic Frameworks (MOFs) as Functional Supramolecular Architectures for Anion Recognition and Sensing. *Chem. Rec.* **2018**, *18* (2), 154–164.

5.7 Supporting Information

5.7.1 Experiment procedure

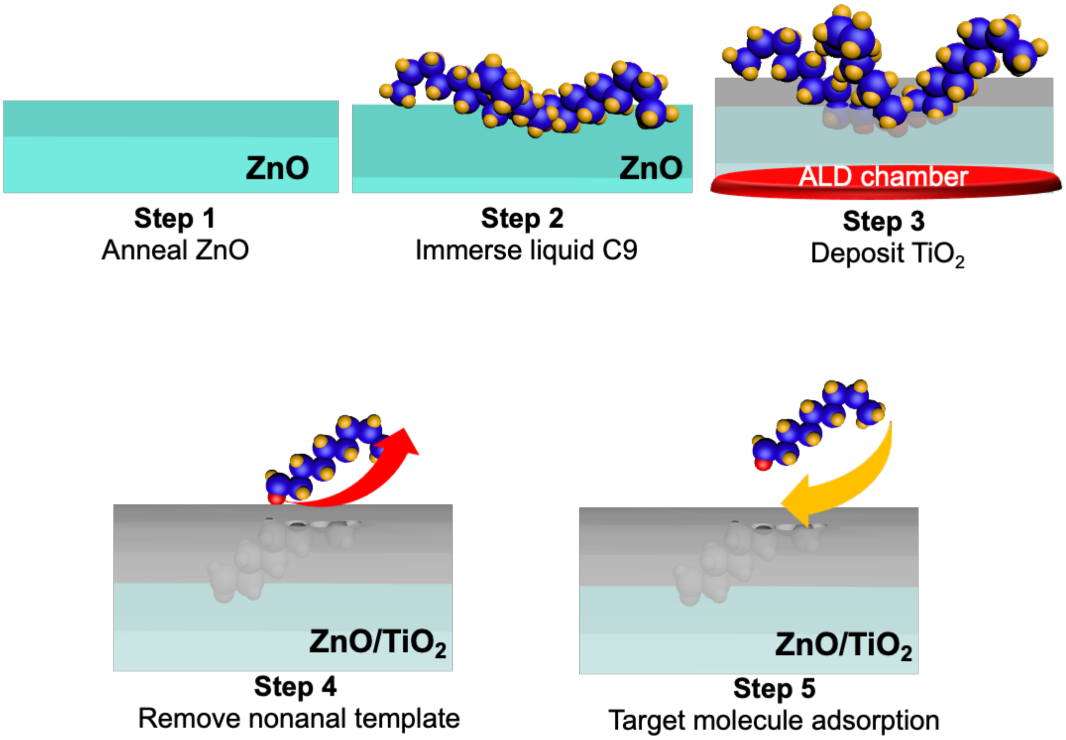

Figure S1. Schematic of the fabrication process of molecular recognition surface

5.7.2 SEM images of ZnO/TiO_2 nanowires with nonanal template at different TiO_2 deposition cycles

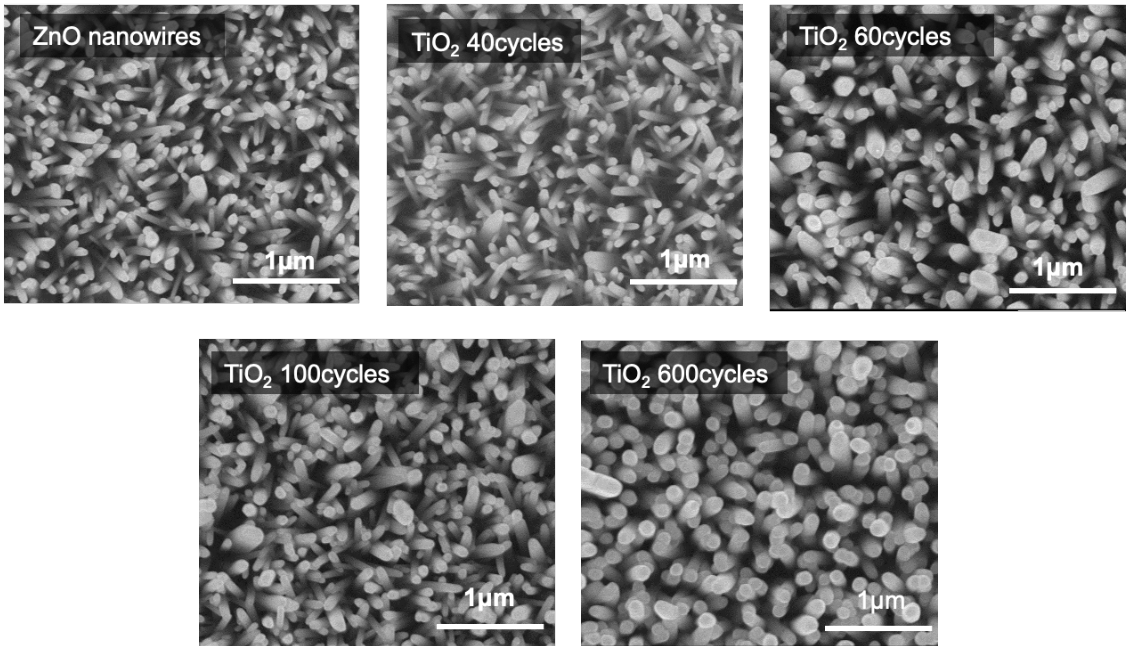

Figure S2. SEM image of various TiO_2 cycles deposited ZnO nanowires array (with nonanal template absorbed on ZnO nanowires).

5.7.3 STEM for calculation the deposition rate of TiO_2

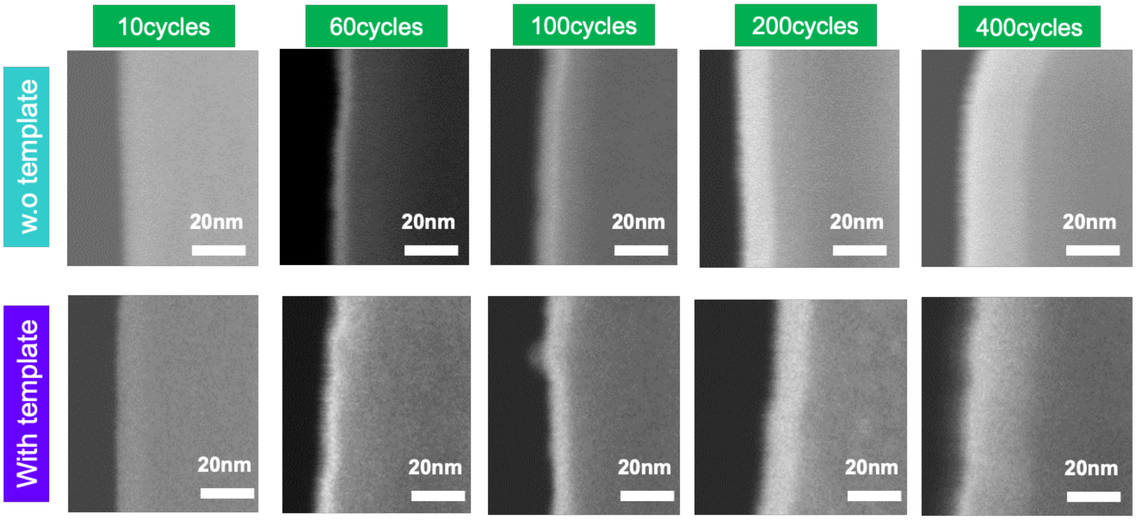

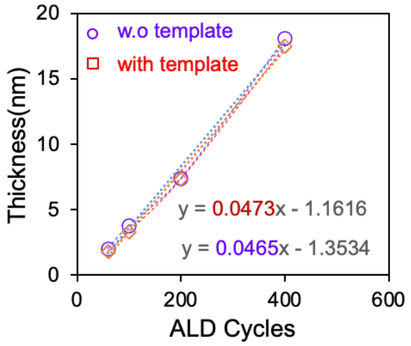

Cycles	with template TiO2 thickness	w.o template TiO2 thickness
10	0	0
60	1.8	2
100	3.3	3.8
200	7.32	7.4
400	17.5	18.1

Figure S3 (a). STEM image of various TiO_2 cycles deposited ZnO nanowires array. (upper column) TiO_2 layer deposited on ZnO nanowires, (lower column) TiO_2 layer deposited on nonanal template absorbed ZnO nanowires. The data shows the deposition rate on the nonanal absorbed ZnO nanowires is slower than it on the ZnO nanowires, we think it is caused by the coverage of template nonanal on the ZnO nanowire.

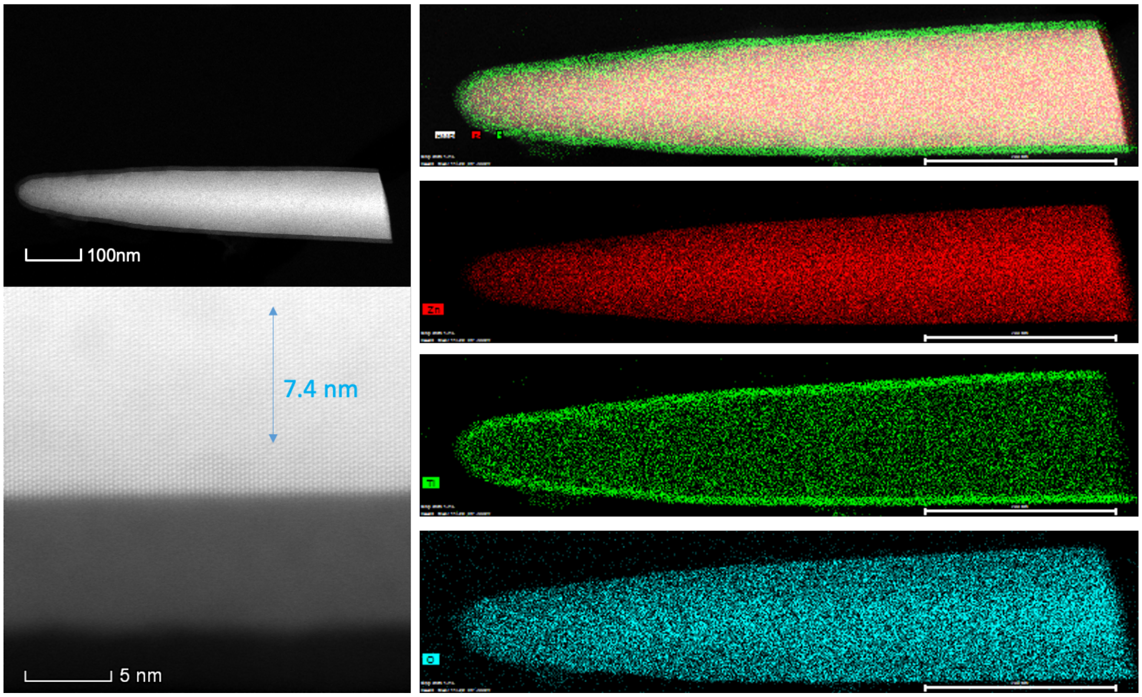

Figure S3 (b). TEM image of ZnO/TiO2 nanowires with deposition of TiO2 at 150 cycles

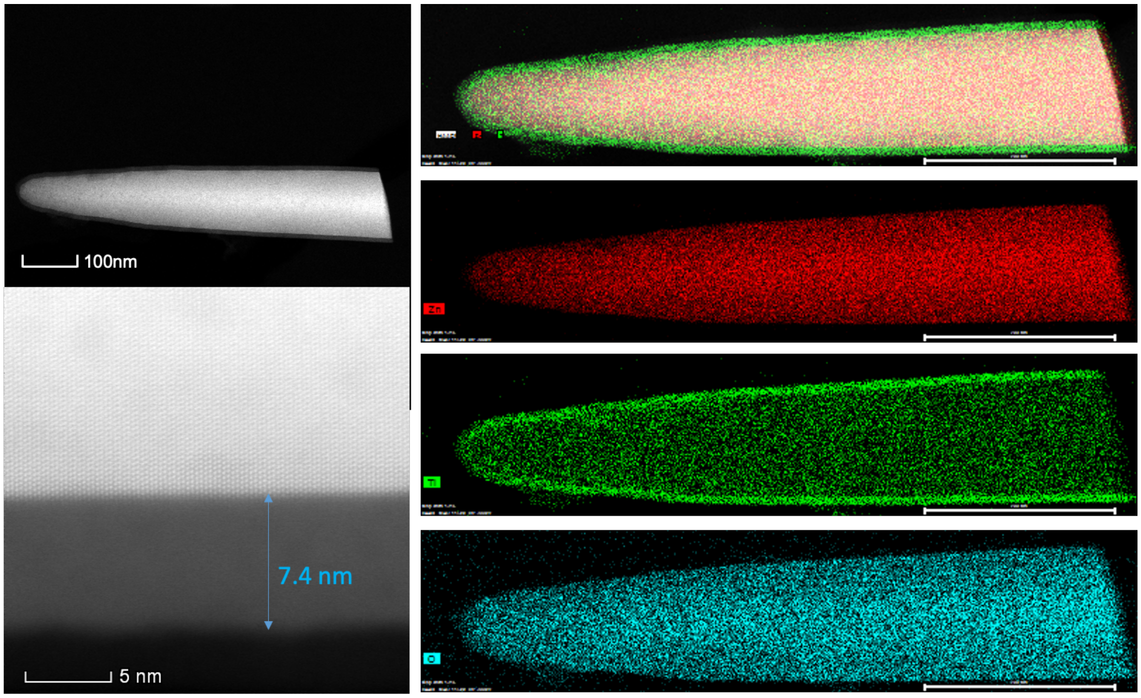

Figure S3 (c). TEM image of ZnO/TiO2 nanowires with deposition of TiO2 at 300 cycles

5.7.4 The condition of desorbed gas analysis by GC-MS

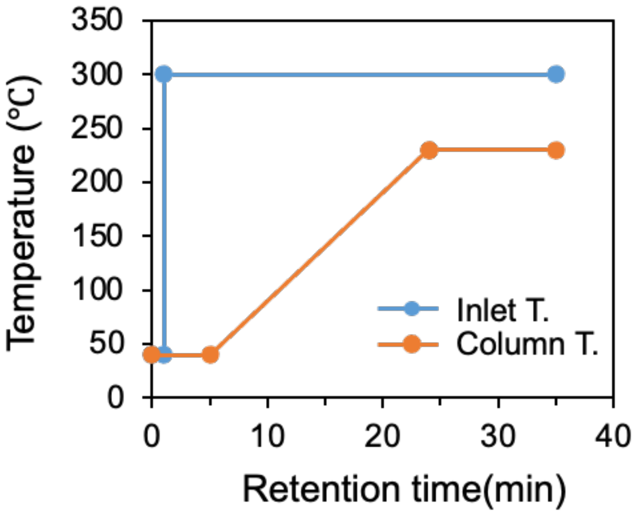

Figure S4. The temperature program for desorbed gas analysis by GC-MS

5.7.5 Gas components of saturated mixtures (C6, C9 and C11)

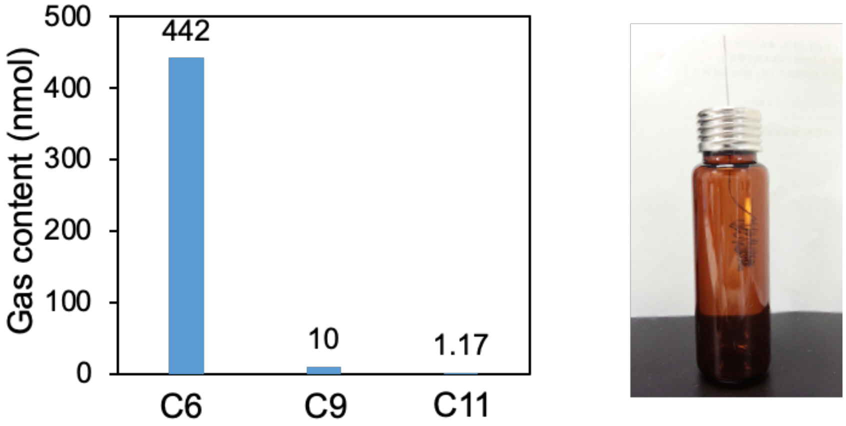

Figure S5. Components of saturated mixture in the 20ml bottle after evaporation for 30min. In the bottle, the most abundant gas is hexanal gas, the second is nonanal gas, and the least amount is undecanal gas. This can be explained by the different saturation vapor pressure.

5.7.6 Selectivity of recognition surface to molecules with different shape and function group

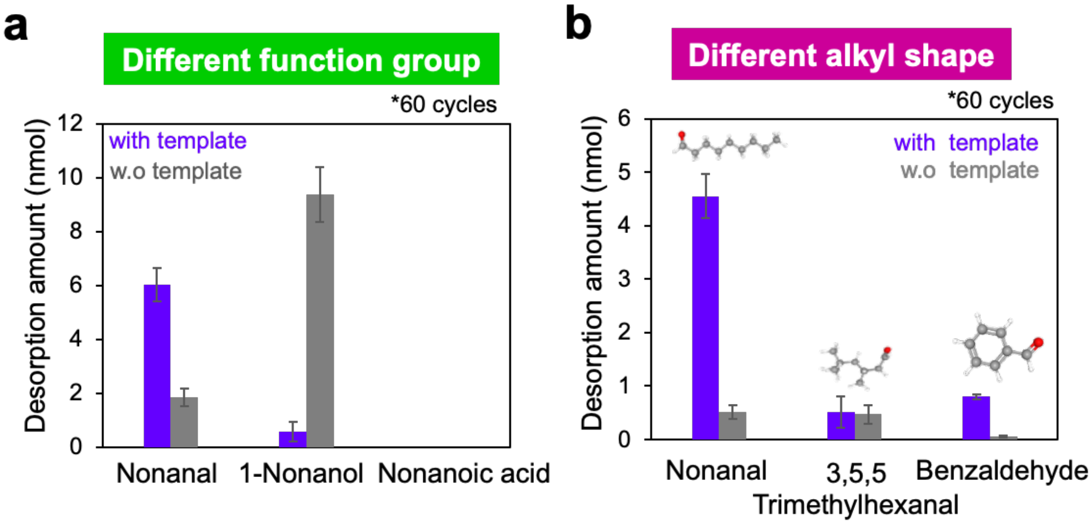

Figure S6. (a) Desorbed target molecules with different functional groups from ZnO/TiO2 nanowires with and without nonanal imprint. (b) Desorbed target molecules with different shapes from ZnO/TiO2 nanowires with and without nonanal imprint.

5.7.7 Selectivity of recognition surface with C9 imprint in mixture (C6, C8, C9, C10, C11)

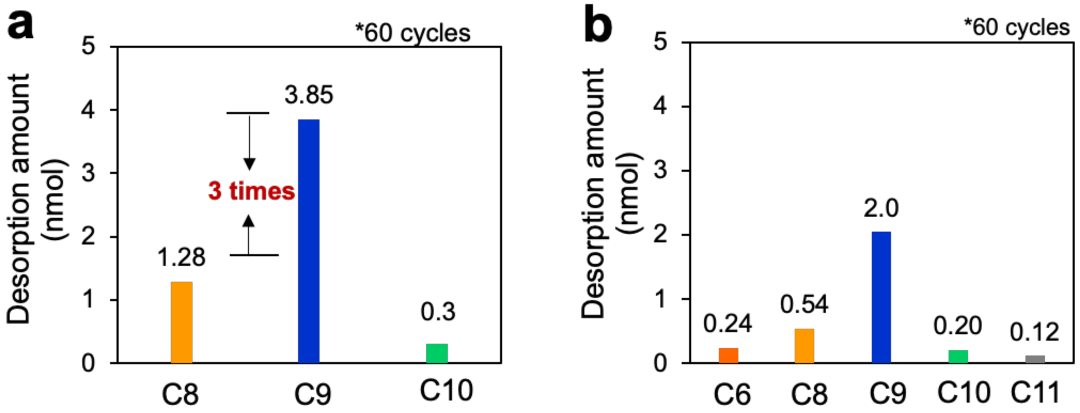

Figure S7. (a) Desorbed octanal (C8), nonanal (C9) and decanal (C10) from ZnO/TiO2 nanowires with nonanal imprint. (b) Desorbed hexanal (C6), octanal (C8), nonanal (C9), decanal (C10) and undecanal (C11) from ZnO/TiO2 nanowires with nonanal imprint. In this experiment, all of the target gases are measured in the mixture gas. (a) is measured in the mixture gas with three molecules, (b) is measured in the mixture gas with five molecules.

5.7.8 Recognition surface with undecanal (C11) imprint

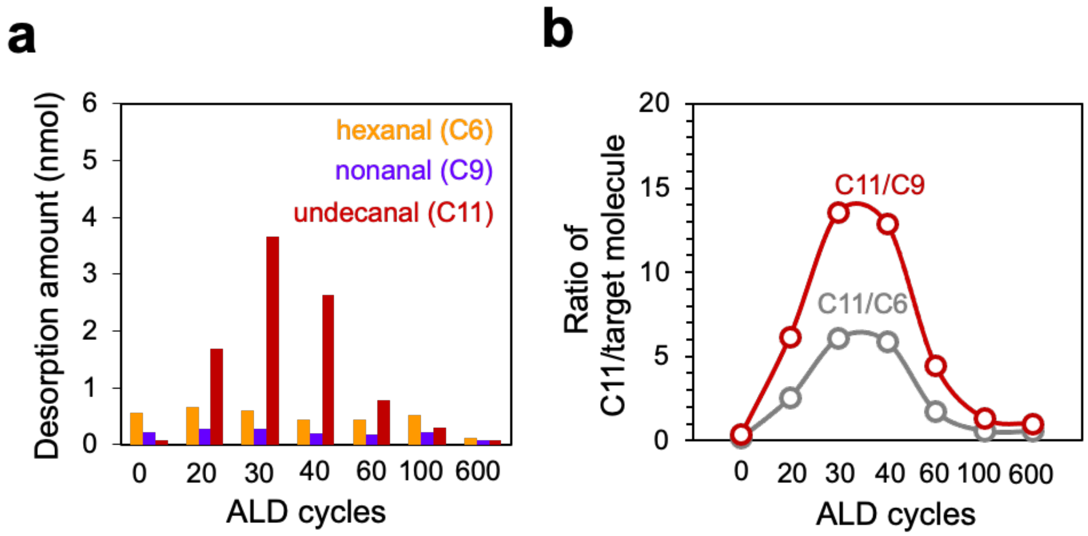

Figure S8. (a) Desorbed targets from ZnO/TiO_2 nanowires surface with undecanal (C11) imprint deposited at different TiO_2 deposition cycles. (b)The ratio of desorbed nonanal/target molecules calculated form (a).

5.7.9 Desorbed template molecule from ZnO NWs with ALD cycles at 0 cycle

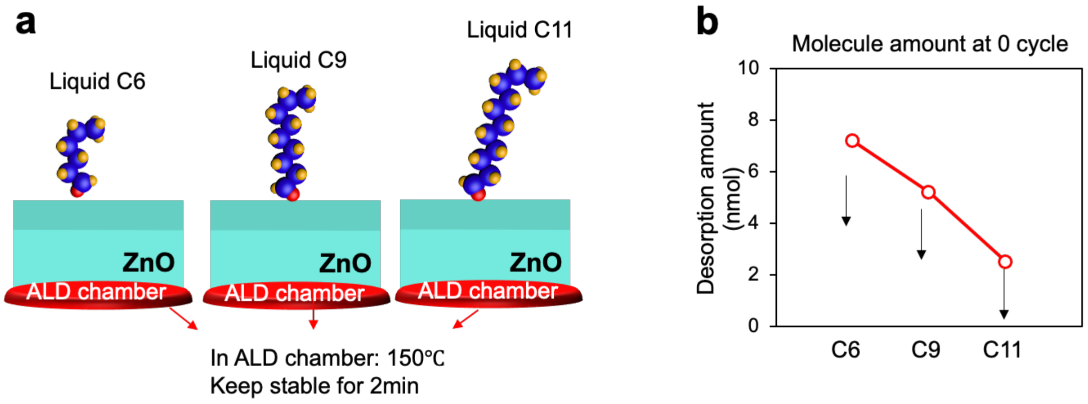

Figure 9. (a) Schematic of template molecules on ZnO nanowires in ALD chamber at 0 cycles. (b) Desorption amount of different template molecules from ZnO nanowires at 0 cycles.

5.7.10 Optimal ALD cycles for template molecules with different chain length

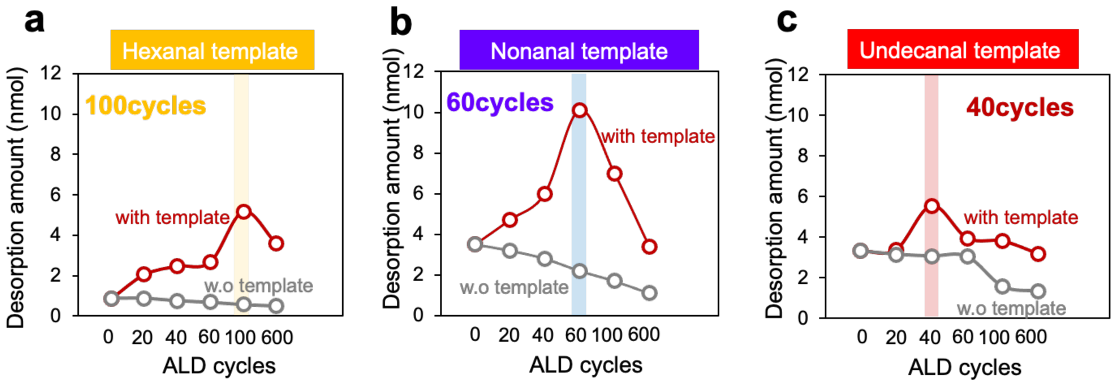

Figure 10. Optimal ALD cycles for (a) Hexanal template, (b) Nonanal template, (c) Undecanal template. Here the optimum thickness varies from template molecule to template molecule. This is related to the desorption content of different template molecules with deposited TiO_2 at 0 cycle.

5.7.11 Temperature-dependent FTIR of nonanal template adsorbed ZnO NWs

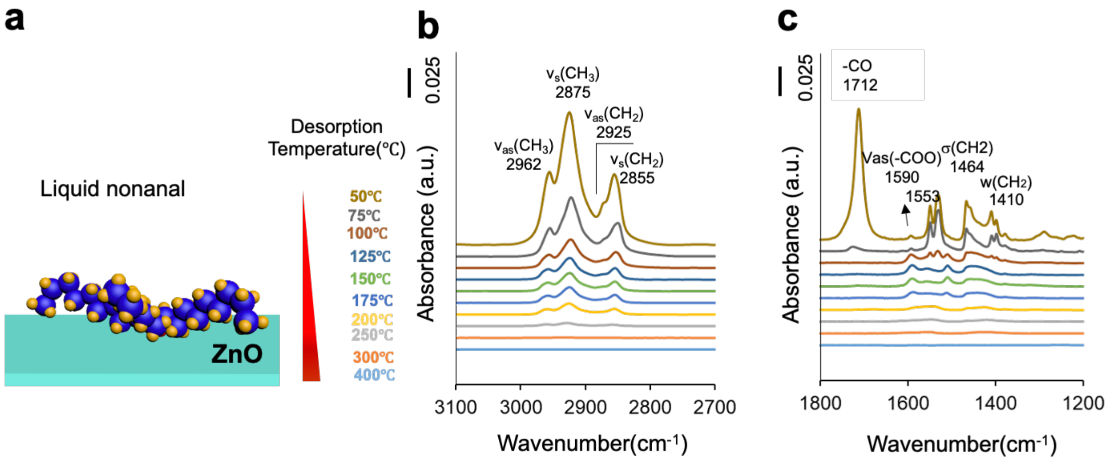

Figure S11. (a) Schematic, (b) and (c) Temperature-dependent FT-IR spectra of liquid nonanal-adsorbed ZnO nanowires. In this experiment, the ZnO nanowires were immersed into the liquid pure nonanal, then the nonanal absorbed ZnO nanowires were annealed at different temperatures for 5 mins.

5.7.12 Stability of nonanal template on ZnO nanowire with TiO_2 deposition at 0 cycle

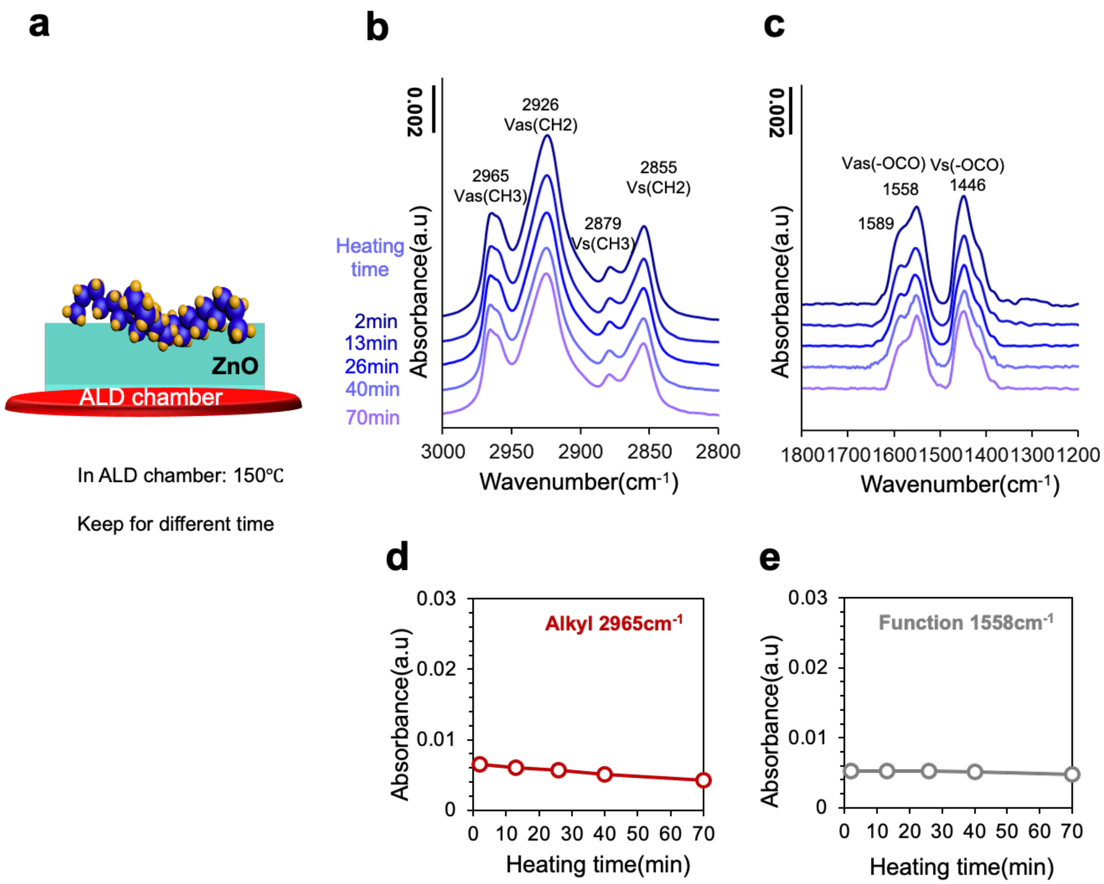

Figure S12. (a) Schematic of template nonanal adsorbed on ZnO nanowires in ALD chamber with deposited TiO_2 at 0 cycle, (b) and (c) FT-IR of nonanal adsorbed ZnO nanowire at different resting time in ALD chamber deposited TiO_2 at 0 cycle, (c) and (d) calculated intensity data of absorbance from (a) and (b).

5.7.13 pMAIRS of Nonanal template at different ALD cycles

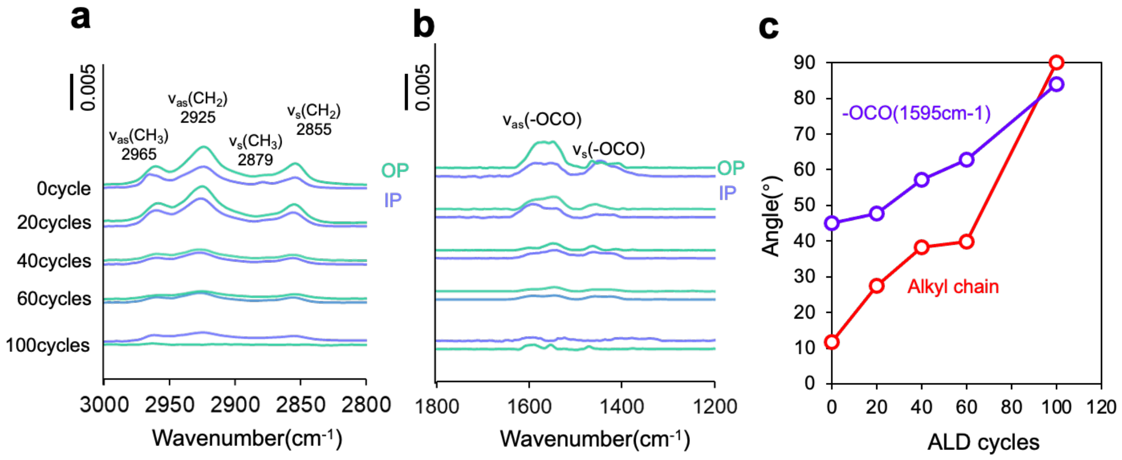

Figure S13. pMAIRS of nonanal template absorbed on ZnO nanowires deposited with TiO_2 layer at different ALD cycles.

5.7.14 Adsorption of nonanal template on ZnO NWs during ALD process

Baseline of IR spectra of nonanal on ZnO and TiO2 surface

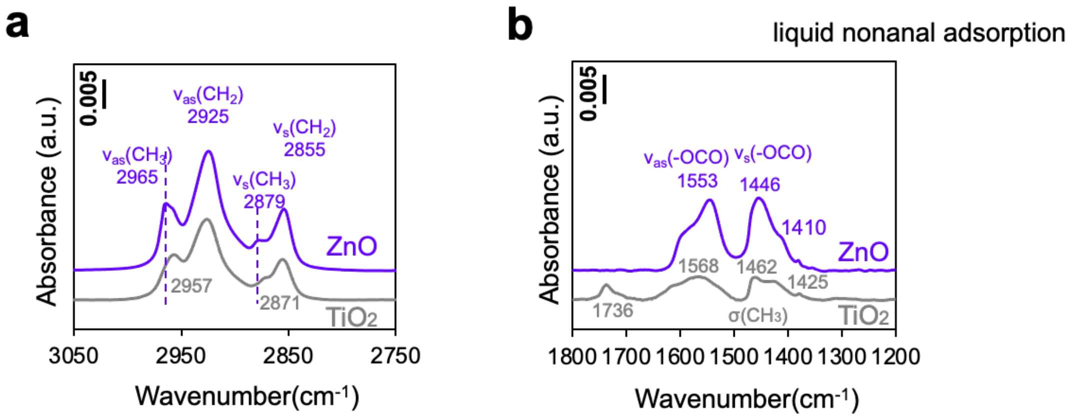

IR spectra of nonanal template on imprinting surface of nanowires

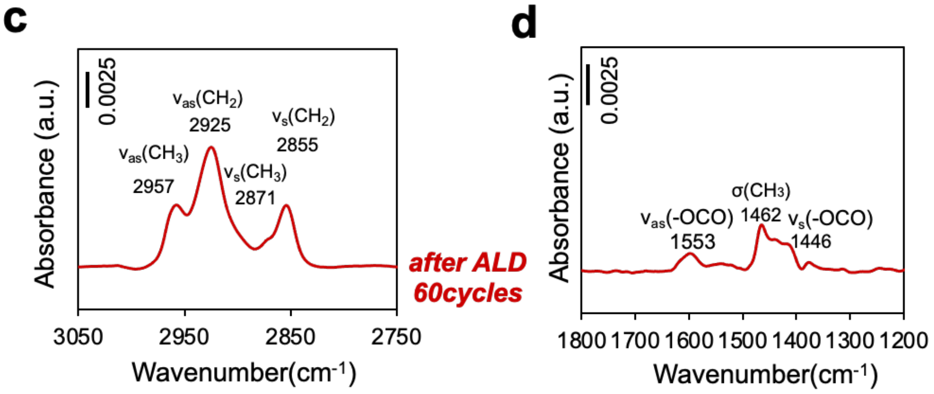

Figure S14. IR spectra of nonanal template adsorbed on different surface. (a) and (b) baseline of IR spectra of nonanal template on ZnO and TiO2 surface. (c) and (d) IR spectra of nonanal template on ZnO nanowires with the deposition of TiO2 at 60 cycles. In this experiment, the baseline of IR spectra of nonanal on ZnO and TiO2 surface are measured at a TiO2 deposition cycle of 0.

5.7.15 Nonanal template removal process

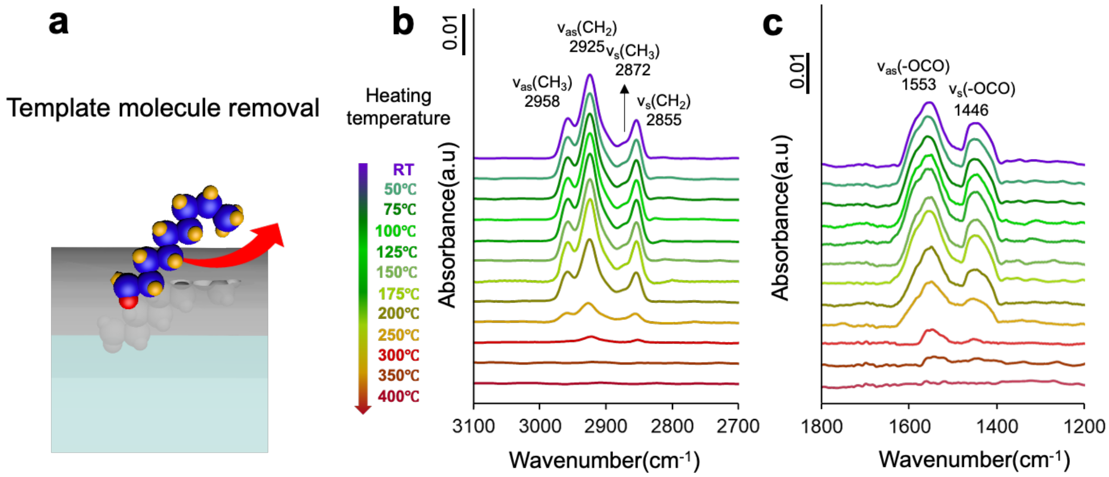

Figure S15. (a) Schematic of nonanal template removal process, (b) and (c)Temperature dependent FT-IR spectra of nonanal template from ZnO/TiO_2 nanowire with deposition TiO_2 at 60 cycles.

5.7.16 Adsorption state of target nonanal on imprinted ZnO/TiO_2 NWs

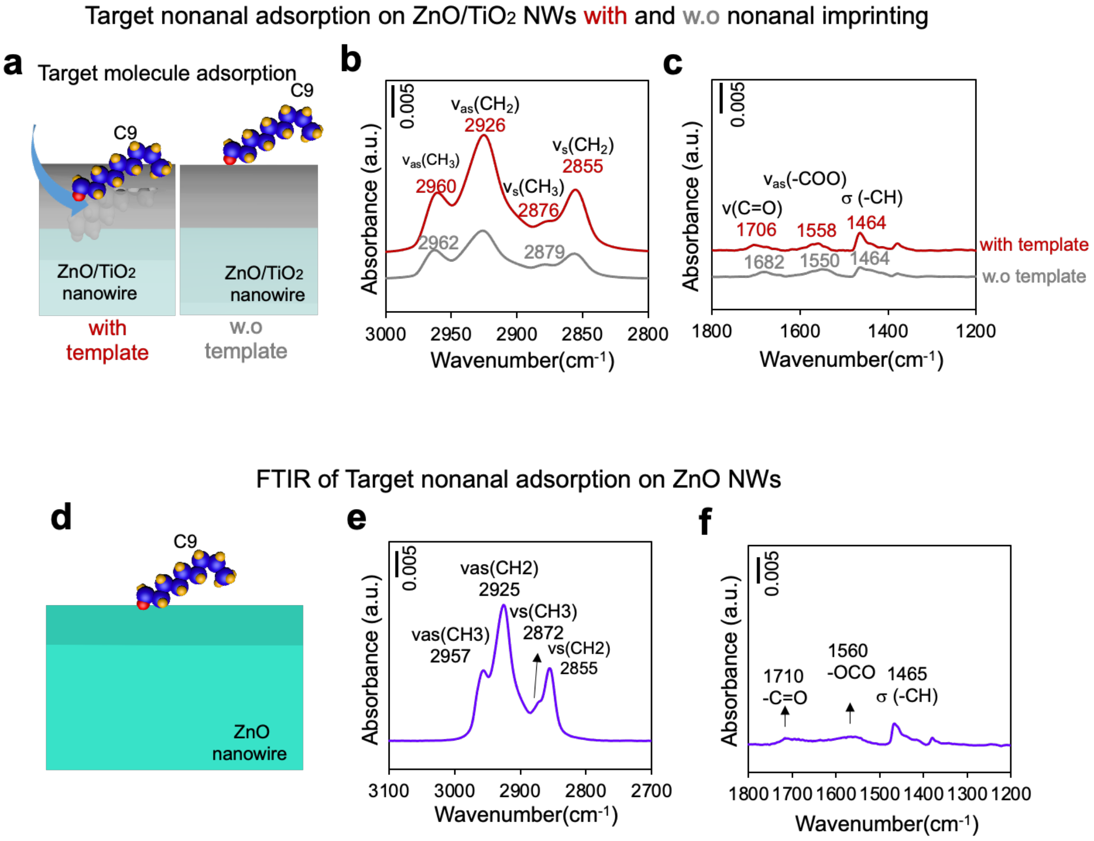

Figure S16. (a) Schematic of target nonanal gas absorbed on ZnO/TiO2 nanowires with and without nonanal imprint, (b) and (c) FT-IR of target nonanal gas absorbed on ZnO/TiO2 nanowires with and without nonanal imprint. (d) Schematic of target nonanal gas absorbed on ZnO nanowires, (e) and (f) FT-IR spectra of target nonanal gas absorbed on ZnO nanowires. In this experiment, before target nonanal adsorption, all the samples are pre-treated at 400 °C for 30 min.

5.7.17 Simulation of the molecule absorbed on ZnO NWs

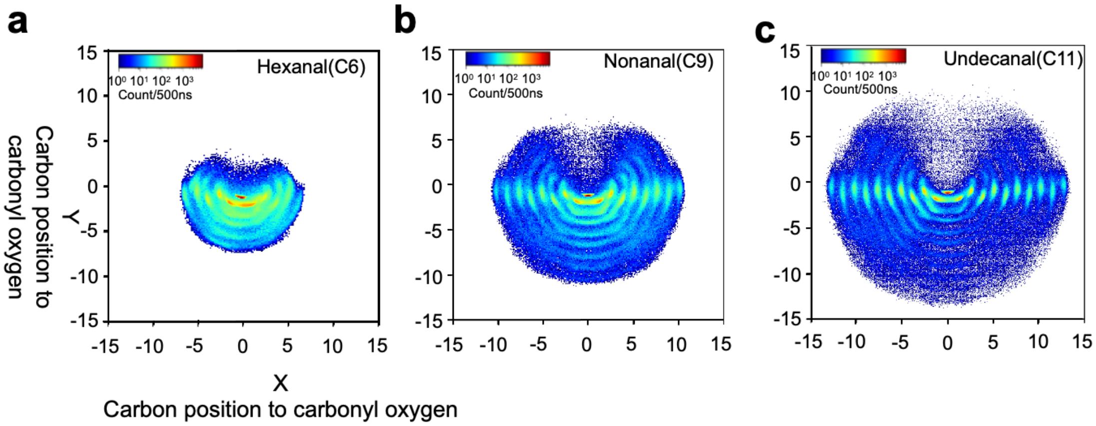

Figure S17. Dynamic adsorption state of molecules on the (100) plane of ZnO nanowire. (a) Hexanal, (b) Nonanal, (c) Undecanal. In this calculation, the method of Molecular dynamics by AMBER (500nsec) was used.

5.7.18 Calibration curve of gas phase

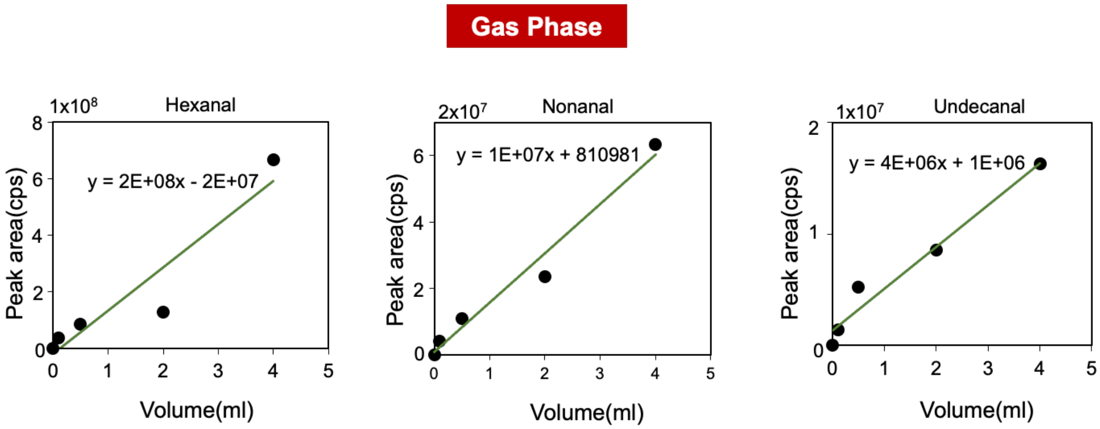

Figure S18. Volume calibration of hexanal, nonanal and undecanal by GC-MS (from left to right).

5.7.19 Calibration curve of concentration

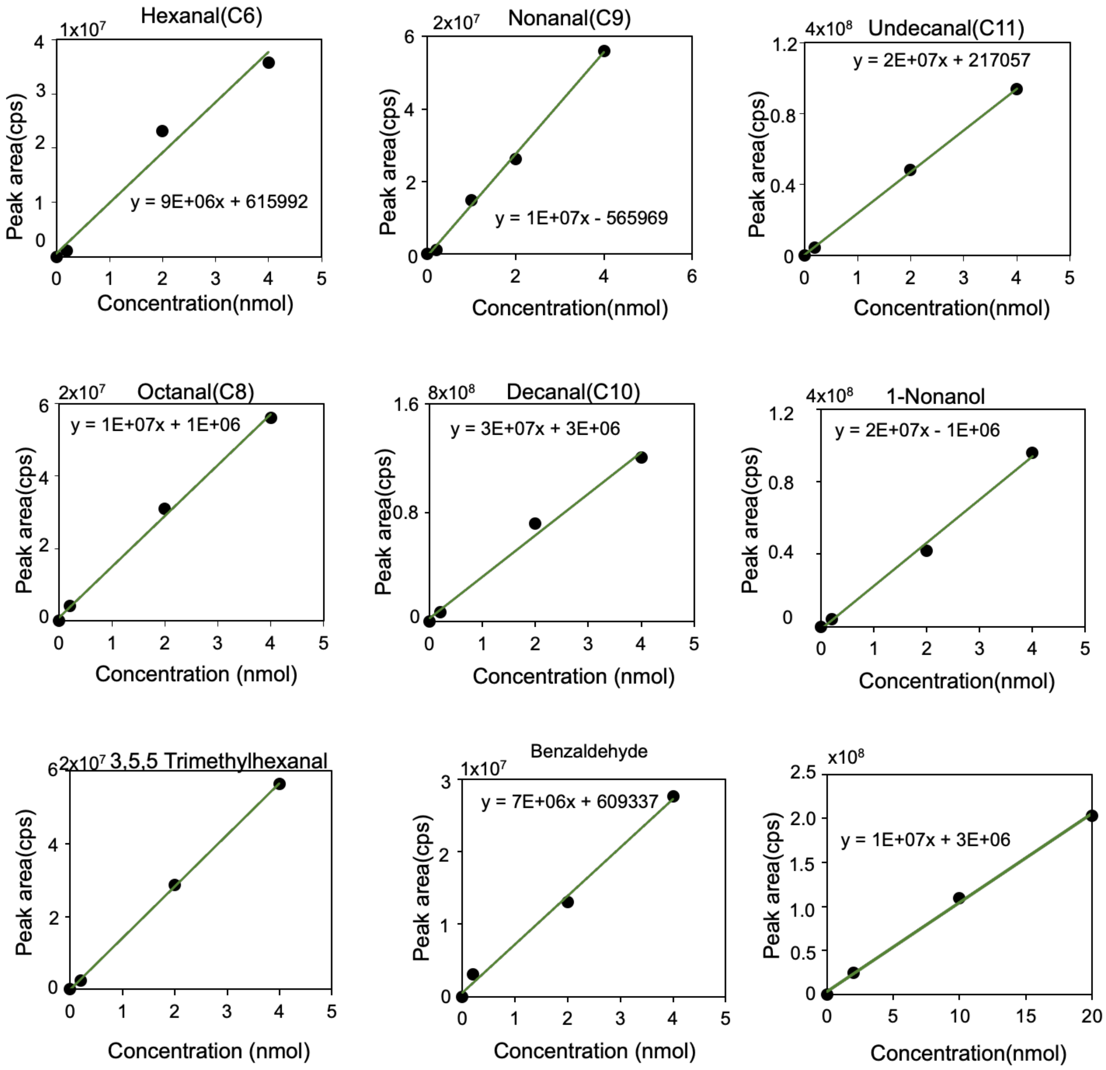

Figure S19. Target molecules concentration calibration by GC-MS.

5.7.20 FTIR spectra of liquid hexanal, nonanal and undecanal

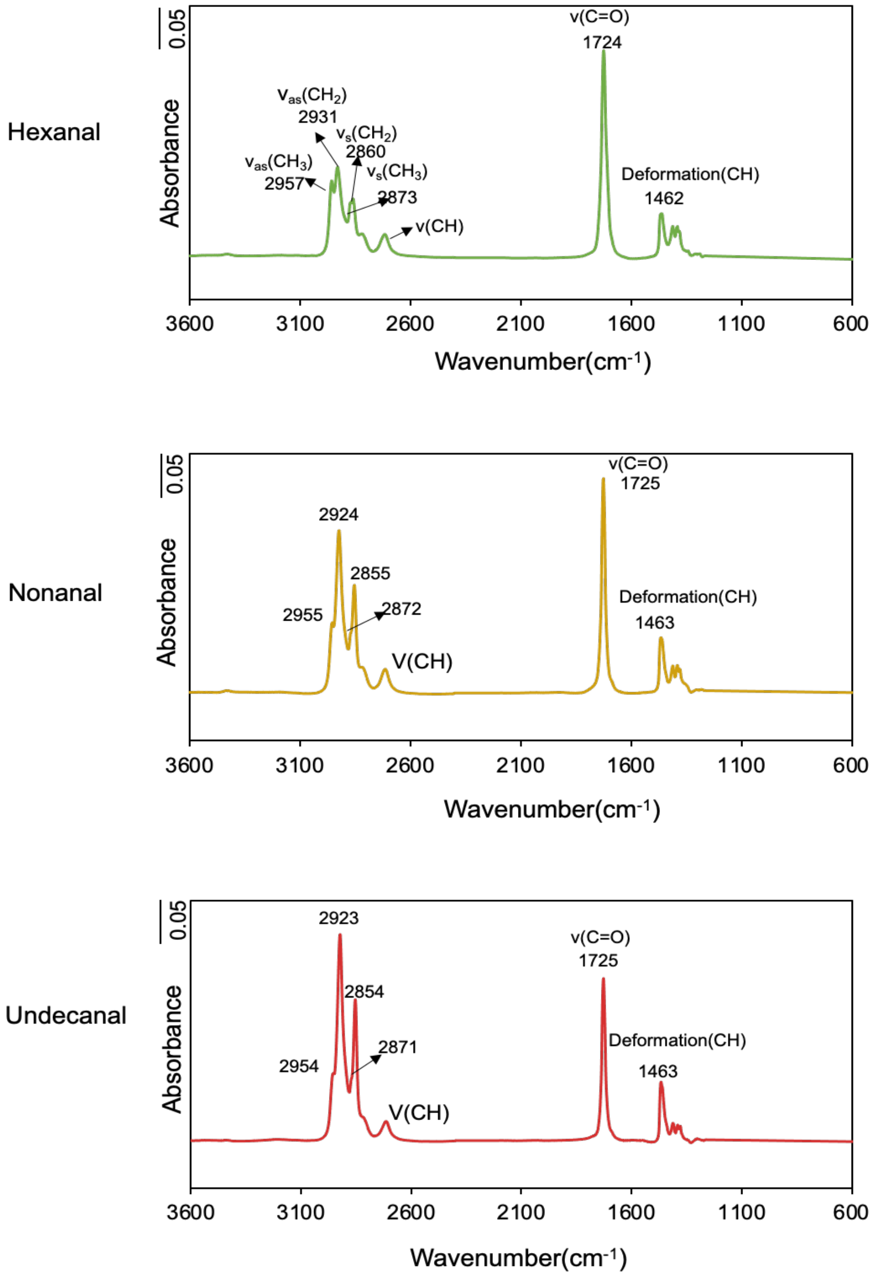

Figure S 20. FT-IR spectrum of liquid hexanal, nonanal and undecanal.

Chapter VI

Overall Conclusions

6.1 Overall Conclusions

In summary, this thesis is focused on these issues to gain insight into the mechanism and achieve breakthroughs in science and technology.

Firstly, the effect of ammonia addition to the "concentration window" required in the crystal growth of hydrothermal ZnO nanowires is well elucidated in Chapter III. It is found that the ammonia addition substantially narrows the width of "concentration window" and significantly increased the growth rate of ZnO nanowires. This concept of narrowed the "concentration window" will be useful, especially when it is necessary to increase the growth rate of hydrothermal ZnO nanowires without the need for any additional equipment.

Secondly, to obtain a more homogeneous nanowire structure, we demonstrated a facile, rational synthesis of monodispersed ZnO nanowires from randomly sized seeds by two-step hydrothermal growth. The nanowire tips with shape uniformity and spatial separation were formed in the ammonia-dominated alkaline conditions in step1. The tips serve as a seed for the growth of the monodisperse nanowires in step 2. We think the concept of two-step growth consisting of sharp tip formation and the subsequent nucleation control on the sharp tips must be general for monodisperse nanowire synthesis in diverse metal oxide nanowires and pave the road for metal oxide nanowires-integrated nanodevices.

Thirdly, we created a nonanal imprinted surface on the ZnO nanowires by atomic layer deposition (ALD) process, which can discriminate the target aldehydes with only one carbon difference. Isolation of the aggregated template molecules during the formation process plays an important role in forming molecular recognition surface and has been experimentally verified by pre-heating the nonanal absorbed ZnO nanowires. In addition, we confirmed the thermal stability of the recognition surface, which can be maintained up to 400°C for more than 720 hours.

Overall, improving the structural controllability of metal oxide nanowires and creating molecular recognition surfaces on the nanowires to discriminate between similar chain aldehydes will provide a promising platform for the development of integrated molecular recognition devices.

List of Publications

Scientific Journal in This Thesis

1. (Chapter IV)
"Substantial Narrowing on the Width of "Concentration Window" of Hydrothermal ZnO Nanowires via Ammonia Addition"
D. Sakai, K. Nagashima, H. Yoshida, A. Inoue, C. Nakamura, M. Kanai, Y. He, G. Zhang, **X. Zhao,** T. Takahashi, T. Yasui, T. Hosomi, Y. Uchida, S. Takeda, Y. Baba and T. Yanagida.
Scientific Reports, **2019**, 9, 14160.

2. (Chapter III)
"Synthesis of Monodispersedly Sized ZnO Nanowires from Randomly Sized Seeds"
X. Zhao, K. Nagashima, G. Zhang, T. Hosomi, H. Yoshida, Y. Akihiro, M. Kanai, W. Mizukami, Z. Zhu, T. Takahashi, M. Suzuki, B. Samransuksamer, G. Meng, T. Yasui, Y. Aoki, Y. Baba and T. Yanagida.
Nano Letters. **2020**, *20*, 599-605

3. (Chapter V)
"Molecularly Templated Metal Oxide Surface Discriminates Length of Aliphatic Chains with Long-Term Thermal Robustness"
X. Zhao, K. Nagashima, G. Zhang, T. Hosomi, M. Kanai, W. Mizukami, N. Saito, Z. Zhu, T. Takahashi, T. Yasui, Y. Baba and T. Yanagida.
In submission.

The Other Scientific Journals

"Face-Selective Tungstate Ions Drive Zinc Oxide Nanowire Growth Direction and Dopant Incorporation"
J. Liu, K. Nagashima, H. Yamashita, W. Mizukami, T. Hosomi, M. Kanai, **X. Zhao,** Y. Miura, G. Zhang, T. Takahashi, M. Suzuki, D. Sakai, Y. He, T. Yasui, Y. Aoki, Y. Baba, J.C. Ho and T. Yanagida
Communications Materials, **2020**, 1, 58.

Conferences

1. "High uniformity ZnO nanowires growth from random seed layer"
   X. Zhao，G. Zhang，K. Nagashima，D. Sakai，A. Inoue，C. Nakamura，M. Kanai，Y. He，T. Takahashi，T. Yanagida
   第 78 回応用物理学会秋季学術講演会，福岡国際会議場，福岡，7p-PA7-142017 年 9 月 5-8 日．（ポスター発表）

2. "Impact of precise control of zinc complex concentration on face selective. enhancement of hydrothermal ZnO nanowire growth,"
   D. Sakai, K. Nakamura, K. Nagashima, H. Yoshida, A. Inoue, C. Nakamura, M. Kanai, G. Zhang, **X. Zhao**, T. Takahashi, S. Takeda and T. Yanagida, *The 19th Cross Straits Symp. on Energy and Environmental Science and Technology (CSS-EEST19)*, Fukuoka, Japan, 2017/11/29-12/1. (Poster)

3. "Synthesis of ultra-uniform sized ZnO nanowires by post-growth homogenization of. growth interface"
   X. Zhao，K. Nagashima，G. Zhang，Z. Zhu，T. Takahashi，T. Hosomi，H. Yoshida，M. Kanai，S. Takeda，T. Yanagida
   第 37 回電子材料シンポジウム，ホテル&リゾーツ長浜，滋賀，2018 年 10 月 10-12 日．（ポスター）

4. "Synthesis of Ultra Uniform Sized ZnO Nanowires by Post-growth Homogenization. of Growth Interface"
   X. Zhao，K. Nagashima，G. Zhang，H. Yoshida，Z. Zhu，T. Takahashi，T. Hosomi，M. Kanai，G. Meng，S. Takeda，T. Yanagida
   平成 30 年度応用物理学会九州支部学術講演会（international session），福岡大学七隈キャンパス，福岡，8Gp-1，2018 年 12 月 8-9 日．（口頭発表）

5. "Synthesis of Monodispersedly Sized ZnO Nanowires from Randomly Sized Seeds"
   X. Zhao，K. Nagashima，G. Zhang，H. Yoshida，Z. Zhu，T. Takahashi，T. Hosomi，M. Kanai，G. Meng，S. Takeda，T. Yanagida
   International School and Symposium on Nanoscale Transport and Photonics 2019. (ISNTT), Wen-25, Atsugi, Japan, 2019/11/18-22. (Poster)

6. “Synthesis of Monodispersedly Sized ZnO Nanowires from Randomly Sized Seeds”
   X. Zhao，長島一樹，Zhang Guozhu，細見拓郎，吉田秀人，金井真樹，高橋綱己，柳田剛
   第68回応用物理学会春季学術講演会，オンライン，17p-Z18-9，2021年3月17日．（口頭発表）

Research Funding

1. 研究課題「原子分解能を有する分子認識ナノワイヤ界面及び新規分子識別センシングデバイスの創製」
   （独）日本学術振興会　特別研究員奨励費（DC2）, 2019.4 - 2021.3

Awards

NTT-BRL school scholarship　　2019